ATLAS NOTE

May 21, 2012

Measurement of $W\gamma$ and $Z\gamma$ Productions and Searches for Technicolor in $p-p$ collisions at $\sqrt{s}=7$ TeV with the ATLAS Detector

Supporting Note v1.0

The ATLAS collaboration

Abstract

We present measurements of high energy photons produced in associated with W and Z bosons in pp collisions at $\sqrt{s}$ = 7 TeV. The analysis starts with a data set of W and Z bosons with leptonic e/μ decays selected with the criteria used for inclusive W/Z studies. A subset of these events is identified by demanding an electromagnetic object passing tight photon cuts with an additional isolation requirement. The measurement is performed on a data sample with an integrated luminosity of ~ 5 fb^{-1} collected during the 2011 data taking. Production cross sections of $W\gamma$ and $Z\gamma$ are measured in fiducial phase space well covered by the ATLAS detector and for several ranges of the transverse energy of the photon. The measured fiducial cross sections at high photon transverse energy ranges are used to determine the limits on the anomalous Triple Gauge-Boson Couplings. In this data sample the analysis also search for Technicolor where the technimesons decay into $W\gamma$ pair or $Z\gamma$ pair, forming narrow resonances in the $W\gamma$ and $Z\gamma$ mass distributions. No evidence of technicolor is observed in the data and limits on the production cross section times branching ratios and the masses of the technimesons are determined at 95% confidence level.

Contents

1 Introduction

1.1 Measurement of Standard Model $W\gamma$ and $Z\gamma$ Productions

Measurements of W and Z bosons productions in association with high energy photons provide important tests of the Standard Model (SM) of particle physics. The $W\gamma$ process is directly sensitive to the triple gauge boson couplings predicted by the non-Abelian $SU(2)_L \times U(1)_Y$ gauge group of the electroweak sector. However, the triple gauge boson couplings in the $Z\gamma$ process is forbidden in the SM at tree level. Physics beyond the SM can enhance the production cross sections and alter the event kinematics.

In this paper we report on the measurements of $W\gamma$ and $Z\gamma$ productions using the full 2011 data sample ($L \sim 5$ fb^{-1}) collected with the ATLAS detector. The analysis strategy is to identify W and Z bosons using a data set based upon high E_T/P_T e/μ triggers, and then search for a high energy isolated photons in these events. The experimental results is compared to the Standard Model predictions that include direct $W\gamma/Z\gamma$ production and final state photon radiation off the leptons from the W/Z decays. The relevant leading order Feynman diagrams involved in the $W\gamma$ processes are shown in Figure 1. Diagrams for the $Z\gamma$ processes are similar except for the s-channel case ($ZZ\gamma$ vertex), which is forbidden in the Standard Model. The selected signal events in the data also include events with photons coming from hard fragmentation of a quark or gluon (see Figure 2 for the case of $l\nu\gamma$). This source, while reduced by the photon identification and isolation requirements, cannot be neglected and is considered as a part of the signal process in the analysis presented here.

1.1.1 Previous measurements of SM $W\gamma$ and $Z\gamma$ productions

The first measurement of $W\gamma$ and $Z\gamma$ production with the ATLAS detector was performed with a data sample of ~ 35 pb^{-1} collected in 2010 at $\sqrt{s} = 7$ TeV [1]. In that measurement the production processes $p+p \rightarrow l+\nu+\gamma+X$ and $p+p \rightarrow l^+ + l^- + \gamma + X$ (where the leptons are electrons or muons) were studied. Due to small data statistics, the fiducial and production cross sections were only measured for a single photon transverse energy range ($E_T > 15$ GeV).

The second analysis looked at the data sample collected by ATLAS in the first half of 2011, which has a size of $L \sim 1$ fb^{-1} [2]. The new measurement also considers the leptonic decays of the W and Z bosons and minimum photon transverse energy $E_T > 15$ GeV. With a larger data sample, fiducial cross sections for several photon transverse energy ranges, and fiducial cross sections for exclusive $W\gamma$ and $Z\gamma$ production in the case where no jet is reconstructed in the final state are measured. The exclusive measurements at the highest photon transverse energy range are used to extract limits on the anomalous triple gauge-boson couplings.

1.2 Searches for Technicolor

Technicolor [3, 4], another extension of the SM, is invented to provide a natural and consistent quantum-field-theortic description of electroweak symmetry breaking. The theory does not requires the existence of elementary scalar fields (e.g. the Higgs boson). The model postulates the existance of a new strong gauge interaction, which can generate the electroweak symmetry breaking, and therefore the masses of the W and Z bosons. New particles, technifermions, are introduced by the model and they can form technimeason bound states (e.g. technipion (π_T), technirho (ρ_T), techniomega (ω_T)).

In the Low Scale Technicolor (LSTC) model [5], which is developed to overcome the flavor changing neutral current (FCNC) problem in the older technicolor models, the technicolor scale is lower and this allows the lightest technimesons to be accessible at the LHC. The technimesons can decay into electroweak boson (γ, W or Z) plus π_T, or to a pair of electroweak bosons. The neutral ρ_T and ω_T can decay to $Z\gamma$ pair and charged $a_T^{\pm}$ and $\rho_T^{\pm}$ can decay into $W\gamma$ pair. Their production and decay diagrams

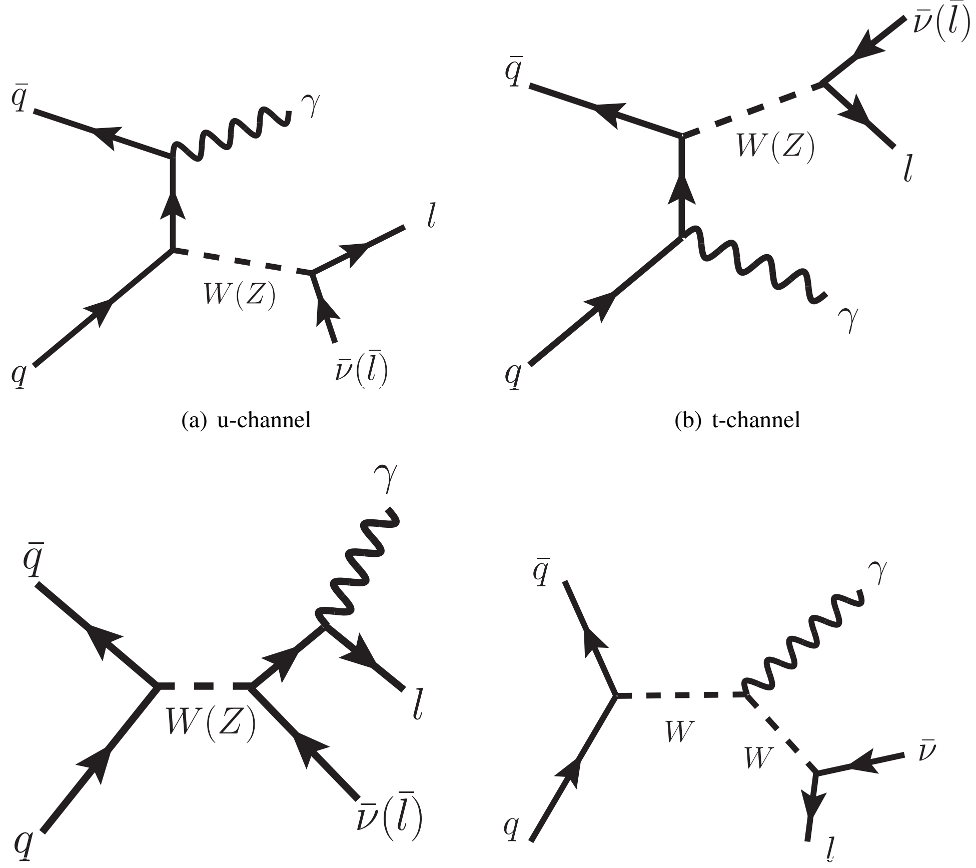

(a) u-channel (b) t-channel

(c) FSR (d) s-channel

Figure 1: Feynman diagrams of $W\gamma$ and $Z\gamma$ production in (a) u-channel (b) t-channel and (c) final state photon radiation (FSR) from the W and Z boson decay process. (d) Feynman diagram of $W\gamma$ production in the s-channel.

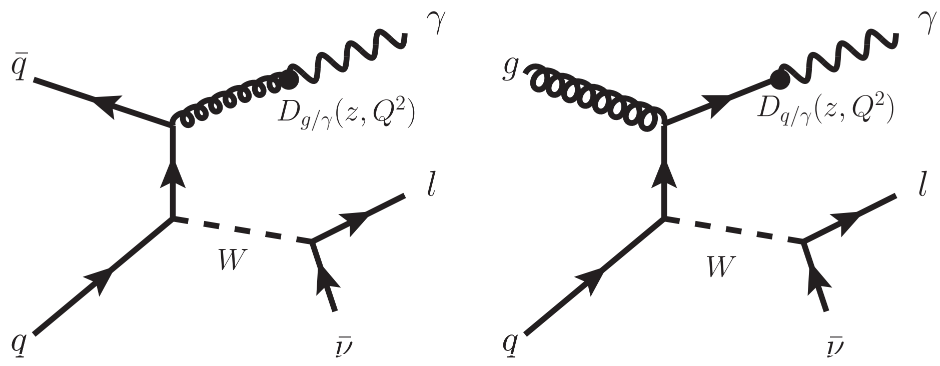

(a) (b)

Figure 2: Diagrams of the signal contributions from the $W + q(g)$ processes when a photon emerges from the fragmentation of the final state parton.

Electron		Muon	
Periods	Trigger	Periods	Trigger
D-J	EF_e20_medium	D-I	EF_mu18_MG
K	EF_e22_medium	J-M	EF_mu18_MG_medium
L-M	EF_e22vh_medium1		

Table 1: Single lepton triggers used to collect the data samples for $W\gamma$ and $Z\gamma$ measurements.

are shown in Figure 3. As the decays consist of a $W\gamma$ or $Z\gamma$ pair, the measurements of SM $W\gamma$ and $Z\gamma$ production can be converted into searches for technicolor through the production of ρ_T, ω_T, $a_T^{\pm}$, and $\rho_T^{\pm}$. In the search analysis, all of the the physics objects (e.g. electron, muon, photon, jets and missing transverse energy) reconstruction, event selections and background estimations are performed in the same way as the SM measurement.

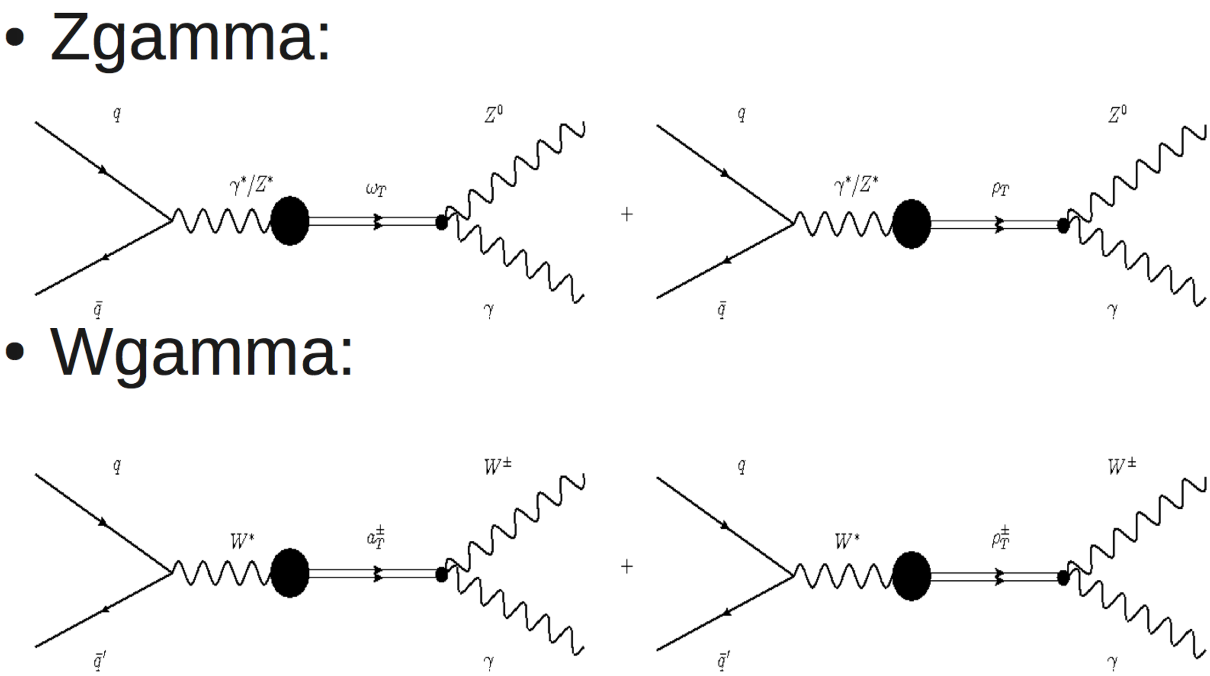

(a)

Figure 3: Feynman diagrams of productions and decays of ρ_T, ω_T, $a_T^{\pm}$, and $\rho_T^{\pm}$ technicolor particles.

1.3 Data Sample

The analysis is based on a sample of $\sqrt{s} = 7$ TeV proton-proton collision events that are collected by the ATLAS experiment in 2011 (data-taking period from D to M). We apply a Good Run List (GRL) criterion on these triggered data to select events that were collected during the time when the ATLAS sub-detectors, essential to this analysis, were operating properly. The ATLAS WZ/EWK common GRL (data11_7TeV.periodAllYear_DetStatus-v36-pro10_CoolRunQuery-00-04-08_WZjets_allchannels_DtoM.xml) is used by the analyses in both electron and muon decay channels. The single lepton trigger requirements use in the $W\gamma$ and $Z\gamma$ analysis in the electron and muon decay channels are shown in Table 1. The total integrated luminosity after the GRL requirement is 4701.37 pb^{-1} with an uncertainty of $\sim 3.9\%$ [6].

Process	Dataset	Cross Section Section (pb)	$k-$ factor	filter	Generated Events
$W\gamma$	117410.AlpgenJimmyWgammaNp0_pt20	213.06	1	1	1459774
$W\gamma$	117411.AlpgenJimmyWgammaNp1_pt20	52.199	1	1	529881
$W\gamma$	117412.AlpgenJimmyWgammaNp2_pt20	17.259	1	1	174939
$W\gamma$	117413.AlpgenJimmyWgammaNp3_pt20	5.3316	1	1	264886
$W\gamma$	117414.AlpgenJimmyWgammaNp4_pt20	1.3762	1	1	69961
$W\gamma$	117415.AlpgenJimmyWgammaNp5_pt20	0.33819	1	1	19979
$W\gamma$	117420.AlpgenJimmyWgammaNp0_pt20	1.7841	1	1	999872
$W\gamma$	117421.AlpgenJimmyWgammaNp1_pt20	4.3796	1	1	499874
$W\gamma$	117422.AlpgenJimmyWgammaNp2_pt20	2.1438	1	1	109961
$W\gamma$	117423.AlpgenJimmyWgammaNp3_pt20	0.86924	1	1	42982
$W\gamma$	117424.AlpgenJimmyWgammaNp4_pt20	0.27857	1	1	14992
$W\gamma$	117425.AlpgenJimmyWgammaNp5_pt20	0.085262	1	1	4994
$Z\gamma$	145161.Sherpa_Zeegamma_3jets	15.343	1	1	400000
$Z\gamma$	145162.Sherpa_Zmumugamma_3jets	15.343	1	1	399879
$Z\gamma$	145163.Sherpa_Zeegamma_highpt	0.52528	1	1	200000
$Z\gamma$	145164.Sherpa_Zmumugamma_highpt	0.52528	1	1	199952

Table 2: Nominal signal MC samples for $W\gamma$ and $Z\gamma$ analysis.

1.4 Signal and Background MC samples

For the $W\gamma$ production measurement, the SM signal production is modeled by ALPGEN. The samples are generated with the MLM matching scheme and interfaced to HERWIG for parton shower and fragmenation processes, and to JIMMY for underlying event simulation. These samples are generated with zero to five jets at the matrix element level. For the $Z\gamma$ production measurement, the SM signal production is modeled by SHERPA. These samples are generated with zero to three jets at the matrix element level. ALPGEN is not used to generate the $Z\gamma$ sample because the simulation of $Z\gamma$ production process is not available in ALPGEN yet. High transverse momentum SHERPA samples ($p_T^\gamma > 40$ GeV) are also generated to increase the MC statistics at high photon transverse momentum. The nominal signal MC samples are listed in Table 2 and the signal samples for systematic studies are listed in Table 3.

Various generators are used to model the background processes in the $W\gamma$ and $Z\gamma$ analysis. Table 4 lists the MC samples used for simulating background sources. The signal samples generated with anomalous triple gauge-boson couplings are listed in Table 5.

All the simulated Monte Carlo (MC) samples are of “mc11c” type, which incorporates bunch train pileup with three bunch trains that are separated by nine bunch crossings (225 ns). The bunches within a bunch train are separated from one another by 50 ns.

1.4.1 Pile-up

Multiple proton-proton interactions can occur within a single proton bunch crossing (in-time pile-up) in the ATLAS detector. The extra interactions from the pile-up can affect the measurements of the process from the main interaction. The in-time pile-up is modelled in the MC simulation. Additional re-weighting of the MC samples have to be applied such that the samples describe the pile-up effect as seen in the data. All the MC samples use in our analysis are “mc11c” type where the extra interactions are modelled with PYTHIA 6. We follow the pile-up re-weighting method as described in Ref. [7]. As the analysis is performed on data sample that is collected with different single lepton triggers over the run periods between D to M, we apply the “Recipe F” method to re-weigh the pile-up events in the MC

Process	Dataset	Cross Section Section (pb)	$k-$ factor	filter	Generated Events
$W\gamma$	126013.Sherpa_Wenugamma_1jet	75.5	1	1	399936
$W\gamma$	126014.Sherpa_Wmunugamma_1jet	75.5	1	1	399936
$W\gamma$	126018.Sherpa_Wenugamma_highpt	2.7	1	1	300000
$W\gamma$	126019.Sherpa_Wmunugamma_highpt	2.7	1	1	300000
$Z\gamma$	126015.Sherpa_Zeegamma_1jet	14.7	1	1	200000
$Z\gamma$	126016.Sherpa_Zmumugamma_1jet	14.7	1	1	174975
$Z\gamma$	126020.Sherpa_Zeegamma_highpt	0.46	1	1	150000
$Z\gamma$	126021.Sherpa_Zmumugamma_highpt	0.46	1	1	149960

Table 3: Signal MC samples for systematic studies.

Process	Dataset	Cross Section Section (pb)	$k-$ factor	filter	Generated Events
$W \to \tau\nu$	107054.PythiaWtaunu_incl	10460	1	1	1998438
$Z \to ee$	106046.PythiaZee_no_filter	990	1	1	5000000
$Z \to \mu\mu$	106047.PythiaZmumu_no_filter	990	1	1	4999129
$Z \to \tau\tau$	106052.PythiaZtautau	990	1	1	1998042
$t\bar{t}$	105861.TTbar_PowHeg_Pythia	145.8	1	0.54301	998771
WW	105921.McAtNlo_JIMMY_WpWm_enuenu	0.503	1	1	199960
WW	105922.McAtNlo_JIMMY_WpWm_enumunu	0.503	1	1	199960
WW	105923.McAtNlo_JIMMY_WpWm_enutaunu	0.503	1	1	199966
WW	105924.McAtNlo_JIMMY_WpWm_munumunu	0.503	1	1	199956
WW	105925.McAtNlo_JIMMY_WpWm_munuenu	0.503	1	1	199961
WW	105926.McAtNlo_JIMMY_WpWm_munutaunu	0.503	1	1	199960
WW	105927.McAtNlo_JIMMY_WpWm_taunutaunu	0.503	1	1	199966
WW	105928.McAtNlo_JIMMY_WpWm_taunuenu	0.503	1	1	199958
WW	105929.McAtNlo_JIMMY_WpWm_taunumunu	0.503	1	1	199957
single-top	108341.st_tchan_munu_McAtNlo_Jimmy	6.93	1	1	299879
single-top	108342.st_tchan_taunu_McAtNlo_Jimmy	6.93	1	1	299879
single-top	108344.st_schan_munu_McAtNlo_Jimmy	0.5	1	1	299877
single-top	108345.st_schan_taunu_McAtNlo_Jimmy	0.5	1	1	299864
single-top	108346.st_Wt_McAtNlo_Jimmy	15.6	1	1	899336

Table 4: Background MC samples for $W\gamma$ and $Z\gamma$ analysis.

Process	Dataset	Cross Section Section (pb)	$k-$ factor	filter	Generated Events
$W\gamma$	126023.Sherpa_Wenugamma_LAMBDA_plus02	3.9	1	1	50k
$W\gamma$	126024.Sherpa_Wmunugamma_LAMBDA_plus02	3.9	1	1	50k
$W\gamma$	126025.Sherpa_Wenugamma_LAMp02_DKAPPAp10	3.9	1	1	50k
$W\gamma$	126026.Sherpa_Wmunugamma_LAMp02_DKAPPAp10	3.9	1	1	50k
$W\gamma$	126027.Sherpa_Wenugamma_LAMp02_DKAPPAm10	3.9	1	1	50k
$W\gamma$	126028.Sherpa_Wmunugamma_LAMp02_DKAPPAm10	3.9	1	1	50k
$W\gamma$	126029.Sherpa_Wenugamma_DELTAKAPPA_plus10	3.2	1	1	50k
$W\gamma$	126030.Sherpa_Wmunugamma_DELTAKAPPA_plus10	3.2	1	1	50k
$W\gamma$	126031.Sherpa_Wenugamma_DELTAKAPPA_minus10	3.2	1	1	50k
$W\gamma$	126032.Sherpa_Wmunugamma_DELTAKAPPA_minus10	3.2	1	1	50k
$Z\gamma$	126033.Sherpa_Zeegamma_h3gamma_plus003	0.46	1	1	25k
$Z\gamma$	126034.Sherpa_Zmumugamma_h3gamma_plus003	0.46	1	1	25k
$Z\gamma$	126035.Sherpa_Zeegamma_h3Z_plus003	0.46	1	1	25k
$Z\gamma$	126036.Sherpa_Zmumugamma_h3Z_plus003	0.46	1	1	25k
$Z\gamma$	126037.Sherpa_Znunugamma_h3gamma_plus003	2.1	1	1	25k
$Z\gamma$	126038.Sherpa_Zeegamma_h4gamma_plus00005	0.46	1	1	25k
$Z\gamma$	126039.Sherpa_Zmumugamma_h4gamma_plus00005	0.46	1	1	25k
$Z\gamma$	126040.Sherpa_Zeegamma_h4Z_plus00005	0.46	1	1	25k
$Z\gamma$	126041.Sherpa_Zmumugamma_h4Z_plus00005	0.46	1	1	25k
$Z\gamma$	126042.Sherpa_Znunugamma_h4gamma_plus00005	2.1	1	1	25k

Table 5: Signal samples generated with anomalous triple gauge-boson couplings.

samples.

2 Event Selection for SM $W\gamma$ and $Z\gamma$ Measurement

In this analysis the $W\gamma$ and $Z\gamma$ productions are measured in the leptonic decays of the W and Z bosons. We only consider the electronic and muonic decays ($W \to e\nu, \mu\nu$ and $Z \to e^+e^-, \mu^+\mu^-$ are considered as signal, $W \to \tau\nu$ and $Z \to \tau^+\tau^-$ are considered as background). Therefore the $W\gamma$ production final state consists of an isolated electron or muon, large missing transverse energy due to the un-detected neutrino, and an isolated photon. For the $Z\gamma$ production final state, it contains one pair of e^+e^- or $\mu^+\mu^-$ and an isolated photon. We select events which have these final state signatures. The following sections describe the cuts that select/identify these physics objects.

2.1 Electron Selection

In the event selection of W and Z bosons in the electron channel the reconstructed electrons are required to have a cluster transverse energy greater than 25 GeV (due to the threshold applied in the trigger), where cluster energy is calibrated using insitu energy calibration obtained from $Z \to ee$ events study [25]. The electron energy resolution in the MC is corrected using "EnergyRescaler" tool [11]. The η of the electron cluster must be within the range $|\eta| <2.47$, excluding the crack region of $1.37< |\eta| <1.52$. The electron cluster in data must also pass the OTX cleaning cut by requiring "(el_OQ&1446)==0", in order to make sure the LAr cells in the cluster do not have high voltage problem or dead readout link issue. MC simulations assume the all readout links is perfect, in order to let MC simulations reproduce the data, we apply a Egamma tool to check cluster quality using OTX map (The map to record the locations of LAr cells with dead OTX) of late period (late period E, period F,period H with the same OTX problem) for 85.35% of MC simulations events. Calorimeter and tracking information have been used to determine a baseline electron identification selection optimized for identification efficiency and jet rejection. Of the three reference set of requirements, two of them are used in the analysis reported in this document, "medium" and "tight". Their definition in terms of requirements are reported in [10]. Tight electron identification is used in the $W\gamma$ analysis, whereas medium identification requirement is applied in the $Z\gamma$ analysis. An calorimeter based isolation cut (EtCone30, corrected for energy leakage and underlying events) less than 6 GeV is required for the electron candidates in the $W\gamma$ analysis to reduce γ+jets background. No isolation requirement is needed for electron selection in the $Z\gamma$ analysis. In this analysis we do not require at least one of the selected offline electron candidate to match to a triggered electron. The requirement of such matching will have very small effect on the signal acceptance since the trigger efficiency is almost 100%.

2.2 Muon Selection

The muon selection applied in the measurements of the $W(\rightarrow \mu\nu) + \gamma$ and $Z(\rightarrow \mu\mu) + \gamma$ production cross–section follows closely the Muon Combined Performance (MCP) working group guidelines for analyses under release 17 ATLAS software [**?**]. Data events selected in the $W\gamma$ and $Z\gamma$ analyses in the muonic decay channel, must pass a single muon trigger requirement and GRL. Then the STACO algorithm is used for the offline reconstruction of high transverse momentum (p_T) isolated muons in these events.

In these analyses, all muon candidates must satisfy the following requirements:

- muons should be *combined*, hence have a track in the spectrometer associated to a track in the inner detector system, and *tight*, hence of the highest reconstruction quality;
- they should have a high transverse momentum: $p_T^\mu > 25$ GeV;
- they need to be reconstructed within $\mid \eta^\mu \mid < 2.4$;
- they have to come from the primary vertex of the interaction, therefore the distance between the muon and the primary vertex in the longitudinal plane (z_0^μ) should be smaller than 1 mm;
- this should also be true on the transverse plane, where the muon impact parameter (d_0) is required to satisfy $d_0/\sigma(d_0) < 3$;
- the ID track associated to the muon should satisfy these hits requirements:
  - (! mu_staco_expectBLayerHit) || (mu_staco_nBLHits > 0)
  - (mu_staco_nPixHits + mu_staco_nPixelDeadSensors) > 1
  - (mu_staco_nSCTHits + mu_staco_nSCTDeadSensors) >= 6
  - (mu_staco_nPixHoles + mu_staco_nSCTHoles) < 2
  - if $\mid \eta \mid < 1.9$ then $N_{TRT}^{hits} >= 6$ and $(N_{TRT}^{outliers}/N_{TRT}) < 0.9$
    - where $N_{TRT} = N_{TRT}^{hits} + N_{TRT}^{outliers}$
  - if $\mid \eta \mid >= 1.9$ and $N_{TRT}^{hits} >= 6$, then $(N_{TRT}^{outliers}/N_{TRT}) < 0.9$
- all muons should be isolated, hence have $\sum p_T^{\text{tracks}(\Delta R<0.2)}/p_T^\mu < 0.15$. Here the ratio between the sum of the transverse momenta of all tracks (except the muon one) in a cone $\Delta R < 0.2$, where $\Delta R = \sqrt{\Delta\eta^2 + \Delta\phi^2}$ around the muon direction and the transverse momentum of the muon is computed.

In the $W(\rightarrow \mu\nu)+\gamma$ analysis exactly one muon candidate must pass the quality selection, whereas exactly two muon candidates need to be reconstructed for the $Z(\rightarrow \mu\mu)+\gamma$ analysis. A match in η and ϕ coordinates is then performed between the offline reconstructed muon candidates and the trigger features reconstructed online.

When using MC simulated samples, the transverse momenta of the reconstructed muons need to be smeared in order to have a transverse momentum resolution that matches the one measured on data. The smearing is provided by the MCP group "MuonMomentumCorrections" tool [].

2.3 Photon Selection

Photon reconstruction and identification is seeded by clusters in the electromagnetic calorimeter with transverse energies exceeding 2.5 GeV, measured in projective towers of 3×5 cells in the second layer of the calorimeter. Clusters without matching tracks are directly classified as unconverted photon candidates. Clusters matched to tracks originating from reconstructed conversion vertices in the inner detector or to tracks consistent with coming from a conversion are considered as converted photon candidates. The final energy measurement is made using cluster with 3×5 cells(3×7 cells) for non-converted photons(converted photons) in barrel. In endcap, a cluster size of 5×5 is used for all candidates.

In the data the photon transverse energy is corrected with an energy scale that is obtained from resonances such as $Z \rightarrow e^+e^-$, $J/\psi \rightarrow e^+e^-$ or E/P studies using isolated electrons from $W \rightarrow e\nu$. This correction is performed by calling the "applyEnergyCorrection" method in the "EnergyRescaler" tool. For the MC events, the photon transverse energy is smeared by calling the "getSmearingCorrection" also in the "EnergyRescaler" tool. Details about the usuage of "EnergyRescaler" tool can be found at [11].

Details on algorithms implementing the photon reconstruction is given in [13]. As reference we mention below the name and meaning of the discriminating variables used in the photon selection that will be mention throughout this document:

- R_{had}: ratio of ET in the first layer of the hadronic calorimeter to the ET of the EM cluster. In the pseudorapidity range $0.8 < |\eta| < 1.37$ which is not covered by the first hadronic layer, it is the ratio of the total hadronic E_T to the EM E_T.
- **EM Middle Layer Variables**:
  - R_η: ratio in η of cell energies in 3×7 versus 7×7 cells.
  - w_2: lateral width of the shower,
  - R_ϕ: ratio in ϕ of cell energies in 3×7 versus 7×7 cells.
- **EM First (Strip) Layer Variables**:
  - w_{s3}: shower width for three strips around maximum strip,
  - w_{stot}: total lateral shower width,
  - F_{side}: fraction of energy outside a core of 3 central strips, but within 7 strips,
  - ΔE: difference between the energy of the strip with the second largest energy deposited and the energy of the strip with the smallest energy deposit between the two leading strips,
  - $Eratio$: ratio of the energy difference associated with the largest and second largest energy deposits over the sum of these energies.

For the $W\gamma$ and $Z\gamma$ analysis a tight photon candidate is selected based on these discriminating variables. The photon candidate should also pass an OTX cleaning cut requirement ("(ph_OQ & 34214) == 0"). The selected photon candidate should be isolated, has a transverse energy $E_T > 15$ GeV, and

$|\ \eta\ | < 1.37$ or $1.52 < |\ \eta\ | < 2.37$. To pass the isolation criteria, the recorded transverse energy in the isolation region (a cone size of $dR = 0.3$ surrounding the photon and excluding the photon core of $\Delta\eta \times \Delta\phi = 0.125 \times 0.175$) has to be less than 6 GeV. The transverse energy in the isolation region is corrected for the energy leakage from the photon and for the energy from the underlying events. The isolation region of cone size $dR = 0.3$ is choosen (compare to cone size of 0.2 or 0.4) to provide a balance between minimizing the effect from pile-up and to provide sufficient measurement of the energy surrounding the photon candidate if it is a fake coming from a jet.

2.4 Jet definition and selection

Jets are reconstructed from topological calorimeter clusters using the anti-kT algorithm with a resolution parameter of R = 0.4. In order to take into account the differences in calorimeter response to electrons and hadrons, a p_T and η dependent factor, derived from simulated events, was applied to each jet to provide an average energy scale correction from the electromagnetic (EM) scale to the hadronic energy scale (correct back to particle-level).

In this analysis, the selected jets are required to have $p_T > 30GeV$ at the hadronic energy scale and $|\eta| < 4.5$. Bad Jets arising from detector noise or cosmic rays were rejected following Jet/MET group recommendations on jet quality. Selected jets are required to be isolated from selected electrons and photons by requiring $\Delta R(e, jet) > 0.3$ and $\Delta R(\gamma, jet) > 0.3$, in order to avoid double counting.

As mentioned earlier there was a hole in the LAr calorimeter(runs between 180614 and 185352 or period E to H). Energies that are deposited in the LAr hole will be underestimated and it will affect the missing transverse energy measurement. In the data and mc samples we remove any event if a jet is identified within the LAr hole during the data taking period that the hole existed.

2.5 Missing Transverse Energy

In this analysis the missing transverse energy (MET) is calculated from calorimeter cells with $|eta| < 4.9$ and from muons. Cells are calibrated according to the object to which they are associated(medium electrons,tight photons,tight taus,Anti-kT R-0.4 jets with $pt > 10GeV$, and cell-out term for cells which are not associated to any object,combined muons and segment-tagged muons.)

Due to the high pileup effects, the resolution of MET is negatively affected and is increasing with in-time pileup. So that a higher MET cut $MET > 35GeV$ is applied in order to keep backgrouds which do not have real neutrino low, such as Z events.

In the earlier sections we mentioned that corrections (e.g. momentum smearing) are being applied to the leptons and photons in the MC to match closer to the data. These corrections are also propagated into the MET calculation in the MC.

2.6 $W\gamma$ and $Z\gamma$ Signal Event Selection

In this section we describe the full event selection cuts to select the $W\gamma$ and $Z\gamma$ signal events. We first select events with a W or Z boson candidate, and then we ask that there is an isolated photon in the event. In this analysis we also study exclusive $W\gamma$ and $Z\gamma$ productions where there is no reconstructed jet in the selected events.

To select events with a W or Z boson candidate, we first require the events to pass the GRL criterion and are accepted by a specific trigger path (see section 1.3). These events are then required to have at least one reconstructed vertex with three or more associated tracks with $p_T > 0.4$ GeV in the inner detector. If more than one vertex is reconstructed, the primary vertex is chosen as the one with the highest sum of the squares of the transverse momenta of all its associated tracks.

To reduce spurious missing energy prompted by detector effects, a special procedure (described in [14]) is applied to calibrated (EM+JES) jets with a transverse momentum $p_T > 20$ GeV. Events not passing this cleaning procedures are rejected (i.e. if at least one jet with $\Delta R(jet, lepton) > 0.3$ and $p_T > 20$ GeV is flagged as a "looser bad" jet). This jet cleaning is applied only to the W selection candidates to clean up events with bad Jet/MET quality.

In the data taking period between E and H a crate controller of the LAr calorimter failed, which resulted in a lost of six FEBs. This created a "hole" in the LAr calorimeter in the region $-0.1 < \eta < 1.5$ and $-0.9 < \phi < -0.5$. This "hole" could affect the measurement of missing transverse energy and the identification of electron and photon candidates. Thus events are rejected if a jet is found in the hole, and electron and photon candidates are not considered if they are also found in the hole. These requirements are only applied to the data events that are in these affected periods, and to the fraction of MC events that is equivalent to the fraction of affected data sample.

For the Z selection it is important to notice that in contrast to the inclusive Z analysis we *don't* require the invariant mass of the two lepton be compatible with the Z boson mass hypothesis. [1]. This is because our signal sample includes events where one of the lepton radiate an energetic photon that is not part of a simple two-body invariant mass calculation.

At this stage specific sets of cuts are then applied to select W and Z candidate events in the electron and muon decay channels:

- Select W candidates (electron channel)
  - one tight electron with $p_T(e) > 25$ GeV
  - $Z \to ee$ veto cut :
    - events with a second electron passing the "medium++" selection and the other electron selection (OTX, etc...) are rejected
  - $MET > 35$ GeV
  - transverse mass of electron and missing energy $M_T > 40$ GeV
- Select Z candidates (electron channel)
  - two electrons with $p_T(e) > 25$ GeV passing at least the "medium++" selection and the other electron selection (OTX, etc...)
  - the selected electrons must have opposite charge
  - the invariant mass of the two electrons M_{ee} must be greater than 40 GeV
- Select W candidates (muon channel)
  - at least one isolated muon candidate with $p_T(\mu) > 25$ GeV
  - $Z \to \mu\mu$ veto cut :
    - events with a second combined muon with $p_T(\mu) > 20$ GeV are rejected
  - $MET > 35$ GeV
  - transverse mass of muon and neutrino $M_T(\mu, \nu) > 40$ GeV
- Select Z candidates (muon channel)
  - exactly two isolated muon candidate with $p_T(\mu) > 25$ GeV
  - both muon candidates have opposite charge

[1] In the inclusive Z analysis this is done requiring $66 < M_{ll} < 116$ GeV

– invariant mass of both muon candidates $M(\mu,\mu) > 40$ GeV

Once the event has passed the W or Z boson selection cuts, we then search for a photon candidate in the event. The selection cuts for the photon candidate are:

- $p_T(\gamma) > 15$ GeV
- not located in the regions of the LAr calorimeter that suffer from readout problem due to bad OTX or in the LAr hole.
- $\mid \eta(\gamma) \mid < 2.37$ (excluding the crack region $1.37 < \mid \eta(\gamma) \mid < 1.52$)
- $dR(e/\mu,\gamma) > 0.7$
- pass tight photon ID cut
- isolated : $EtCone30\_corrected(\gamma) < 6$ GeV (corrected for photon energy leakage and energy from underlying events)
- For the $W(e\nu)\gamma$ analysis we require $\mid M(e,\gamma) - M(Z) \mid > 15$ GeV to remove events where an electron from Z decay is mis-identified as a photon. A similar Z mass window cut is not applied in the $W(\mu\nu)\gamma$ analysis because it is much harder for a muon from the Z boson decay to fake as a photon.

The requirements on the reconstructed jet are documented in Section 2.4, a few key points of jet selections is shown below as reminder.

- $p_T^{jet} > 30$ GeV, $\mid \eta^{jet} \mid < 4.4$
- $\Delta R(lepton, jet) > 0.3$ and $\Delta R(photon, jet) > 0.3$

The total number of events in the data that passed all the selection cuts for the $W\gamma$ and $Z\gamma$ analysis are listed in Table **??**.

2.7 Electron Efficiency

2.7.1 Trigger Efficiency

For the electron channel only one trigger (EF_e20_medium) was used to collect the data used in this document. As a trigger efficiency here we refer as the efficiency for single, isolated electron with $P_T >$ 25 GeV. The scale factor for EF_e20_medium trigger efficiency, used for 2011 data period D-H, has been measured with data (see [15]). The central value of electron trigger efficiency is evaluated from signal Monte Carlo sample with scale factor correction to correct for data/MC discrepancy. The detailed number of corrected electron trigger efficiency is shown in Table 24 and Table 24. The uncertainty of Trigger Efficiency includes the uncertainty in modeling of turn on curve in Monte Carlo and background uncertainty in trigger data driven measurement. The uncertainty of the electron trigger efficiency as a function of η and p_T of the electrons is given in Ref [15]. By integrating these uncertainties over the $W\gamma$ samples, the trigger uncertainty is about 0.5% for $W\gamma$ channel. The trigger efficiency for $Z\gamma$ events is close to 100% due to the fact that there are two electrons in final state, the systematic uncertainty on trigger efficiency is 0.02% as shown in Table 26.

2.7.2 Electron Identification Efficiency

For electron identification efficiency ε_e^{ID}, we take the ratio between the number of electrons passing the identification quality cuts ("tight" or "medium") and the number of electrons in signal events reconstructed within the kinematic and geometric requirements [2] The central value of the efficiency for the "tight" selection in $W\gamma$ and $Z\gamma$ events is obtained from signal Monte Carlo simulation and corrected for data/MC discrepancy using scale factor. The corrected tight electron efficiency is shown in Table 24 and corrected medium electron efficiency is shown in Table 25.

In order to correct for discrepancy between data and Monte Carlo in ε_e^{ID}, "tag and probe" measurements using probe electrons from $W \rightarrow e\nu$ and $Z \rightarrow ee$ events have been performed by Egamma group to get an efficiency scale factor(SF). Scale factors from Egamma group are given as a function of electron E_T and η. The scale factors are obtained using $1fb^{-1}$ data and recommended by EGamma (so called EGamma recommendations for EPS analyses in Ref [15]).

The main systematic uncertainty comes from the background estimation used in the tag and probe measurement, and discrepancy between Z tag and probe and W tag and probe [15] measurement. The scale factor uncertainties are provided by Egamma group as a function of p_T and η, in egammaSFclass of egammaAnalysisUtils-00-02-42 ([15]). By integrating over electron p_T and η of $W\gamma$ and $Z\gamma$ signal sample, the final systematic uncertainties due to electron efficiency is shown in Table 26.

2.7.3 Electron Isolation Efficiency

The electron isolation efficiency is estimated from Monte Carlo with scale factor correction applied to correct for data/MC discrepancy. In order to study electron isolation efficiency from data, a high purity sample of electrons is selected with $Z \rightarrow ee$ tag and probe like selection criteria:

- at least two electrons $p_T > 25GeV$ with opposite charge.
- require $80GeV < M_{ee} < 100GeV$.
- require both legs to pass robust tight electron identification cuts.
- required $30GeV < p_T < 40GeV$ for tag electron

The distribution of the isolation energy for such selected electrons is shown in Figure **??**.

The systematic uncertainty includes effects from background contamination in the electron sample, and differences in the p_T spectrum between the electron sample in $Z \rightarrow ee$ and the $W/Z + \gamma$ photon sample and the impact from in-time pileup and out-of-time pileup .

- The systematic uncertainty due to background contamination is estimated by varying the window of Z mass constraint (from 10 GeV to 30 GeV) and varying the tag electron identification cut requirements (from robust medium to robuster tight). The maximum variation (0.5%) is quoted as systematic uncertainty.
- The impact from in-time pileup is evaluated by comparing the data driven isolation efficiency in $Z \rightarrow ee$ events with different number of recontructed primary vertex as shown in Figure **??**. The systematic uncertainty from this term is less than $< 0.3\%$.
- The impact from out-of-time pileup is evaluated by comparing the data driven isolation efficiency from in $Z \rightarrow ee$ events with different bunch train as shown in Figure **??**. electrons in early bunch have larger isolation value than in late bunch crossing. The systematic uncertainty from this term is less than $< 0.5\%$.

[2] This efficiency is sometime referred as "with respect to container"

- The systematic uncertainty due to shape differences between electrons and photons is evaluated by varying the 6GeV threshold cut by the 500 MeV shift by the systematic uncertainty from this source is $< 0.2\%$.

- The systematic uncertainty due to p_T range differences between the probe electron sample in $Z \rightarrow ee$ and electrons in $W\gamma$ and $Z\gamma$. It is found that the systematic uncertainty from this term is less than $< 0.1\%$. A weak p_T dependence is shown in figure **??**.

By adding up all the systematic in quadrature, we quoted 1% as uncertainty for electron isolation cuts as shown in Table 26. The electron isolation efficiency from data driven method is found to be consistent with isolation efficiency with MC simulation with the same selection cuts, We quote scale factor (SF) equal to 1 (no scale factor is applied).

2.8 Muon Efficiency

2.8.1 Trigger Efficiency

The events selected for the $W+\gamma$ and $Z+\gamma$ analyses in the muon decay channel must have passed a single muon trigger online selection. For events relative to an early data taking period (D to I), the trigger chain required is the "EF_mu18_MG", whereas during the more recent, higher luminosity, data taking period it is required that the events pass the "EF_mu18_MG_medium" chain, due to the evolution of prescales in single muon triggers. The efficiency of the combination of these two triggers is measured using the "Tag-and-Probe" method on Z candidate sample in the data and in the monte carlo. The results of the muon trigger efficiencies measured in the data and monte carlo are documented in [16] .

The measured efficiencies of the muon triggers as a function of the muon transverse momentum, for muons in the barrel and endcap regions, are shown in Figure **??**. The trigger efficiency in the barrel (endcap) region is about $\sim 75-80\%$ ($\sim 90\%$). The ratio of the muon trigger efficiency measured in the data to the efficiency measured in the monte carlo is then used as a scale factor to correct the monte carlo. The scale factors as a function of the muon $\eta-\phi$ location in the barrel region, and as a function of the muon transverse momentum in the endcap region, are shown in figure **??**.

The systematic uncertainties on the scale factor measurements are estimated by comparing the results from two independent measurements (one is D3PD based and the other is AOD based) with slightly different selections, and the difference of two muon reconstruction algorithms (Staco and MuID). The uncertainties obtained are about 0.3%. However 1% error is assigned as the trigger scale factor uncertainty since full systematic error study had not beed performed.

2.8.2 Reconstruction Efficiency

The efficiency of reconstructing the STACO combined muon is measured also using the "tag-and-probe" method on the muons of the Z boson decay as described in [17]. The measured efficiency from the simulation agrees well with the data and the average reconstruction efficiency is about $\sim 93\%$. The scale factor to correct the MC efficiency to data efficiency is close to one and is obtained using the "MuonEfficiencyCorrections" package provided by the MCP group. The tool also provides the statistical uncertainty on the correction scale factor. The average statistical uncertainty is $\sim 0.5\%$. The systematic uncertainty on the correction scale factor is in the order of $\sim 0.2\%$ [18]. The combined total uncertainty on the correction scale factor is $\sim 0.7\%$ (adding the statistical error and systematic error linearly as suggested in [18]).

2.8.3 Muon momentum scale and resolution

The muon momentum resolution is measured from the width of the di-muon mass distribution in the $Z \rightarrow \mu\mu$ and external constraint from the analysis of toroid-off data. The "MuonMomentumCorrections" tool from the MCP group [18] is used to smear the muon momentum resolution in the MC to match with data. To estimate the effect of the momentum resolution uncertainty on the acceptance of the $W(\mu\nu)+\gamma$ and $Z(\mu\mu)+\gamma$ signals, we repeat the analysis by varying the "THESTRING" input variable in the "mcp_smear.PTVar" method with values of "MSLOW", "MSUP", "IDLOW" and "IDUP". The relative change in the acceptance of the $W(\mu\nu)+\gamma$ signal is $\sim 0.4\% - 1\%$, and $\sim 0.1\% - 0.3\%$ for the $Z(\mu\mu)+\gamma$ signal.

2.8.4 Muon isolation

In the $W\gamma$ and $Z\gamma$ analysis for the muon decay channel, a selected muon candidate must pass the relative isolation cut $\sum p_T^{ID}(cone20)/p_T < 0.1$. We do not assign an uncertainty on the isolation efficiency based on studies from the WZ and ZZ measurements. In the WZ measurement [19], which is also performed on the same dataset ($L \sim 1$ fb^{-1}) as this measurement, an identical muon isolation cut is applied to select the muon candidate. The efficiency of the muon isolation cut is studied using a tag-and-probe method on $Z \rightarrow \mu\mu$ selected events. The variations of the isolation efficiency has been examined for different data taking periods and between data and MC. The variation, which is taken as the systematic uncertainty, is found to be neligible. The ATLAS ZZ analysis [20], which is also performed over the same dataset and applies similar muon isolation cut ($\sum p_T^{ID}(cone20)/p_T < 0.15$) to select the muon candidates, found an uncertainty of 0.1% is for the muon isolation efficiency.

2.9 Photon Efficiency

2.9.1 Photon Efficiency definition

Photon selection efficiency $\varepsilon_\gamma^{\rm sel}$ can be broken down into three components : photon reconstruction efficiency $\varepsilon_\gamma^{\rm reco}$, photon identification efficiency $\varepsilon_\gamma^{\rm ID}$, and photon isolation efficiency $\varepsilon_\gamma^{\rm iso}$.

- The photon reconstruction efficiency $\varepsilon_\gamma^{\rm reco}$ is defined as the fraction of generated photons within the fiducial region of the measurement that match a reconstructed photon with the offline kinematic and geometric selection ($E_T > 15GeV$, $|\eta| < 2.37$). This efficiency will not be calculated explicitly but it will be absorbed in the α_{reco} component of the C_W/C_Z factors in Sec. 5.
- The photon identification efficiency $\varepsilon_\gamma^{\rm ID}$ is defined as the fraction of reconstructed photons in the fiducial region passing also the "tight" identification selection criteria.
- The photon isolation efficiency $\varepsilon_\gamma^{\rm iso}$ is the fraction of "tight" photons passing also the isolation cut $E^{iso} < 6$ GeV.

2.9.2 The Main Method for Estimation of Photon identification efficiency and its systematic uncertainty

MC based Fudge factor approach is used as the main method to estimate photon identification efficiency. The nominal photon identification efficiency $\varepsilon_\gamma^{\rm ID}$ is calculated using photons in $W\gamma$ and $Z\gamma$ Monte Carlo with fudge factor corrections [21]. Fudge factor corrections approximate the discrepancy between the discriminating variables (DV) distributions in data and MC by a small shift. Fudge factors for each DV is defined in Eq. 1 [21].

$$\Delta\mu^t_{DV} =< DV^t_{data} > - < DV^t_{MC} > \quad (1)$$

Fudge factors for each DV are obtained by comparing data and MC shower shapes of selected photon candidates passing the $W/Z+\gamma$ selection cuts. The index t indicates photon tight quality requirements the candidates used for the comparison satisfy. The fudge factor is obtained from Egamma group by comparing data and rel 16 Monte Carlo photon shower shape is documented in FudgeMCtool in Ref [22]. We applied the fudge factor on the signal $W/Z+\gamma$ Monte Carlo to correct the photon shower shape, and the central values of the photon identification efficiency (obtained after the correction) are shown in Table 24 and Table 25.

The list of systematic uncertainties considered for the photon identification efficiency is given below:

- uncertainty on fudge factor due to background contamination: evaluate this systematic by calculating correction factors on tight photon selection level μ^{tight}_{DV}, and loose selection level (μ^{loose}_{DV}), compare the discrepancy between two sets of fudge correction factor.

- uncertainty on fudge factor due to simple shift approximation: evaluate this systematic by performing the whole fudge factor correction procedure on photons in distorted material Monte Carlo samples with respect to photons in nominal geometry samples. Photon MC efficiency in nominal geometry samples with fudge factor correction is supposed to approximate the true MC efficiency in distorted material samples[21] if simple shift approximation is valid. Take the difference of two efficiencies as uncertainty on simple shift approximation.

- The impact of the hadronization model on the efficiency has been evaluated comparing sample with Pythia and Herwig hadronization models. Differences are found to be within 1.5% [21].

- The impact of upstream material uncertainty has been assessed by comparing photon efficiencies from nominal photon Monte Carlo samples with those obtained with Monte Carlo samples simulated with additional material[21].

- The impact of the classification between converted and unconverted photons is studied in MC artificially altering the conversion algorithm efficiency. Reconstructed photons that are wrongly classified as converted or unconverted can impact the identification efficiency given the different requirements applied on each category of photons. The uncertainty due to this effect is estimated to be within 1-2% (depending on η_γ).

- The impact due to high pileup environment in 2011 collision data is considered to be 2% (recommendations from Egamma group)

- Uncertainty due to fragmentation photons contribution : fragmentation photons productions are included in signal $W\gamma$ and $Z\gamma$ Monte Carlo. Variating the fractions of fragmentation photons in signal Monte Carlo by $\pm$ 50%, the variation of photon efficiency is considered as uncertainty due to fragmentation photons contribution.

Table 6 showed an example of the list of absolute systematic uncertainty and its contributions to low p_T photon efficiency. The relative uncertainty due to uncertainty of photon efficiency is shown in Table 26 and Table 27. Table 6 shows the systematic uncertainty for photons with $p_T > 15GeV$ and $p_T > 60GeV$. We assume the systematic uncertainty for high p_T photons with $p_T > 100GeV$ is similar to that of for p_T photons with $p_T > 60GeV$. It is found that the discrepancy in shower shape ($\Delta\mu^t_{DV}$) between data/MC become small in high region and the uncertainty due to upstream material drops as a function of photon p_T, it should be safe to assume that high p_T ($p_T > 100GeV$)photons have the same systematic uncertainty as medium p_T ($p_T > 60GeV$) photons.

Source of Systematic Uncertainty	$\Delta\varepsilon/\varepsilon$ $p_T > 15GeV$	$\Delta\varepsilon/\varepsilon$ $p_T > 60GeV$
Systematic uncertainty due to simple shift approximation	2.4%	1.4%
Systematic uncertainty due to background contamination	3.1%	1.5%
Hadronization model	1.0%	1.0%
Photons from fragmentation efficiency	1.5%	1.8%
EM scale uncertainty on photon ID	negligible	negligible
uncertainty of up stream material	6.0%	1.6%
uncertainty due to bad conversion reconstruction	1.2%	0.9%
Pile up uncertainty	2%	2%
Overall uncertainty	7.8 %	4.1%

Table 6: Contributions to the overall absolute systematic uncertainty on the photon reconstruction and offline identification efficiency

2.10 Acceptance in Missing Transverse Energy

The acceptance of the MET cut, which is applied in the $W\gamma$ analysis, is obtained from MC. We follow the procedure used by the ATLAS WW measurement [23] to evaluate the systematic uncertainty on the MET acceptance. The procedure consists of four components :

- MuonBoy term : In section 2.5 we mentioned that in the $W(\mu\nu)+\gamma$ analysis the MET is corrected by replacing the energy loss by the muon in the calorimeter with the muon momentum measured by the muon spectrometer and inner detector ("combined" momentum). To evaluate the systematic uncertainty of the muon correction on the MET we replace the muon "combined" momentum with the momentum measured by the muon spectrometer for the MET correction. This is only done for the case where the muon is isolated ($\Delta R(\mu, jet) > 0.3$, where the jet is of cone size 0.6, calibrated at LC scale, and has $p_T > 7$ GeV).

- Cell-out term : The calorimeter component of the MET receives contributions from physics objects (e.g. electron and jets) and from other un-clustered energies (cell-out). To evaluate the uncertainties from the un-clustered energies, A dedicated study has been done and documented in Ref [24], the conclusion is that the scale uncertainties on un-clustered energies is 13.2%. we vary the "cell-out" contribution to the MET by $\pm 13.2\%$.

- In-time pileup : Studies show the MET resolution width increases with increase in the number of collision vertices. The difference in the resolution width between data and MC is found to be less than 3%. Thus the uncertainty on the MET acceptance due to in-time pileup is determined by varying the MET by $\pm 3\%$.

- Out-of-time pileup : The out-of-time pileup is the effect of the detector responses in one bunch crossing affects the detector measurement in adjcent bunch crossing. The MC simulation of the bunch train luminosity profile does not match that in the data, especially in the bunches early in train, which corresponds to $\sim 33\%$ of all the bunches in the train. In order to let MC reproduce the pileup effect in data. Addtional smearing on MC is needed. It is seen that in WW analysis [23], the required smearing appears to be roughly constant, without dependency on the Emiss cut or number of vertices, and lies in the range 3-5 GeV. Following the approach from WW analysis, we smear the MET by 5 GeV in 33% of the signal MC events to evaluate the systematic uncertainty due to this effect.

	$W\gamma \to e\nu\gamma$					
	$p_T(\gamma) > 15GeV$		$p_T(\gamma) > 60GeV$		$p_T(\gamma) > 100GeV$	
	$N_{jet} = 0$	$N_{jet} >= 0$	$N_{jet} = 0$	$N_{jet} >= 0$	$N_{jet} = 0$	$N_{jet} >= 0$
Cell Out	0.5%	0.2%	0.5%	0.3%	1.4%	1.1%
In-Time Pileup	2.6%	2.5%	2.5%	2.0%	2.9%	2.0%
Out-Of-Time Pileup	0.3%	0.3%	0.3%	0.3%	0.4%	0.8%
Total Uncertainty	2.7%	2.5%	2.6%	2.0%	3.2%	2.4%
	$W\gamma \to \mu\nu\gamma$					
	$p_T(\gamma) > 15GeV$		$p_T(\gamma) > 60GeV$		$p_T(\gamma) > 100GeV$	
	$N_{jet} = 0$	$N_{jet} >= 0$	$N_{jet} = 0$	$N_{jet} >= 0$	$N_{jet} = 0$	$N_{jet} >= 0$
MuonBoy	0.5%	0.2%	0.3%	0.2%	0.7%	0.7%
Cell Out	0.6%	0.4%	0.2%	0.3%	0.4%	0.4%
In-Time Pileup	2.7%	2.5%	2.7%	2.2%	2.7%	1.9%
Out-Of-Time Pileup	1.1%	1.0%	1.0%	0.7%	1.1%	0.6%
Total Uncertainty	3.0%	2.7%	2.9%	2.3%	3.0%	2.1%

Table 7: Systematic uncertainties from various components that are related to the missing transverse energy measurement for the $W gamma$ analysis in the electron and muon decay channels.

The total MET systematic uncertainty is obtained by summing the uncertainties from these four components in quadrature. The results are presented in Table 7.

2.11 Acceptance uncertainty from jet energy scale, resolution and jet reconstruction efficiency

Jet energy scale uncertainty is evaluated by Jet/MET group from Monte Carlo simulation and validated by data using $\gamma + jet$ events and multi-jets events, the impact of jet energy scale uncertainty(JES) and jet resolution uncertainty to signal efficiency is estimated by varying the jet uncertainty scale by one sigma of JES to each jet in signal MC simulation samples and add addtional smearing, which is corresponding to one sigma of jet energy resolution, to each jet in signal MC simulation. This study is documented in Table 26 and Table 27 of section 5. About 5% level variations for signal acceptance for cross section measurement with jet veto cuts. The jet reconstruction efficiency was found in simulation signal MC samples to be close to 100% for jets with $p_T > 30GeV$, The jet reconstruction efficiency is very ideal, no addtional systematic for jet reconstruction efficiency is quoted.

3 Background Determination and Signal Yield

Although all the photon selection criteria, applied on our selection of W and Z bosons, are very effective in rejecting background, part of the total events representing our final sample of photon candidates are produced by processes different from $W\gamma$ and $Z\gamma$.

The dominant sources of background for this analysis are from $W(Z)$+jets events where photons from the decay products of mesons produced by the jet fragmentation (mainly $\pi^0 \to \gamma\gamma$) pass the photon selection criteria. Since the fragmentation functions of quarks and gluons into hadrons are poorly constrained by experiments, these processes are not well modeled by $W(Z)$+jets MC simulations.

Another source background to $W\gamma$, which is not well modeled by MC simulations, is $\gamma + jets$ process. There is no real MET and real lepton in this kind of events. However, due to the large production cross section of $\gamma + jets$ process, this kind of background events can be still misidentified as $W\gamma$ events, when hadrons inside jets faked as leptons, or there are leptons from heavy flavour decays of jets in the event and fake MET is created by pileup background or mismeasurement of jets energy in the event.

Additional backgrounds from other processes, such as $W \to \tau\nu$, $t\bar{t}$, single-Top, WW and $Z \to e^+e^-(\mu^+\mu^-)$ (misidentified as $W\gamma$) for the $W\gamma$ analysis, and $t\bar{t}$ for the $Z\gamma$ analysis will be referred to collectively as "EW+TOP background" (EWbkg) and their contribution are estimated from MC simulation.

Since the processes of a jet faking a photon and jet faking leptons are not well modeled in the current Monte Carlo simulation, we use data-driven methods to estimate the amount of $W+jets$ and $\gamma+jets$ background events present in our $W\gamma$ selected events, and to estimate the amount of $Z+jets$ background in the $Z\gamma$ selected events.

3.1 Data driven method for estimating W+jets backgrounds

A two-dimensional sideband method (2D sideband method or so–called ABCD method) is used in order to estimate the jet–fake contamination in the data sample. Here the two dimensions are given by the isolation of the photon candidate on one axis and its "tightness" on the other one. Hence, three background control regions and one signal region are defined as follows:

- Tight and isolated region (signal region A): candidates that have an isolated ($E_T^{iso(R<0.3)} < 6$ GeV) photon passing the tight selection criteria;
- Tight but not-isolated region (control region B): candidates that have a non-isolated photon ($E_T^{iso(R<0.3)} >$ 7 GeV) passing the tight selection criteria;
- Not-tight and isolated region (control region C): candidates that have an isolated ($E_T^{iso(R<0.3)} < 6$ GeV) photon passing the not-tight selection criteria;
- Not-tight and not-isolated region (control region D): candidates that have a non-isolated ($E_T^{ISO(R<0.3)} >$ 7 GeV) photon passing the not-tight selection criteria.

Not-tight photons are defined as those ones which pass all the calorimeter middle layer shower shape cuts and the hardronic leakage cut, but fail at least one of three (w_{s3},F_{side},ΔE) of the first layer shower shape variables. The choice of the shower shape variables to be used to define the background control region is driven mainly by two criteria: on one hand the requirement that correlations between the isolation of the photon and its "tightness" are negligible, so that the extrapolation of the background counts from the control regions to the signal region can be safely performed; on the other hand the need to reduce the signal contamination in the control regions [3].

The method is in fact based on the following two assumptions:

- The presence of signal events in the three control regions (B, C, and D) is negligible. This allow us to consider all reconstructed photons falling in one of these regions as coming from a background event. The fraction coming from jet-faking events N^{jetbkg} can then be extracted subtracting the contribution from electroweak+TOP backgrounds N^{EWbkg} (estimated from Monte Carlo) from the total number of observed events in each of these three regions:

$$N_A = (N_A^{w\gamma} + N_A^{\gamma jet}) + N_A^{wjet} + N_A^{EWbkg} \tag{2}$$

$$N_B = N_B^{wjet} + N_B^{EWbkg} \tag{3}$$

$$N_C = N_C^{wjet} + N_C^{EWbkg} \tag{4}$$

$$N_D = N_D^{wjet} + N_D^{EWbkg} \tag{5}$$

[3] The assumption that the signal contamination is small in the control region is checked using the $W+\gamma$ and $Z+\gamma$ signal Monte Carlo Sample **??**

- The ratio of isolated to non-isolated background candidates from jet–fake in the not–tight bins ($\frac{N_D^{wjet}}{N_C^{wjet}}$) is equal to the same ratio computed in the tight bins ($\frac{N_B^{wjet}}{N_A^{wjet}}$).

Assuming that these statements are valid, the $W + jet$ background in region A can be calculated as follows:

$$N_A^{wjet} = (N_B - N_B^{EWbkg})\frac{N_C - N_C^{EWbkg}}{N_D - N_D^{EWbkg}} \tag{6}$$

It is found, based on Monte Carlo studies, that these assumptions are only approximately true. In particular the signal leakage in the background control regions may not always be negligible, since there is a small fraction of real photons coming from $W+\gamma$ and $\gamma+jet$ processes which fails photon identification cuts or photon isolation cuts. Also, a small correlation between isolation and tightness of the photon might introduce a bias in the background estimation. To take these effects into account in our computation, we define:

$$N_A^{W\gamma}+N_A^{\gamma jet} = (N_A - N_A^{EWbkg}) - \frac{1}{R^{Wjet}}\frac{(N_B - N_B^{EWbkg} - c_B(N_A^{W\gamma}+N_A^{\gamma jet}))(N_C - N_C^{EWbkg} - c_C(N_A^{W\gamma}+N_A^{\gamma jet}))}{N_D - N_D^{EWbkg} - c_D(N_A^{W\gamma}+N_A^{\gamma jet})} \tag{7}$$

Then by solving Equation 7, we obtain:

$$N_A^{Wjet} = N_A - N_A^{EWbkg} - (N_A^{W\gamma}+N_A^{\gamma jet}) = N_A - N_A^{EWbkg} - \frac{E*(-1+\sqrt{1+F})}{G} \tag{8}$$

Where

- $R^{Wjet} = \frac{N_B^{Wjet}N_C^{Wjet}}{N_A^{Wjet}N_D^{Wjet}}$ is defined to account for the bias on isolation due to reverse-cuts procedure;
- $C_X = \frac{N_X^{W\gamma(\gamma jet)}}{N_A^{W\gamma(\gamma jet)}}$, X=(B,C,D) is defined to take into account the leakage of real photon from $W+\gamma$ and $\gamma + jet$ into control regions B, C, D;
- $E = N_D - N_D^{EWbkg} + (N_A - N_A^{EWbkg})*C_D - (N_B - N_B^{EWbkg})*C_C/R^{wjet} - (N_C - N_C^{EWbkg})*C_B/R^{wjet}$;
- $F = \frac{4(C_B*C_C/R^{wjet}-C_D)*((N_A-N_A^{EWbkg})*(N_D-N_D^{EWbkg})-(N_C-N_C^{EWbkg})*(N_B-N_B^{EWbkg})/R^{wjet})}{E^2}$;
- $G = 2*(C_B*C_C/R^{wjet} - C_D)$.

The signal leakage C_X is estimated using the signal $W+\gamma$ Monte Carlo, assuming that the leakage is similar for real photons coming from $W+\gamma$ and $\gamma+jet$ process, whereas, when computing the measurement central value, the R^{Wjet} factor is fixed to 1. A systematic uncertainty is associated to this assumption.

3.2 Data driven method for estimating γ+jets background

In γ+jets events there are no real missing E_T or real isolated leptons, however jets coming from γ+jets events could be misidentified as leptons, and a high missing E_T could be recontructed in these events, due to pile-up events in the calorimeters and mis-measurements of the jets energy. Although the probability of a γ+jets event being reconstructed as a signal event is low, the large production cross–section of such events makes this contamination non–negligible in the final $W\gamma$ candidates sample.

In order to estimate the γ+jets contamination, the ABCD method is used. Hence, three background control regions are defined to estimate the amount of background in the signal region. The signal and the background regions in this two-dimensional plane are defined as follows:

- signal region A: candidates with one isolated lepton and $E_T^{miss} > 35$ GeV;
- control region B’: candidates with one non-isolated lepton and $E_T^{miss} > 35$ GeV;
- control region C’: candidates with one isolated lepton and $E_T^{miss} < 20$ GeV;
- control region D’: candidates with one non-isolated lepton and $E_T^{miss} < 20$ GeV.

Details on the regions definition, in particular for what concerns the isolation selection for both the electronic and the muonic case, are provided in Table 8.

In order to have enough statistics in the background control regions to perform the γ+jets data driven estimate, some additional cut inversions were performed in the C’ and D’ background regions. In these two regions, and in the electronic channel, no selection on the W candidate transverse mass is performed; furthermore, in the muon channel both the W transverse mass selection and the transverse impact parameter selection are reversed. In particular, in the muon channel C’ and D’ regions, we require that $M_T^W < 40$ GeV and $|d_0/\sigma(d_0)| \geq 3$.

region	$E_T^{iso(\Delta R<0.3)(\text{electron})}$ [GeV]	$\sum p_T^{track(\Delta R<0.3)(\text{muon})}/p_T^{(\text{muon})}$	MET [GeV]
A	< 6	< 0.15	> 35
B’	< 6	> 0.17	> 35
C’	> 7	< 0.15	< 20
D’	> 7	> 0.17	< 20

Table 8: AB’C’D’ regions definition for γ+jet background estimation for both electronic and muonic channels.

Assuming, in analogy with what presented in the previous section, that the W+jet and the W+γ contaminations are negligible in the background control regions (B’, C’ and D’) and that the correlation between the missing transverse energy of the event and the lepton isolation is small, the number of γ+jets events in the signal region can be computed as follows:

$$N_A^{\gamma jet} = (N_{B'} - N_{B'}^{EWbkg})\frac{N_{C'} - N_{C'}^{EWbkg}}{N_{D'} - N_{D'}^{EWbkg}} \tag{9}$$

As discussed in the case of the W+jets background, these assumptions are not fully satisfying, especially for what concerns the leakage of W+jets and γ+jets events in the background control regions. When this contamination is accounted for in Equation 9, the following formula for the γ+jets background counts in region A is obtained:

$$N_A^{\gamma jet} = N_A - N_A^{EWbkg} - (N_A^{W\gamma} + N_A^{wjet}) = N_A - N_A^{EWbkg} - \frac{E' * (-1 + \sqrt{1+F'})}{G'} \tag{10}$$

Where

- $R^{\gamma jet} = \frac{N_{B'}^{\gamma jet} N_{C'}^{\gamma jet}}{N_A^{\gamma jet} N_{D'}^{\gamma jet}}$ is defined to account for the bias on isolation due to reverse-cuts procedure;
- $C'_X = \frac{N_X^{W\gamma(Wjet)}}{N_A^{W\gamma(Wjet)}}$, X=(B’,C’,D’) is defined to account for leakage of from $W+\gamma$ and $W+jet$ into control regions B’, C’, D’;
- $E' = N_{D'} - N_{D'}^{EWbkg} + (N_A - N_A^{EWbkg}).C_{D'} - (N_{B'} - N_{B'}^{EWbkg})\frac{C_{C'}}{R^{\gamma jet}} - (N_{C'} - N_{C'}^{EWbkg})\frac{C_{B'}}{R^{\gamma jet}}$;
- $F' = \frac{4(\frac{C_{B'}.C_{C'}}{R^{\gamma jet}} - C_{D'}).((N_A - N_A^{EWbkg}).(N_D - N_{D'}^{EWbkg}) - \frac{(N_C - N_{C'}^{EWbkg}).(N_{B'} - N_{B'}^{EWbkg})}{R^{\gamma jet}})}{E'^2}$;

- $G' = 2.(\frac{C_{B'}.C_{C'}}{R^{\gamma jet}} - C_{D'})$.

Here, the signal leakage C'_X is estimated using the signal $W+\gamma$ Monte Carlo, assuming that it is similar for real photons coming from $W+\gamma$ and $\gamma + jet$ process, whereas, when computing the measurement central value, the $R^{\gamma jet}$ factor is fixed to 1. A systematic uncertainty is associated to this assumption.

3.3 Extrapolation methods for $W+jet$,$Z+jet$ and γjet

Two dimensions sideband methods (or template methods) are used as baseline method for $W+jet$, $Z+jet$ and γjet background estimation. However this method suffers from low statistics issue in high pT, zero jet phase space ($N_{jet}=0$ and $p_{T\gamma} > 60GeV$ or $p_{T\gamma} > 100GeV$, detailed phase space definition is shown in table 22). Extrapolation methods based on N_{jet} distribution in control region is used as baseline methods for those phase space. Here we describe two extrapolation methods ($p_{T\gamma}$ based extrapolation and N_{jet} based extrapolation method).

Example of Extrapolation methods based on two dimensions sideband methods

As an example, we describe how to obtain $W+jet$ background estimation in high $p_{T\gamma}$ phase space (eg: $p_{T\gamma} > 60GeV$ and $N_{jet}=0$) using these two extrapolation methods.

- $p_{T\gamma}$ based extrapolation:

  - obtain N_A^{wjet} in low $p_{T\gamma}$ phase space ($p_{T\gamma} > 15GeV$ and $N_{jet}=0$) using 2D sideband method.
  - get $p_{T\gamma}$ distribution ($f(p_{T\gamma})$) for $W jet$ background from non-tight regions (control region C,D).
  - Then $N_A^{wjet}(p_{T\gamma} > 60GeV, N_{jet}=0) = \int_{60GeV}^{inf} N_A^{wjet}(p_{T\gamma} > 15GeV, N_{jet}=0) f(p_{T\gamma}) d(p_{T\gamma})$

- N_{jet} based extrapolation:

  - obtain N_A^{wjet} in low $p_{T\gamma}$ phase space ($p_{T\gamma} > 60GeV$ and $N_{jet} >= 0$) using 2D sideband method.
  - get N_{jet} distribution ($f(N_{jet})$) for $W jet$ background from non-tight regions (control region C,D).
  - Then $N_A^{wjet}(p_{T\gamma} > 60GeV, N_{jet}=0) = N_A^{wjet}(p_{T\gamma} > 60GeV, N_{jet} >= 0).f(N_{jet}=0)$

Example of Extrapolation methods based on template methods

Here is another example for how to estimate γ+jets background in high p_T region using extrapolation method.

For the N_{jet} based extrapolation method we first start off with using the template method to estimate the γ+jets background for the $W\gamma$ analysis with $NJet >= 0$ and for a specific p_T^γ threshold. We then obtain a $NJet$ distribution in the data in the regio $Iso > 0.2$ with all the non-γ+jets backgrounds subtracted away. The resulting $NJet$ distribution, which we assume to represent the γ+jets background, is normalized to the initially estimated γ+jets background (using the template method) for the $W\gamma$ analysis with $NJet >= 0$. The entries in the $NJet = 0$ bin of the normalized $NJet$ distribution is the amount of γ+jets background in the signal region of $W\gamma$ analysis with $NJet = 0$ for that specific p_T^γ threshold.

For the photon p_T extrapolation method we first start off with using the template method to estimate the γ+jets background for the $W\gamma$ analysis with $NJet = 0$ for $p_T^\gamma > 15$ GeV. We then obtain a p_T^γ distribution in the data in the regio $Iso > 0.2$ with all the non-γ+jets backgrounds subtracted away. The resulting p_T^γ distribution, which we assume to represent the γ+jets background, is normalized to the initially estimated γ+jets background (using the template method) for the $W\gamma$ analysis with $NJet = 0$ and $p_T^\gamma > 15$ GeV. The entries in the p_T^γ >60 or 100 GeV region of the normalized p_T^γ distribution is the amount of γ+jets background in the signal region of $W\gamma$ analysis with $NJet = 0$ for p_T^γ >60 or 100 GeV.

Figure **??** is the extracted $NJet$ distribution in the region $Iso > 0.2$ (after subtracting away the contributions from other background sources) and have normalized to the estimated γ+jets background events (based on the template method) for the $W\gamma$ analysis with $p_T^\gamma > 15$ GeV and $NJet >= 0$ ($N(\gamma + jets) = 67.3 \pm 7.6$). There are 16.7 events in the $NJet = 0$ bin which corresponds to the amount of γ+jets background for the $W\gamma$ analysis at $p_T^\gamma > 15$ GeV and $NJet = 0$.

3.4 Summary of backgrounds estimation for W+γ

As discussed in section 3.1 that $W jet$ and γjet background to $W\gamma$ are estimated from data driven method according to Equation 8 and Equation 10, "EW+$t\bar{t}$ background" to $W\gamma$ are estimated from MC simulation. The input parameters (number of events in A,B,C,D region and leakage factors) to Equation 8 for $W + jet$ background estimation are given in Table **??**(Appendix) for electron channel and in Table **??** (Appendix) for muon channel. The input parameters to Equation 10 for $\gamma + jet$ background estimation in electron channel are given in Table **??**(Appendix). A summary of the each components of background contribution and signal yield are given in Table 9. The factor $R^{W jet}$ and $R^{\gamma jet}$ is assumed to be equal to 1, the systematic error due to this assumeption will be discussed in section 3.6. Figure **??** is showing the photon isolation shape (before photon isolation cut) comparison between data and Monte Carlo simulations, the number of expected signal is normalized to data and the number of expected background is taken from Table 9. According to Figure **??**, the photon isolation distributions in data in both channels are described reasonablely by Monte Carlo simulations, which indicates that non-isolated photons from $W jet$ background are under control. Figure **??** and Figure **??** are showing the lepton isolation shape (before lepton isolation cut) comparison between data and Monte Carlo simulations. They are also in reasonablely good agreement, which indicates that non-isolated leptons from γjet background are also under control.

background	$pp \to e\nu\gamma$	$pp \to \mu\nu\gamma$	$pp \to e\nu\gamma$	$pp \to \mu\nu\gamma$
	$15GeV < p_T(\gamma) < 20GeV, N_{jet} \geq 0$		$15GeV < p_T(\gamma) < 20GeV, N_{jet} = 0$	
observed events	2424	3294	1603	2254
W+jet	$731.1 \pm 179.2 \pm$	$1276.9 \pm 264.2 \pm$	$\pm\pm$	$\pm\pm$
γ+jet	$217.8 \pm 45.0 \pm$	$65.3 \pm 8.2 \pm$	$\pm\pm$	$\pm\pm$
$Z \to ll$	129.4 ± 7.7	194.7 ± 9.4	48.6 ± 4.7	143.3 ± 8.0
$t\bar{t}$	66.1 ± 3.5	87.5 ± 4.0	1.1 ± 0.5	1.8 ± 0.6
Single Top	6.3 ± 0.8	13.9 ± 1.6	0.4 ± 0.2	2.1 ± 0.6
WW	10.8 ± 0.9	15.1 ± 1.2	5.6 ± 0.4	7.4 ± 0.5
extracted signal	$\pm\pm$	$\pm\pm$	$\pm\pm$	$\pm\pm$
background	$pp \to e\nu\gamma$	$pp \to \mu\nu\gamma$	$pp \to e\nu\gamma$	$pp \to \mu\nu\gamma$
	$20GeV < p_T(\gamma) < 30GeV, N_{jet} \geq 0$		$20GeV < p_T(\gamma) < 30, N_{jet} = 0$	
observed events	2369	3470	1427	2141
W+jet	$581.4 \pm 131.3 \pm$	$899.0 \pm 161.6 \pm$	$\pm$	$\pm$
γ+jet	$363.7 \pm 69.2 \pm$	$61.1 \pm 7.4 \pm$	$\pm$	$\pm$
$Z \to ll$	255.0 ± 10.7	287.1 ± 11.3	140.8 ± 8.0	208.2 ± 9.7
$t\bar{t}$	96.4 ± 4.2	146.6 ± 5.2	3.4 ± 0.8	4.3 ± 0.9
Single Top	8.9 ± 1.0	21.7 ± 1.8	0.9 ± 0.3	2.1 ± 0.5
WW	20.2 ± 1.2	31.1 ± 1.1	12.0 ± 0.5	19.3 ± 0.7
extracted signal	$\pm\pm$	$\pm\pm$	$\pm\pm$	$\pm\pm$
background	$pp \to e\nu\gamma$	$pp \to \mu\nu\gamma$	$pp \to e\nu\gamma$	$pp \to \mu\nu\gamma$
	$30GeV < p_T(\gamma) < 40GeV, N_{jet} \geq 0$		$30GeV < p_T(\gamma) < 40GeV, N_{jet} = 0$	
observed events	907	1710	468	894
W+jet	$407.8 \pm 118.1 \pm$	$230.8 \pm 66.1 \pm$	$\pm\pm$	$\pm$
γ+jet	$273.3 \pm 56.6 \pm$	$33.1 \pm 4.5 \pm$	$\pm$	$\pm$
$Z \to ll$	133.8 ± 7.8	166.1 ± 8.7	82.3 ± 6.1	123.5 ± 7.5
$t\bar{t}$	50.9 ± 3.1	122.2 ± 4.8	0.9 ± 0.4	3.2 ± 0.8
Single Top	6.5 ± 0.9	14.3 ± 1.5	0.6 ± 0.3	0.7 ± 0.5
WW	11.8 ± 0.8	28.8 ± 0.9	7.5 ± 0.5	18.2 ± 0.7
extracted signal	$\pm\pm$	$\pm\pm$	$\pm\pm$	$\pm\pm$
background	$pp \to e\nu\gamma$	$pp \to \mu\nu\gamma$	$pp \to e\nu\gamma$	$pp \to \mu\nu\gamma$
	$40GeV < p_T(\gamma) < 60GeV, N_{jet} \geq 0$		$40GeV < p_T(\gamma) < 60GeV, N_{jet} = 0$	
observed events	827	1325	377	611
W+jet	$150.9 \pm 52.5 \pm$	$352.2 \pm 78.8 \pm$	$\pm$	$\pm$
γ+jet	$172.3 \pm 40.5 \pm$	$31.6 \pm 3.9 \pm$	$\pm$	$\pm$
$Z \to ll$	85.7 ± 6.2	97.7 ± 6.6	53.1 ± 4.9	57.8 ± 5.1
$t\bar{t}$	54.0 ± 3.2	147.7 ± 5.2	2.7 ± 0.7	4.4 ± 0.9
Single Top	6.0 ± 0.8	23.0 ± 1.8	0.3 ± 0.2	2.0 ± 0.5
WW	12.3 ± 0.8	37.2 ± 1.1	7.5 ± 0.4	22.8 ± 0.8
extracted signal	$\pm\pm$	$\pm\pm$	$\pm\pm$	$\pm\pm$
background	$pp \to e\nu\gamma$	$pp \to \mu\nu\gamma$	$pp \to e\nu\gamma$	$pp \to \mu\nu\gamma$
	$60GeV < p_T(\gamma) < 100GeV, N_{jet} \geq 0$		$60GeV < p_T(\gamma) < 100GeV, N_{jet} = 0$	
observed events	554	802	191	272
W+jet	$42.8 \pm 21.1 \pm$	$18.1 \pm 25.5 \pm$	$\pm$	$\pm$
γ+jet	$47.5 \pm 16.4 \pm$	$12.8 \pm 2.0 \pm$	$\pm$	$\pm$
$Z \to ll$	56.8 ± 5.1	25.7 ± 3.5	22.1 ± 3.2	13.4 ± 2.5
$t\bar{t}$	40.7 ± 2.7	113.3 ± 4.6	0.2 ± 0.2	5.3 ± 1.0
Single Top	4.5 ± 0.7	15.0 ± 1.5	0.8 ± 0.3	1.9 ± 0.6
WW	7.6 ± 0.4	22.8 ± 0.9	4.3 ± 0.3	12.9 ± 0.5
extracted signal	$\pm\pm$	$\pm\pm$	$\pm\pm$	$\pm\pm$
background	$pp \to e\nu\gamma$	$pp \to \mu\nu\gamma$	$pp \to e\nu\gamma$	$pp \to \mu\nu\gamma$
	$100GeV < p_T(\gamma) < 1TeV, N_{jet} \geq 0$		$100GeV < p_T(\gamma) < 1TeV, N_{jet} = 0$	
observed events	238	308	64	65
W+jet	$0.4 \pm 4.1 \pm$	$10.5 \pm 9.5 \pm$	$\pm\pm$	$\pm$
γ+jet	$14.8 \pm 8.3 \pm$	$0 \pm 0 \pm 0$	$\pm$	$\pm$
$Z \to ll$	11.8 ± 2.3	7.1 ± 1.8	4.5 ± 1.4	2.6 ± 1.1
$t\bar{t}$	14.7 ± 1.7	41.0 ± 2.7	0.6 ± 0.3	0.7 ± 0.3
Single Top	1.4 ± 0.4	6.1 ± 0.9	0.2 ± 0.1	0.6 ± 0.3
WW	2.9 ± 0.5	7.2 ± 0.5	0.9 ± 0.1	2.7 ± 0.2
extracted signal	$\pm\pm$	$\pm\pm$	$\pm\pm$	$\pm\pm$

Table 9: Expected number of backgroud events and observed signal yield afer all $W\gamma$ selection cuts in $pp \to e\nu\gamma$ channel and $pp \to \mu\nu\gamma$ channel for different fiducial phase space. The Detailed information

3.5 Summary of backgrounds estimation for Z+γ

Following the discussion in section 3.1 that $Zjet$ background to $Z\gamma$ are estimated from data driven method, "EW+$t\bar{t}$ background" to $Z\gamma$ are estimated from MC simulation.

A summary of the various components that enter the calculation of $N_A^{Z\gamma}$ and N_A^{Zjet} are given in Table. **??**. The factor R^{Zjet} is assumed to be equal to 1. Here we define the photon purity P of the photon candidate sample as

$$P = \frac{N_A^{Z\gamma}}{N_A - N_A^{EWbkg}}$$

Using the input from Table. **??** (Appendix), the purity of $Z\gamma$ events in data is calulated and summarized in Table 10. According to Table 10, the $Z\gamma$ signal purity in low γ pT region are very similar in electron channel and muon channel. Since the statistics for $Z\gamma$ candidates in data is very limited, especially in high pT region. We combine the statistics in e,μ channels for final number of $Z+jet$ background estimation, assuming they have similar signal purity both channels. Using e,μ channels combined purity in Table 10, $Z+jet$ background contribution and $Z\gamma$ signal yield are evaluated and given in Table 11. Figure **??** is showing the photon isolation shape (before photon isolation cut) comparison between data and $Z\gamma$ signal MC, the number of expected background is taken from 11.

channel	$pp \to e^+e^-\gamma$	$pp \to \mu^+\mu^-\gamma$	$pp \to l^+l^-\gamma$ (combined)
	$p_T(\gamma) > 15GeV, N_{jet} >= 0$		
purity	$90.4\% \pm 3.3$	$92.4\% \pm 2.4$	$91.5\% \pm 1.5\%$
	$p_T(\gamma) > 15GeV, N_{jet} >= 0$		
purity	$92.1\% \pm 3.9$	$93.0\% \pm 2.7$	$92.2\% \pm 1.7\%$
	$p_T(\gamma) > 60GeV, N_{jet} >= 0$		
purity	-	-	$89.8\% \pm 5.1\%$
	$p_T(\gamma) > 60GeV, N_{jet} = 0$		
purity	-	-	$93.4\% \pm 4.6\%$

Table 10: $Z\gamma$ signal purity in different fiducial phase space. Detailed definition of fiducial phase space is defined in Table 22.

3.6 Systematics on $W(Z)+jet$ Background Estimation

As described in the previous section, the extraction of the signal yield using the data driven method relies on the definition of the background control regions and on a number of assumptions. In this section the estimate of the impact of such choices and assumptions on the photon purity is evaluated and the associated systematic uncertainties on the measurements are computed.

Definition of non–isolated control region

The photon candidates of the selected signal events are required to have an isolation energy $E_T^{iso(R<0.3)} <$ 6 GeV. The non–isolated control region (regions B and D as defined in section 3.1) is chosen to have $E_T^{iso(R<0.3)} >$ 7 GeV. The impact on the measurement of the choice of this particular control region definition has been evaluated by varying the boundary value to 6 GeV or 8 GeV. The effects of these variations are summarized in table 12.

background source	$pp \to e^+e^-\gamma$	$pp \to \mu^+\mu^-\gamma$	$pp \to e^+e^-\gamma$	$pp \to \mu^+\mu^-\gamma$
	$p_T(\gamma) > 15GeV, N_{jet} >= 0$		$p_T(\gamma) > 15GeV, N_{jet} = 0$	
total observed events	514	634	376	495
Z+jet	$43.7 \pm 7.7 \pm 14.6$	$53.6 \pm 9.7 \pm 12.8$	$29.3 \pm 6.4 \pm 8.9$	$38.6 \pm 8.6 \pm 13.2$
$t\bar{t}$	0	2.5 ± 0.5	0	0
$Z \to \tau\tau$	0	0.7 ± 0.7	0	0.7 ± 0.7
extracted signal	$470.3 \pm 23.0 \pm 14.6$	$577.2 \pm 25.9 \pm 12.8$	$346.7 \pm 19.7 \pm 8.9$	$455.8 \pm 23.0 \pm 13.2$
	$p_T(\gamma) > 60GeV, N_{jet} >= 0$		$p_T(\gamma) > 60GeV, N_{jet} = 0$	
total observed events	40	46	24	32
Z+jet	$4.1 \pm 2.0 \pm 2.4$	$4.6 \pm 2.4 \pm 2.2$	$1.6 \pm 1.1 \pm 1.3$	$2.1 \pm 1.5 \pm 1.6$
$t\bar{t}$	0	0.5 ± 0.3	0	0
$Z \to \tau\tau$	0	0	0	0
extracted signal	$35.9 \pm 6.3 \pm 2.4$	$40.9 \pm 6.8 \pm 2.2$	$22.4 \pm 4.9 \pm 1.3$	$29.9 \pm 5.7 \pm 1.6$

Table 11: Expected number of electroweak backgroud events afer all $Z\gamma$ selection cuts in $pp \to e^+e^-\gamma$ channel and $pp \to \mu^+\mu^-\gamma$ channel in different fiducial phase space. Detailed definition of fiducial phase space is defined in Table 22.

Definition of non–tight control region

The non–tight control region (regions C and D as defined in section 3.1) is obtained by inverting at least one out of three shower shape variables (w_{s3}, F_{side}, ΔE) used in the PhotonTightSelection definition (here called $def1$). Two alternative choices of non–tight definitions were tested: inverting at least two out of four variables (w_{s3}, F_{side}, ΔE, E_{ratio}) (here called $def2$) and inverting at least two out of the five variables (w_{s3}, F_{side}, ΔE, E_{ratio}, w_{tot}) (here called $def3$). The $Wjet$ ($Zjet$) background estimation results obtained using different definitions of non–tight regions are summarized in Table 12 (Table 13).

Corrections for signal contamination in control regions

As said in the previous section, in order to obtain a correct estimate of the W+jets background using the ABCD method, the leakage of signal events in the control regions needs to be taken into account. In these measurements, the leakage is estimated using the MC signal samples. However the MC may not be able to perfectly model data for both the isolation and shower shape variables which have been used to define the non–tight control region. A very conservative 10% systematic uncertainty is quoted to take into account the leakage of signal events into non–tight regions due to the large uncertainty associated to the low p_T photon ID efficiency, whereas a 2.5% systematic uncertainty is quoted for signal leakage into the non–isolated region.

Corrections for background correlations in control regions

The W+jets (Z+jets) background estimation is based on the assumption that for background events, the isolation energies $E_T^{iso(R<0.3)}$ for the reconstructed photons passing the analyses selection criteria (regions A and B) and the ones passing the non–tight control region criteria (regions C and D) are uncorrelated, *i.e.* their distribution is the same (albeit a normalization factor). Under this condition, we expect to have that $N_A^{bkg}/N_C^{bkg} \simeq N_B^{bkg}/N_D^{bkg}$. To test the impact of such an assumption on the W+jets (Z+jets) background estimation, a correction factor $R^{Wjet}(R^{Zjet})$ is introduced (as described in the previous section), defined as:

$W + jet$ background variations due to control region definition				
Non–tight (definition #)	Non–iso regions [GeV]	Type of study	Electron channel	Muon channel
		$15GeV < p_T(\gamma) < 20GeV$		
1	> 7	nominal	-	-
2	> 7	syst.	+14.7%	-14.0%
3	> 7	syst.	+0.47%	-23.2%
1	> 6	syst.	-0.02%	-7.3%
1	> 8	syst.	-13.2%	+3.5%
		$20GeV < p_T(\gamma) < 30GeV$		
1	> 7	nominal	-	-
2	> 7	syst.	-1.66%	-3.7%
3	> 7	syst.	-16.0%	-22.0%
1	> 6	syst.	-3.9%	-2.9%
1	> 8	syst.	-1.3%	+0.96%
		$30GeV < p_T(\gamma) < 40GeV$		
1	> 7	nominal	-	-
2	> 7	syst.	-6.0%	-2.6%
3	> 7	syst.	-47.0%	-10.4%
1	> 6	syst.	+6.2%	-4.6%
1	> 8	syst.	+10.1%	-0.86%
		$40GeV < p_T(\gamma) < 60GeV$		
1	> 7	nominal	-	-
2	> 7	syst.	-8.3%	-55.7%
3	> 7	syst.	+26.6%	-58.8%
1	> 6	syst.	13.4%	+2.6%
1	> 8	syst.	-7.1%	+4.2%
		$60GeV < p_T(\gamma) < 100GeV$		
1	> 7	nominal	-	-
2	> 7	syst.	-29%	>100%
3	> 7	syst.	-23.7%	>100%
1	> 6	syst.	-5.1%	-11.0%
1	> 8	syst.	-11.8%	-5.4%
		$100GeV < p_T(\gamma) < 1TeV$		
1	> 7	nominal	-	-
2	> 7	syst.	>100%	-27.5%
3	> 7	syst.	>100%	-37.3%
1	> 6	syst.	-3.4%	-5.7%
1	> 8	syst.	-3.13%	-7.4%

Table 12: Here the variations of the W+jets background counts associated to the ABCD regions definition in the different p_T bins in the signal region, for both electronic and muonic channel, are shown. The systematic uncertainty associated to the non–tight control region definition is estimated by using two alternative choices of non–tight photon ($def2$ and $def3$) as described in the text. Furthermore, the systematic uncertainty on the non–isolated control region is obtained varying the photon isolation requirement The maximum deviation from the nominal value are accounted for, in each p_T bin, as systematic uncertainties of the W+jets background estimate, as shown in Table **??**.

		$Z+jet$ background for $Z\gamma$					
(# of Var to invert)	Not-Iso regions (GeV)	Study	Electron	Electron	Muon	Muon	
		$p_T(\gamma) > 15GeV$					
			$N_{jet} >= 0$	$N_{jet} = 0$	$N_{jet} >= 0$	$N_{jet} = 0$	-
2	>7	nominal	-	-	-	-	
1	>7	syst.	+26.7%	+22.8%	+6.2%	+11.2%	
3	>7	syst.	-21.8%	-22.7%	-9.1%	-5.4%	
5	>6	syst.	+3.2%	+3.2%	+2.1%	-1.6%	
5	>8	syst.	-2.4%	-2.4%	+12.2%	+25.5%	
		$p_T(\gamma) > 60GeV$					
2	>7	nominal	-		-	-	
1	>7	syst.	+0.0%	+0.0%	-30.2%	-50.7%	
3	>7	syst.	-25.0%	-28.4%	-7.1%	-24.0%	
5	>6	syst.	0.0%	0.0%	+31.2%	+15.8%	
5	>8	syst.	+50%	+50%	+15.3%	+36.5%	

Table 13: The variation of the $Z+jet$ background estimations in $Z\gamma$ analysis by changing the definition of the background regions of the two dimensional sideband method used to estimate the purity fraction of isolated photon events in the signal region. Non-tight control regions can be reverted by requiring at least one ,two or three strips cuts to fail, non-isolated region can be defined by requiring photon isolaiton $> 6GeV$,$> 7GeV$ or $> 8GeV$. These deviation from nominal value are considered as one term of systematic in final systematic summary table **??** for $Zjet$ background.

$$R^{Wjet} = \frac{N_C^{Wjet} \cdot N_B^{Wjet}}{N_A^{Wjet} \cdot N_D^{Wjet}}$$

In order to study the impact of such a correlation on the data–driven method, R^{Wjet} is computed using high statistics MC samples of $W^{\pm} \to l^{\pm}\nu + \text{n jets}$ ($Z \to l^+l^- + \text{n jets}$) events generated using ALPGEN+JIMMY and with pile–up events superimposed. In these samples, the contributions from $W\gamma$ ($Z\gamma$) processes (both ISR and FSR) have been manually removed at the truth level, so that only background events are left. The R^{Wjets} ratio has thus been computed for both analyses, and in both muonic and electronic channels, for each photon p_T bin. Results are shown in Table 14, here p_T bins are defined inclusively in order to reduce the statistical uncertainty associated to the ratio.

p_T selection [GeV]	R^{Wjets} (electronic channel)	R^{Wjets} (muonic channel)	R^{Zjets} (electronic channel)	R^{Zjets} (muonic channel)
$15 < p_T$	1.4 ± 0.2	0.9 ± 0.1	$\pm$	$\pm$
$20 < p_T$	1.3 ± 0.2	0.9 ± 0.1	$\pm$	$\pm$
$30 < p_T$	1.2 ± 0.2	0.8 ± 0.1	$\pm$	$\pm$
$40 < p_T$	1.1 ± 0.2	1.0 ± 0.2	$\pm$	$\pm$
$60 < p_T$	0.6 ± 0.2	1.0 ± 0.2	$\pm$	$\pm$
$100 < p_T$	1.2 ± 0.6	0.8 ± 0.3	$\pm$	$\pm$

Table 14: R^{Wjets} and R^{Zjets} correction factors computed, according to the formula provided in the text, using ALPGEN+JIMMY background-only MC samples.

It is shown that, in almost every bin, the ratio is compatible with one within its statistical uncertainty, hence the assumption that the two variables (tightness and isolation of the photon) used to define the ABCD method control regions are uncorrelated is valid within uncertainties. A systematic uncertainty associated to this assumption on the number of W+jets (Z+jets) events found in the signal region is estimated by introducing in Equation 8 the ratios shown in Table 14.

In particular, systematic uncertainties on N_A^{wjet} due to correlation effect are evaluated in the following way:

$$\Delta N_A^{Wjet}(R^{wjet}) = N_A^{Wjet}(R^{wjet} = 1) - N_A^{Wjet}(R^{wjet} = R_{MC}^{wjet}).$$

Results are shown in Table 15.

W+jets background variations due to $R^{Wjets} = 1$ assumption		
p_T selection [GeV]	$W(\rightarrow e\nu)\gamma$	$W(\rightarrow \mu\nu)\gamma$
$15 < p_T < 20$	-37.3%	$+13.0\%$
$20 < p_T < 30$	-32.1%	$+21.7\%$
$30 < p_T < 40$	-22.8%	$+35.0\%$
$40 < p_T < 60$	-14.6%	$+5.2\%$
$60 < p_T < 100$	-88.2%	$+2.9\%$
$100 < p_T < 1000$	-15.1%	$+25.2\%$

Table 15: R^{Wjets} and R^{Zjets} correction factors computed, according to the formula provided in the text, using ALPGEN+JIMMY background-only MC samples.

Uncertainty due to Extrapolation

Besides the uncertainty of standard two dimensions sideband methods, addtional systematic uncertainties are needed to be estimated for signal yield in the certain phase space ($N_{jet} = 0$ and $p_{T\gamma} > 60GeV$ or $p_{T\gamma} > 100GeV$, detailed phase space definition is shown in table 22). The reason is that there are too few data events left in control regions for these phase space, and N_{jet} based extrapolation method described in section 3.3 is used as baseline method. To access the systematic uncertainties of extrapolation method, we compare the background estimation using N_{jet} based extrapolation method and $p_{T\gamma}$ based extrapolation method, and 2D sideband method in Table 16 for $W + jet$ background and in Table 17 for $Zjet$ background. The maximum difference between difference methods is quoted as systematic due to extrapolation for the certain phase space ($N_{jet} = 0$ and $p_{T\gamma} > 60GeV$, $p_{T\gamma} > 100GeV$ and $N_{jet} = 0$), in which the N_{jet} based extrapolation method is used as baseline method.

3.7 Systematics on $\gamma + jet$ Background Estimation

3.7.1 Systematics on $\gamma + jet$ Background Estimation in electron channel

Definition of not-isolated control region

In $W\gamma$ electron channel analysis, the electron candidates of the selected signal events are required to be isolated, with an electron isolation energy $E_T^{iso(R<0.3)} < 6$ GeV. The not-isolated control region (region C' and D' as defined in section 3.1) is chosen to have $E_T^{iso(R<0.3)} > 7$ GeV. The impact on the final purity measurement of this particular control region definition has been evaluated varying the boundary value to 6 GeV or 8 GeV. The effects of these variations are summarized table 18.

Channel	$W\,jet$ background $e\nu\gamma$	$\mu\nu\gamma$
	$p_T(\gamma) > 15GeV, N_{jet} = 0$	
N_{jet} based Extrapolation	277.9 ± 20.6	471.0 ± 46.5
2D sideband	241.8 ± 24.0	472.2 ± 45.4
	$p_T(\gamma) > 60GeV, N_{jet} = 0$	
N_{jet} based Extrapolation	6.4 ± 1.6	12.9 ± 3.2
$p_{T\gamma}$ Extrapolation	7.5 ± 0.8	10.0 ± 2.8
2D sideband	6.3 ± 2.4	10.6 ± 4.3
	$p_T(\gamma) > 100GeV, N_{jet} = 0$	
N_{jet} based Extrapolation	2.9 ± 0.9	$0.4^{+0.6}_{-0.4}$
$p_{T\gamma}$ Extrapolation	1.1 ± 0.5	$0.5^{+0.6}_{-0.5}$
2D sideband	1.5 ± 1.3	$0.6^{+0.7}_{-0.6}$

Table 16: Comparison of $W\,jet$ background data-driven background estimation using $p_{T\gamma}$ Extrapolation and N_{jet} based Extrapolation and 2D sideband methods. These discrepancy between method are considered as one term of systematic uncertainty in final systematic summary table **??** for $W\,jet$ background.

Channel	$e^+e^-\gamma$	$\mu^+\mu^-\gamma$
	$p_T(\gamma) > 15GeV, N_{jet} = 0$	
N_{jet} based Extrapolation	33.5 ± 5.9	38.6 ± 7.0
2D sideband	29.3 ± 6.4	38.6 ± 8.6
	$p_T(\gamma) > 60GeV, N_{jet} >= 0$	
$p_{T\gamma}$ Extrapolation	2.4 ± 0.5	2.6 ± 1.3
2D sideband	4.1 ± 2.0	4.6 ± 2.4
	$p_T(\gamma) > 60GeV, N_{jet} = 0$	
N_{jet} based Extrapolation	3.1 ± 2.0	3.4 ± 1.8
$p_{T\gamma}$ Extrapolation	1.4 ± 0.7	1.9 ± 1.0
2D sideband	1.6 ± 1.1	2.1 ± 1.5

Table 17: Comparison of $Z\,jet$ background data-driven background estimation using $p_{T\gamma}$ Extrapolation and N_{jet} based Extrapolation and 2D sideband methods. These discrepancy between method are considered as one term of systematic uncertainty in final systematic summary table **??** for $Z\,jet$ background.

$\gamma + jet$ background for $W\gamma$ analysis				
Low-MissingEt (GeV)	Not-Isolated regions(GeV)	Study	Electron channel $N_{jet} >= 0$	Electron channel $N_{jet} = 0$
$p_T(\gamma) > 15GeV$				
20	> 7	nominal	-	-
20	> 6	syst.	-2.33%	-17.32%
20	> 8	syst.	+14.14%	+18.89%
15	> 7	syst.	-4.73%	-0.611%
25	> 7	syst.	+1.16%	-2.64%
$p_T(\gamma) > 60GeV$				
20	> 7	nominal	-	-
20	> 6	syst.	+47.65%	-32.39%
20	> 8	syst.	+25.22%	+32.08%
15	> 7	syst.	-11.03%	-19.94%
25	> 7	syst.	+8.63%	+7.01%
$p_T(\gamma) > 100GeV$				
20	> 7	nominal	-	-
20	> 6	syst.	+77.04%	+212.7%
20	> 8	syst.	+24.03%	+74.25%
15	> 7	syst.	+18.40%	-2.55%
25	> 7	syst.	+20.08%	+14.88%

Table 18: The variation of the $\gamma + jet$ background estimation in $W\gamma$ analysis by changing the definition of the background regions of the two-dimensional sideband method. Low MET region can be defined as $MET < 20GeV$,$MET < 15GeV$ and $MET < 25GeV$, and non-isolated control regions can be defined by requiring electron isolation $>$ 7GeV, $> 6GeV$ or $> 8GeV$. These variations are considered as one term of systematics in Table 21.

Definition of low MET control region

In $W\gamma$ electron channel analysis, The low MET control region (regions B' and C' as defined in section 3.1) is chosen inverting MET cut used in $W\gamma$ selection cuts ($MET < 20GeV$). Two alternative choices of low-MET control regions were tested: $MET < 15GeV$ and $MET < 25GeV$. The $\gamma + jet$ background estimation results with different definition of non-tight regions are summarized in Table 18. The maximum difference in number of γjet background estimation using difference control regions is considered as systematics uncertainty as shown in Talbe 21.

Corrections for background correlations in control regions

The γjet background estimation is based on the assumption that for not-signal events, the lepton isolation energies $E_T^{iso(R<0.3)}$ for the reconstructed electrons passing our selection criteria (regions A and B') and the ones passing the low MET control region criteria (regions B' and D') are uncorrelated, *i.e.* their isolation distributions are the same (albeit a normalization factor). Under this condition, we can assume then $N_A^{\gamma jet}/N_{C'}^{\gamma jet} \simeq N_{B'}^{\gamma jet}/N_{D'}^{\gamma jet}$. To test the impact of such an assumption on the data-driven purity estimation, a corrector factor $R^{\gamma jet}$ can be introduced (as described in the previous section), defined as:

$$R^{\gamma jet} \cdot \frac{N_A^{\gamma jet}}{N_{C'}^{\gamma jet}} = \frac{N_{B'}^{\gamma jet}}{N_{D'}^{\gamma jet}} \Rightarrow R^{\gamma jet} = \frac{N_{C'}^{\gamma jet} \cdot N_{B'}^{\gamma jet}}{N_A^{\gamma jet} \cdot N_{D'}^{\gamma jet}}$$

$R^{\gamma jet}$ can be obtained from photon jet Monte Carlo simulation and from control samples in data, in which photon jet events dominanted. To obtain data driven $R^{\gamma jet}$ factor, photon jet control sample from data is selected by the following criteria:

- Triggered by EF_2g20_loose.
- At least one recontructed tight isolated photon in the event, as described in 2.6.
- Require exactly one recontructed electron in the event, which passes the "loose" electron selection criteria, but fails "medium" electron selection criteria.
- Require the $\Delta R(e;\gamma)$ between leading electron and leading photon in the event $\Delta R(e,\gamma) > 0.7$.

Benefitted from non-tight electron selection cut, the $W\gamma$ and Wjet contamination in this control region is rather small, Photon jet and $Z \to e^+e^-$ events dominate in this control region. According to Table 8, we divide this control sample into four regions, the number events in each regions,after subtracting expected "EW+TOP background" and $W\gamma$ and Wjet contamination from Monte Carlo simulation, is $N_{A''}$, $N_{B''}$, $N_{C''}$, $N_{D''}$, then

$$R^{\gamma jet}_{measured} = \frac{N_{B''} \times N_{C''}}{N_{A''} \times N_{D''}} \tag{11}$$

$R^{\gamma jet}$ obtained from photon jet MC and from data driven approach based on control sample collected by EF_2g20_loose is shown in Table 19 as a function of leading photon p_T threshold in the events.

Following Equation 8, $N_A^{\gamma jet}$ can be written as a function of $R^{\gamma jet}$ ($N_A^{\gamma jet}(R^{\gamma jet})$). The systematic of photon jet background estimation ($N_A^{\gamma jet}$) due to correlation effect is evaluated using Equation 12, where $R^{\gamma jet}_{measured} = 1.14$ for $W\gamma$ analysis with photon $p_{T\gamma} > 15GeV$, and $R^{\gamma jet}_{measured} = 0.91$ for $W\gamma$ analysis with photon $p_{T\gamma} > 60GeV$ and photon $p_{T\gamma} > 100GeV$ as shown in Table 19.

$$\Delta N_A^{\gamma jet}(R^{\gamma jet}) = |N_A^{\gamma jet}(R^{\gamma jet} = 1) - N_A^{W jet}(R^{\gamma jet} = R^{\gamma jet}_{measured})| \tag{12}$$

MC	$p_T > 15GeV$	$p_T > 25GeV$	$p_T > 30GeV$	$p_T > 40GeV$	$p_T > 50GeV$	$p_T > 60GeV$
MC $\gamma jet35$	0.84 ± 0.64	–	–	–	–	–
DataDriven	1.14 ± 0.04	1.09 ± 0.04	1.02 ± 0.04	0.96 ± 0.05	0.95 ± 0.06	0.91 ± 0.07

Table 19: Corelation factors $R^{\gamma jet}$, as a function of leading photon p_T threshold from 15GeV to 60GeV, in the events by using Pythia photon jet Monte Carlo simulation (we call it $R^{\gamma jet}_{MC}$) and data driven method based on control sample collected by EF_2g20_loose trigger as decribed in Equation 11. (We call it $R^{\gamma jet}_{measured}$.)

As addtional cross check to make sure the uncertainty on background correlation is under control, using events with one electron candidates triggered by EF_2g20_loose, the electron isolation shape after "EW+TOP background" subtraction, in different control regions is shown in Figure **??**. Three control regions are defined as follow:

- Region one is called 'Low MET + failed medium' (MET$< 25GeV$, require electron to pass loose but fail electron medium ID cuts).
- Region two is called ;high MET + failed medium' (MET$< 25GeV$, require electron to pass loose but fail electron medium ID cuts).
- Region three is 'Low MET + medium' (MET$> 25GeV$, require electron to pass medium ID cuts)

No significant discrepancy between electron isolation in different control regions is found, as shown in figure **??**. The discrepancy in isolation shape in different regions should be coverd by the uncertainty due to $R^{\gamma jet}_{measured}$ factor as shown in Table 19 and Table 21.

Uncertainty due to Extrapolation

Besides the uncertainty of standard two dimensions sideband methods, addtional systematic uncertainties are needed to be estimated for signal yield in the certain phase space ($N_{jet} = 0$ and $p_{T\gamma} > 60GeV$ or $p_{T\gamma} > 100GeV$, detailed phase space definition is shown in table 22). To access the systematic uncertainties of extrapolation method, we compare the number of photon jet background estimation using N_{jet} based extrapolation method and $p_{T\gamma}$ based extrapolation method, and 2D sideband method in Table 20 for $\gamma + jet$ background . The maximum difference between difference methods is quoted as systematic due to extrapolation for the certain phase space ($N_{jet} = 0$ and $p_{T\gamma} > 60GeV$, $p_{T\gamma} > 100GeV$ and $N_{jet} = 0$), in which the N_{jet} based extrapolation method is used as baseline method.

Source of systematics	$e\nu\gamma$
	$p_T(\gamma) > 15GeV, N_{jet} = 0$
N_{jet} based Extrapolation	151.4 ± 16.6
Direct 2D sideband	119.1 ± 18.6
	$p_T(\gamma) > 60GeV, N_{jet} = 0$
N_{jet} based Extrapolation	5.5 ± 2.2
$p_{T\gamma}$ Extrapolation	8.4 ± 2.7
Direct 2D sideband	7.6 ± 3.5
	$p_T(\gamma) > 100GeV, N_{jet} = 0$
N_{jet} based Extrapolation	1.0 ± 0.7
$p_{T\gamma}$ Extrapolation	1.6 ± 1.2
Direct 2D sideband	0.4 ± 0.4

Table 20: Comparison of γjet background data-driven background estimation using $p_{T\gamma}$ Extrapolation and N_{jet} based Extrapolation and 2D sideband methods. These variations between methods are considered as one term of systematics in Table 21.

Overall Uncertainty for $\gamma + jet$ background estimation in $W\gamma$ electron channel

By summing up all systematic mentioned above, a summary of all the data-driven purity uncertainties of $\gamma + jet$ background estimation are given in Table 21.

Source of systematics	$e\nu\gamma$	$e\nu\gamma$
	$p_T(\gamma) > 15GeV$	
	$N_{jet} >= 0$	$N_{jet} = 0$
Definition of non-isolation	14.1%	18.9%
Definition of low MET control region	4.7%	2.6%
Corrections for background correlations in control regions	14%	14%
Overall Uncertainty	20.4%	23.7%
	$p_T(\gamma) > 60GeV$	
	$N_{jet} = 0$	$N_{jet} >= 0$
Definition of not-isolated control region	47.7%	32.4%
Definition of not-tight control region	11.0%	19.9%
Corrections for background correlations in control regions	9%	9%
Extrapolation	-	52.7%
Overall Uncertainty	49.8%	65.6%
	$p_T(\gamma) > 100GeV$	
	$N_{jet} = 0$	$N_{jet} >= 0$
Definition of not-isolated control region	77.0%	212.7%
Definition of not-tight control region	20.0%	14.9%
Corrections for background correlations in control regions	9%	9%
Extrapolation		60.0%
Overall Uncertainty	80.0%	221.7%

Table 21: Summary of the impact of each term of systematic uncertainties and overall uncertainties on γjet background estimation for $W\gamma$ analysis in electron channel. The input table are Table 19 and Table 18 and 20.

4 introduction to unfolding

4.1 Unfolding the Photon Transverse Energy Distribution

The unfolding of the photon transverse energy (E_T) distribution for $W\gamma$ ($Z\gamma$) is to determine the true number of $W\gamma$ ($Z\gamma$) events in each photon E_T bin, based on the number of observed events passing the analysis cuts, by taking into account the measurement uncertainties due to statistical fluctuation in the finite measured sample.

The unfolding is performed using the electroweak group common unfolding tool [8] (by M. Schott *et. al.*), which is based on the RooUnfold package [9]. The photon E_T spectrum is unfolded with two methods. A simple “bin-by-bin” method and a more sophisticated “bayesian” method which accounts for migration between bins.

Figure XXX (XXX) shows the “purity” as a function of the true photon E_T for $W\gamma$ ($Z\gamma$) events. The purity is defined as the fraction of the true events in the photon E_T bin that is being reconstructed in the same photon E_T bin.

The unfolded photon E_T distributions for $W\gamma$ production are shown in Figure XXX, and the unfolded photon E_T distribution for $Z\gamma$ production is shown in Figure XXX. The unfolded distributions using “bin-by-bin” method is compared to the unfolded distributions based on the “bayesian” method.

4.2 unfolding for radiation zero

5 Cross section measurements

For the $W\gamma$ and $Z\gamma$ analysis, the cross sections are measured in the fiducial phase space as defined in Table 22. These measurments are then extrapolated to an extended fiducial phase space and the extended cross sections are reported at particle level. The cross section measurements are performed for three photon transverse momentum thresholds (low/medium/high) in the $W\gamma$ analysis, and for two photon transverse momentum thresholds (low/medium) in the $Z\gamma$ analysis. The cross sections are also measured in the inclusive and exclusive jet multiplicity configurations. Therefore there are $3\times3\times2$ fiducial cross section measurements for $W\gamma$ analysis, and 3×2 fiducial cross section measurements for $Z\gamma$ analysis.

5.1 Fiducial phase space defintion

According to the $W\gamma$($Z\gamma$) selections criteria defined as Section 2.6, Fiducial phase space for cross section measurement is defined in Table 22.

In order to extract more information from data, six fiducial phase space, with different photon p_T threshold and with different N_{jets} requirement, is defined for $W\gamma$ measurement and four fiducial phase space is defined for $Z\gamma$ measurement, the naming convention of these different fiducial phase space is defined in Table 23.

Particle-level jets in Table 23 are defined as jets reconstructed in simulated events by applying the anti-kt jet reconstruction algorithm[6] with a radius parameter R = 0.4 to all final state particles.

- low pT inclusive phase space :
  - It is defined for baseline measurement.
  - Measurement in this phase space can be compared with the result from other experiment.
- low p_T zero jet exclusive phase space :
  - It is defined for baseline measurement.

Fiducial Cross Section				
Cuts	$e\nu\gamma$	$\mu\nu\gamma$	$e^+e^-\gamma$	$\mu^+\mu^-\gamma$
Lepton $E_t(p_T)$	$E_T^e > 25$ GeV $p_T^\nu > 25$ GeV	$p_T^\mu > 25$ GeV $p_T^\nu > 25$ GeV	$E_T^e > 25$ GeV	$p_T^\mu > 25$ GeV
Lepton η	$\lvert\eta_e\rvert < 2.47$ excluding $1.37 < \lvert\eta_e\rvert < 1.52$	$\lvert\eta_\mu\rvert < 2.4$	$\lvert\eta_e\rvert < 2.47$ excluding $1.37 < \lvert\eta_e\rvert < 1.52$	$\lvert\eta_\mu\rvert < 2.4$
Boson mass	$m_T > 40$ GeV	$m_T > 40$ GeV	$m_{ee} > 40$ GeV	$m_{\mu\mu} > 40$ GeV
Jet	AntiKT4 truth particle level jet $N_{jet} = 0$ (or $N_{jet} >= 0$) $p_T^{jet} > 30GeV$, $\lvert\eta_T^{jet}\rvert < 4.4$ $\Delta R(lepton; jet) > 0.6$ and $\Delta R(\gamma; jet) > 0.6$			
Photon	$E_T^\gamma > 15$ GeV or ($E_T^\gamma > 60$ GeV) or ($E_T^\gamma > 100$ GeV)		$E_T^\gamma > 15$ GeV or ($E_T^\gamma > 60$ GeV)	
	$\lvert\eta_\gamma\rvert < 2.37$ (excluding $1.37 < \lvert\eta_\gamma\rvert < 1.52$) $\Delta R(l, \gamma) > 0.7$ photon isolation fraction $\varepsilon_h^p < 0.5$			
$\lvert m(l, \gamma) - m(Z) \rvert$	> 10 GeV			
Extended fiducial Cross Section				
Cuts	$e\nu\gamma$	$\mu\nu\gamma$	$e^+e^-\gamma$	$\mu^+\mu^-\gamma$
Lepton $E_t(p_T)$	$E_T^e > 25$ GeV $p_T^\nu > 25$ GeV	$p_T^\mu > 25$ GeV $p_T^\nu > 25$ GeV	$E_T^e > 25$ GeV	$p_T^\mu > 25$ GeV
Lepton η	$\lvert\eta_e\rvert < 2.47$	$\lvert\eta_\mu\rvert < 2.47$	$\lvert\eta_e\rvert < 2.47$	$\lvert\eta_\mu\rvert < 2.47$
Jet	AntiKT4 truth particle level jet $N_{jet} = 0$ (or $N_{jet} >= 0$) $p_T^{jet} > 30GeV$, $\lvert\eta_T^{jet}\rvert < 4.4$ $\Delta R(lepton; jet) > 0.6$ and $\Delta R(\gamma; jet) > 0.6$			
	$E_T^\gamma > 15$ GeV or ($E_T^\gamma > 60$ GeV) or ($E_T^\gamma > 100$ GeV)		$E_T^\gamma > 15$ GeV or ($E_T^\gamma > 60$ GeV)	
Boson mass			$m_{ee} > 40$ GeV	$m_{\mu\mu} > 40$ GeV
Photon	$\lvert\eta_\gamma\rvert < 2.37$ $\Delta R(l, \gamma) > 0.7$ photon isolation fraction $\varepsilon_h^p < 0.5$			

Table 22: Definition of the fiducial regions where the measurements are performed and the extended region (common to all measurements) where the total cross sections are evaluated, where ε_h^p is defined at particle level as the ratio between sum of the energies carried by final state particles in the cone $\Delta R < 0.4$ around the photon and the energy carried by the photon.

Phase space name	N_{jet}	$p_{T\gamma}$ threshold	others cuts
low pT inclusive	$>= 0$	$> 15GeV$	cuts for $l\nu\gamma$ and $l^+l^-\gamma$ channel in Table 22
low pT exclusive 0 jet	$= 0$	$> 15GeV$	cuts for $l\nu\gamma$ and $l^+l^-\gamma$ channel in Table 22
medium pT inclusive	$>= 0$	$> 60GeV$	cuts for $l\nu\gamma$ and $l^+l^-\gamma$ channel in Table 22
medium pT exclusive 0 jet	$= 0$	$> 60GeV$	cuts for $l\nu\gamma$ and $l^+l^-\gamma$ channel in Table 22
high pT inclusive	$>= 0$	$> 100GeV$	cuts for $l\nu\gamma$ channel in Table 22
high pT exclusive 0 jet	$= 0$	$> 100GeV$	cuts for $l\nu\gamma$ channel in Table 22

Table 23: The name and definition of six fiducial phase space, with different photon p_T threshold and with different N_{jets} requirement, for $W\gamma$ measurement and four fiducial phase space is defined for $Z\gamma$ measurement.

  - Measurement in this phase space can be compared with standard model NLO prediction from MCFM generator.

- medium p_T inclusive phase space :
  - It is defined for precise measurement in this phase space for $W\gamma$ channel.
- medium p_T zero jet exclusive phase space :
  - It is defined for precise measurement in this phase space for $W\gamma$ channel.
  - The measurement in this phase space for $Z\gamma$ channel is treated as input to extract limits on anomalous triple gauge coupling(ATGC).
  - Measurement in this phase space can be compared with standard model NLO prediction from MCFM generator.
- high p_T zero jet exclusive phase space :
  - The measurement in this phase space for $W\gamma$ channel is treated as input to extract limits on anomalous triple gauge coupling(ATGC).
  - Measurement in this phase space can be compared with standard model NLO prediction from MCFM generator.

5.2 Extended Fiducial cross sections for $W\gamma$

In $W\gamma$ and $Z\gamma$ analysis ($pp \to l\nu\gamma(ll\gamma)$, where $l = e, \mu$), only electron and muon decay channels are considered as signal, the tau decay channels are considered as background. The measurements of the cross sections in the fiducial and extended fiducial region are defined as

$$\sigma^{fid}_{pp\to l\nu\gamma(ll\gamma)} = \frac{N^{sig}_{W\gamma(Z\gamma)}}{C_{W\gamma(Z\gamma)} \cdot L_{W\gamma(Z\gamma)}} \tag{13}$$

$$\sigma^{extfid}_{pp\to l\nu\gamma(ll\gamma)} = \frac{\sigma^{fid}_{pp\to l\nu\gamma(ll\gamma)}}{A_{W\gamma(Z\gamma)}} \tag{14}$$

where

- $N^{sig}_{W\gamma}$ and $N^{sig}_{Z\gamma}$ denote the numbers of background-subtracted signal events passing the selection criteria of the analyses in the $W\gamma$ and $Z\gamma$ channels.
- $C_{W\gamma}$ and $C_{Z\gamma}$ denote the ratios between the total number of generated events which pass the fiducial selection requirements after reconstruction and the total number of generated events which pass the fiducial selection at the particle level.
- $L_{W\gamma}$ and $L_{Z\gamma}$ denote the integrated luminosities for the channels of interest.
- $A_{W\gamma}$ ($A_{Z\gamma}$) denote the acceptances, defined as the fraction of events in $W(Z)+\gamma$ Monte Carlo sample, which is within the particle level phase space of extended fiducial cross sections, satisfying the geometrical and kinematic constraints of fiducial cross section at particle level as shown in Table 22.

By definition, Extended fiducial cross sections measurement focus on the kinematics region where can be well measured. Due to acceptance difference between electron channel and muon channel, a small extrapolations (mainly do extrapolations to account for acceptance loss due to EM calorimeter crack region) is needed to correct the fiducial cross sections measurement to extended fiducial phase space , which is common for both electron and muon channel. The N^{sig} for both $W\gamma$ and $Z\gamma$ processes is given is Table 9 and Table 11.

5.2.1 Correction factor $C_{W\gamma}$ and $C_{Z\gamma}$

The central values of the correction factors $C_{W\gamma}$ and $C_{Z\gamma}$ are computed using $W/Z+\gamma$ signal Monte-Carlo samples with data driven scale factor to correct for discrepancy in lepton and photon selection efficiency between data and Monte Carlo.

$C_{W\gamma(Z\gamma)}$ can be decomposed as:

$$C_{W\gamma(Z\gamma)} = \frac{N^{sel}_{reco}}{N^{acc}_{gen}} = \frac{N^{sel}_{reco}}{N^{acc}_{reco}} \cdot \frac{N^{acc}_{reco}}{N^{acc}_{gen}} \tag{15}$$

where the labels "reco" and "gen" refer respectively to selections applied to fully simulated and reconstructed events and to generated events only. The first term $\frac{N^{sel}_{reco}}{N^{acc}_{reco}}$ mainly includes all trigger,photon and lepton selection efficiency. A more detail of the break down of $C_{W\gamma(Z\gamma)}$ can be written as :

$$C_{W\gamma} = \varepsilon^{W\gamma}_{event} \cdot \varepsilon^{W\gamma}_{lep} \cdot \varepsilon^{W\gamma}_{trig} \cdot \varepsilon^{\mathrm{ID}}_{\gamma} \cdot \varepsilon^{\mathrm{iso}}_{\gamma} \cdot \alpha^{W\gamma}_{reco} \tag{16}$$

$$C_{Z\gamma} = \varepsilon^{Z\gamma}_{event} \cdot (\varepsilon^{Z\gamma}_{lep})^2 \cdot \varepsilon^{Z\gamma}_{trig} \cdot \varepsilon^{\mathrm{ID}}_{\gamma} \cdot \varepsilon^{\mathrm{iso}}_{\gamma} \cdot \alpha^{Z\gamma}_{reco} \tag{17}$$

where

	$W\gamma \to e\nu\gamma$					
	$p_T(\gamma) > 15GeV$		$p_T(\gamma) > 60GeV$		$p_T(\gamma) > 100GeV$	
	$N_{jet} = 0$	$N_{jet} >= 0$	$N_{jet} = 0$	$N_{jet} >= 0$	$N_{jet} = 0$	$N_{jet} >= 0$
ε_{event}	99.2%	98.9%	98.3%	96.4%	98.0%	95.9%
ε_{lep}	73.9%	74.9%	78.1%	78.5%	77.4%	77.6%
ε_{lep}^{iso}	98.8%	98.4%	97.3%	97.5%	95.9%	97.0%
$\varepsilon_{trig}^{event}$	98.2%	98.0%	98.4%	98.2%	98.6%	98.3%
$\varepsilon_{\gamma}^{ID}$	71.0%	67.0%	91.9%	86.0%	94.0%	88.7%
$\varepsilon_{\gamma}^{iso}$	96.6%	96.6%	91.1%	92.3%	88.3%	90.9%
α_{reco}	82.7%	98.8%	92.5%	103.8%	83.7%	100.5%
$C_{W\gamma}$	40.2%	45.3%	57.4%	59.8%	51.7%	57.6%
	$W\gamma \to \mu\nu\gamma$					
	$p_T(\gamma) > 15GeV$		$p_T(\gamma) > 60GeV$		$p_T(\gamma) > 100GeV$	
	$N_{jet} = 0$	$N_{jet} >= 0$	$N_{jet} = 0$	$N_{jet} >= 0$	$N_{jet} = 0$	$N_{jet} >= 0$
ε_{event}	100%	100%	100%	100%	100%	100%
ε_{lep}	92.1%	88.4%	93.3%	86.1%	92.5%	84.4%
$\varepsilon_{trig}^{event}$	83.2%	83.2%	83.0%	83.0%	84.5%	83.7%
$\varepsilon_{\gamma}^{ID}$	69.1%	68.8%	89.5%	89.7%	91.3%	91.5%
$\varepsilon_{\gamma}^{iso}$	99.2%	99.0%	94.2%	95.6%	91.9%	93.9%
α_{reco}	86.1%	100.2%	99.9%	106.0%	103.0%	102.8%
$C_{W\gamma}$	45.3%	51.1%	65.3%	65.0%	67.5%	62.4%

Table 24: Efficiency factors per lepton and α_{reco} as well as their relative uncertainties which enter the calculation of the correction factors $C_{W\gamma}$ for both lepton channels. The trigger efficiencies were measured from data. The other efficiencies and their uncertainties were determined from Monte-Carlo simulation and have been validated with data, as described in the text. A detailed summary of the various contributions entering the uncertainty on $C_{w\gamma}$ is given in Table. 26 and Table. 27

- ε_{event}: event selection efficiencies, (including efficiency of primary vertex requirement).
- ε_{γ}: photon selection efficiency, including photon identification efficiency($\varepsilon_{\gamma}^{\mathrm{ID}}$), and photon isolation efficiency $\varepsilon_{\gamma}^{\mathrm{iso}}$.
- ε_{lep}: lepton selection efficiency, including lepton identification efficiency($\varepsilon_{e}^{\mathrm{ID}}$ or $\varepsilon_{\mu}^{\mathrm{ID}}$), and lepton isolation efficiency($\varepsilon_{\mu}^{\mathrm{iso}}$ or $\varepsilon_{e}^{\mathrm{iso}}$). For the $Z\gamma$ case, the efficiencies of the leading and sub-leading lepton (and the associated uncertainty) have been averaged for convenience ($\varepsilon_{lep} = \sqrt{\varepsilon_{leading}\varepsilon_{sub-leading}}$).
- ε_{trig} : efficiency to trigger the event .
- α_{reco}: $\alpha_{reco} = \frac{N_{reco}^{acc}}{N_{gen}^{acc}}$, account for the basic reconstruction efficiency (including photon reconstruction efficiency ($\varepsilon_{\gamma}^{\mathrm{reco}}$) and lepton reconstruction efficiency ($\varepsilon_{e}^{\mathrm{reco}}$ or $\varepsilon_{\mu}^{\mathrm{reco}}$), and all detector smearing effect(including bin migration effects).

The correction factors $C_{W\gamma}$ ($C_{Z\gamma}$) of both electron and muon channels are given in Table 24 (Table 25).

There are many effects contributing to the uncertainty on $C_{W\gamma}$ and $C_{Z\gamma}$. These effects are listed here :

- Energy scale and resolution: EM Energy scale factor from insitu $Z \to ee$ data driven calibration has been applied to correct for cluster energy of electron and photon candidate in data,as mentioned

	$Z\gamma \rightarrow ee\gamma$			
	$p_T(\gamma) > 15GeV$		$p_T(\gamma) > 60GeV$	
	$N_{jet} = 0$	$N_{jet} >= 0$	$N_{jet} = 0$	$N_{jet} >= 0$
ε_{event}	99.9%	99.9%	99.9%	99.9%
ε_{lep}	93.5%	93.5%	94.9%	94.7%
$\varepsilon_{trig}^{event}$	100%	100%	100%	100%
$\varepsilon_{\gamma}^{ID}$	69.9%	66.7%	92.4%	88.3%
$\varepsilon_{\gamma}^{iso}$	98.9%	98.4%	96.5%	96.1%
α_{reco}	65.9%	74.1%	74.5%	80.1%
$C_{Z\gamma}$	39.8%	42.1%	59.0%	60.0%
	$Z\gamma \rightarrow \mu\mu\gamma$			
	$p_T(\gamma) > 15GeV$		$p_T(\gamma) > 60GeV$	
	$N_{jet} = 0$	$N_{jet} >= 0$	$N_{jet} = 0$	$N_{jet} >= 0$
ε_{event}	100.0%	100.0%	100.0%	100.0%
ε_{lep}	90.9%	90.7%	90.5%	89.8%
$\varepsilon_{trig}^{event}$	96.5%	96.6%	97.0%	97.2%
$\varepsilon_{\gamma}^{ID}$	67.2%	67.1%	90.5%	89.9%
$\varepsilon_{\gamma}^{iso}$	99.5%	99.2%	97.9%	97.5%
α_{reco}	86.2%	91.7%	91.0%	92.2%
$C_{Z\gamma}$	45.9%	48.5%	64.1%	64.5%

Table 25: Efficiency factors and α_{reco} as well as their relative uncertainties which enter the calculation of the correction factors $C_{Z\gamma}$ for both lepton channels. The trigger efficiencies were measured from data. The other efficiencies and their uncertainties were determined from Monte-Carlo simulation and have been validated with data, as described in the text. A detailed summary of the various contributions entering the uncertainty on $C_{w\gamma}$ is given in Table. 26 and Table. 27

in section 2.3.It was found that EM energy resolution in Monte Carlo is better than resolution in data. A smearing recommended by Egamma group have been applied to all signal and background Monte Carlo in order to reproduce energy resolution in data [25]. The impact of EM scale uncertainty on $C_{W\gamma}(C_{Z\gamma})$ is estimated by variating the EM scale of $W\gamma(Z\gamma)$ Monte Carlo is shown in Table 26. .

- Uncertainty due to Jet scale and resolution include main contributions: Jet energy scale uncertainty is evaluated by Jet/MET group from Monte Carlo simulation and validated by data using $\gamma + jet$ events and multi-jets events. The detailed information for jet energy uncertainty is documented in Ref [26]. The detailed information for jet energy resolution uncertainty is documented in Ref [27]. By variating jet energy scale and resolution in signal Monte Carlo samples, the maxinum variation of $C_W\gamma$ ($C_Z\gamma$) from nominal value for exclusive 0 jet measurement is considered as systemstics errors.

- Uncertainty due to E_T^{miss} scale and resolution include main contributions: the topological cluster energy scale, imperfect modeling of the overall E_T^{miss} response (low energy hadrons) and resolution, modeling of the underlying event and pile-up effects.

Table 26 is the summary of the different terms contributing to the uncertainty on $C_{W\gamma}$ and $C_{Z\gamma}$ for electron final states. According to Table 26, the systematic uncertainty of $C_{W\gamma}(C_{Z\gamma})$ mostly comes from photon identification efficiency, Jet energy scale uncertainty and EM scale uncertainty.

The terms that contribute to the uncertainty on $C_{W\gamma}$ and $C_{Z\gamma}$ for muon final states are listed in Table 27.

5.2.2 Acceptance factor ($A_{W\gamma}$ and $A_{Z\gamma}$)

The acceptance $A_{W\gamma}$ ($A_{Z\gamma}$) is used to extrapolate the measurement in fiducial phase space to extended fiducial phase space (mainly do extrapolations to account for acceptance loss due to EM calorimeter crack region), as defined in Table 22.

$$A_{W(Z)\gamma} = \frac{N_{fiducial}}{N_{extented\_fidual}} \tag{18}$$

The precision definition of $A_{W(Z)\gamma}$ is shown in equation 18, where $N_{fiducial}$ is number of events in fiducial region in a signal MC simulation sample and $N_{extented\_fidual}$ is number of events in extented fiducial phase space in the same signal MC sample, the fiducial and extented fiducial phase space are defined in table 22.

The systematic uncertainties on the acceptances are dominated by the limited knowledge of the proton PDFs and the renormalisation and factorisation scale factor uncertainties in signal MC simulation:

- PDF uncertainty:
  - Uncetainty due to discrepancy between different PDF central sets: The signal MC simulations for $W\gamma$ and $Z\gamma$ are generated with CTEQ6L1 parton distribution function.
    - By using PDF reweighting technique, signal MC samples are reweighted with MSTW 2008 NLO 95% CL PDF central set.
    - The uncetainty on signal acceptances due to discrepancy between different PDF central sets is estimated by comparing the acceptances difference between these two PDF central sets.
  - The uncertainty within MSTW 2008 NLO 95% CL PDF set:
    - The signal MC are also reweighted with 40 MSTW 2008 NLO 95% CL error sets.

Composition	$\delta C_{W\gamma}/C_{W\gamma}$	$\delta C_{Z\gamma}/C_{Z\gamma}$	$\delta C_{W\gamma}/C_{W\gamma}$	$\delta C_{Z\gamma}/C_{Z\gamma}$	$\delta C_{W\gamma}/C_{W\gamma}$
$p_T(\gamma)$	$> 15GeV$		$> 60GeV$		$> 100GeV$
N_{jet}			$N_{jet} = 0$		
Trigger efficiency	0.5%	0.02%	0.5%	0.02%	0.5%
electron recontruction efficiency	0.7%	1.0%	0.7%	1.0%	0.7%
electron identification efficiency	1.6%	2.2%	1.5%	2.2%	1.5%
electron isolation efficiency	1%	1%	1%	1%	1%
photon identification efficiency	10.5%	10.5%	4.3%	4.3%	4.3%
photon isolation efficiency	1.5%	1.5%	2.0%	2.0%	2.5%
EM scale and resolution	2.5%	2.0%	2.3%	2.2%	2.5%
Jet energy scale	5.0%	3.2%	4.8%	4.5%	4.8%
Jet energy resolution	0.5%	0.2%	1%	1%	1%
E_T^{miss} scale and resolution	2.7%		2.6%		3.2%
Total uncertainty	12.5%	11.6%	7.9%	7.4%	8.3%
N_{jet}			$N_{jet} >= 0$		
Trigger efficiency	0.5%	0.02%	0.5%	0.02%	0.5%
electron recontruction efficiency	0.7%	1.0%	0.7%	1.0%	0.7%
electron identification efficiency	1.6%	2.2%	1.5%	2.2%	1.5%
electron isolation efficiency	1%	1%	1%	1%	1%
photon identification efficiency	11.0%	11.0%	4.5%	4.5%	4.5%
photon isolation efficiency	1.5%	1.5%	2.0%	2.0%	2.5%
EM scale and resolution	2.5%	2.0%	2.3%	2.2%	2.2%
E_T^{miss} scale and resolution	2.5%		2.0%		2.4%
Total uncertainty	11.9%	11.6%	6.1%	6.0%	6.4%

Table 26: Summary of the different terms contributing to the uncertainty on $C_{W\gamma}$ and $C_{Z\gamma}$ for electron final states.

Composition	$\delta C_{W\gamma}/C_{W\gamma}$	$\delta C_{Z\gamma}/C_{Z\gamma}$	$\delta C_{W\gamma}/C_{W\gamma}$	$\delta C_{Z\gamma}/C_{Z\gamma}$	$\delta C_{W\gamma}/C_{W\gamma}$
$p_T(\gamma)$	$> 15GeV$		$> 60GeV$		$> 100GeV$
N_{jet}			$N_{jet} = 0$		
Trigger efficiency	1%	1%	1%	1%	1%
muon ID efficiency	0.7%	1.4%	0.7%	1.4%	0.7%
muon isolation efficiency			negligible		
Momentum scale and resolution	0.7%	0.2%	1%	0.3%	1%
EM Energy scale and resolution	1.4%	1.3%	1.7%	1.5%	1.5%
photon identification efficiency	10.5%	10.5%	4.3%	4.3%	4.3%
photon isolation efficiency	1.5%	1.5%	2.0%	2.0%	2.5%
Jet energy scale	5.1%	3.6%	6.8%	3.8%	6.8%
Jet energy resolution	0.4%	0.2%	1%	1%	1%
E_T^{miss} scale and resolution	3.0%	-	2.9%	-	3.0%
Total uncertainty	12.3%	11.4%	9.1%	6.6%	9.3%
N_{jet}			$N_{jet} >= 0$		
Trigger efficiency	1%	1%	1%	1%	1%
muon identification efficiency	0.7%	1.4%	0.7%	1.4%	0.7%
muon isolation efficiency			negligible		
Momentum scale and resolution	0.4%	0.1%	1%	0.3%	1%
EM Energy scale and resolution	1.1%	1.2%	1.3%	1.3%	1.5%
photon identification efficiency	11.0%	11.0%	4.5%	4.5%	4.5%
photon isolation efficiency	1.5%	1.5%	2.0%	2.0%	2.5%
E_T^{miss} scale and resolution	2.7%	-	2.3%	-	2.1%
Total uncertainty	11.5%	11.3%	5.8%	5.4%	6.0%

Table 27: Summary of the different terms contributing to the uncertainty on $C_{W\gamma}$ and $C_{Z\gamma}$ for muon final states. The decomposition has been made such that correlations between the various contributions are negligible.

        * The difference in signal acceptance between central sets and error sets are quoted as systematic errors.

- Renormalisation and factorisation scale uncertainty:
  - this uncertainty is estimated by varying the renormalisation and factorisation scale by factors of two around the nominal scales.

The list of systematic uncertainty for $A_{W\gamma}$ and $A_{Z\gamma}$ is summarized in Table 28 and Table 29.

Source of systematics	$e\nu\gamma$	$e\nu\gamma$	$\mu\nu\gamma$	$\mu\nu\gamma$
	$p_T(\gamma) > 15GeV$			
	$N_{jet} >= 0$	$N_{jet} = 0$	$N_{jet} >= 0$	$N_{jet} = 0$
Discrepancy between different PDF central sets	0.1%	0.1%	0.1%	0.1%
Discrepancy within MSTW 2008 NLO 95% CL PDF set	0.1%	0.1%	0.1%	0.1%
renormalisation and factorisation scale uncertainty	0.6%	1.0%	0.6%	0.3%
Overall Uncertainty	0.6%	1.0%	0.6%	0.3%
	$p_T(\gamma) > 60GeV$			
	$N_{jet} >= 0$	$N_{jet} = 0$	$N_{jet} >= 0$	$N_{jet} = 0$
Discrepancy between different PDF central sets	0.7%	0.9%	0.6%	0.6%
Discrepancy within MSTW 2008 NLO 95% CL PDF set	0.1%	0.1%	0.1%	0.1%
renormalisation and factorisation scale uncertainty	1.6%	2.1%	2.4%	2.2%
Overall Uncertainty	1.7%	2.3%	2.5%	2.3%
	$p_T(\gamma) > 100GeV$			
	$N_{jet} >= 0$	$N_{jet} = 0$	$N_{jet} >= 0$	$N_{jet} = 0$
Discrepancy between different PDF central sets	0.6%	1.0%	0.7%	1.1%
Discrepancy within MSTW 2008 NLO 95% CL PDF set	0.2%	0.2%	0.2%	0.3%
renormalisation and factorisation scale uncertainty	2.5%	2.5%	3.4%	2.2%
Overall Uncertainty	2.6%	2.7%	3.5%	2.5%

Table 28: Summary of the list systematic uncertainties and overall uncertainties on acceptance ($A_{W\gamma}$ estimation for $W\gamma$ analysis)

5.3 Results of extended fiducial crosssection measurments

Assuming lepton universality for the W and Z-boson decays,the measured cross-sections in both channels can be combined to decrease the statistical uncertainty. The cross-section for the two different channels are combined by an weighted average of the individual cross-sections. The combination of electron and muon channels in extended fiducial cross section measurement is performed following the method described in Ref [28]. In order to combine two channels , we need a weight for each channel. The weight for individual channels (w_e for electron channel , w_μ for muon channel) is derived by the uncorrelated uncertainties (σ_l^{unc}, where $l = e, \mu$) , including statistical, and uncorrelated systematic uncertainties, as shown in Equation 20. The correlated errors and uncorrelated errors we considered for both electron and muon channels is shown in Table 33.

$$\sigma(combined) = \frac{1}{w_e + w_\mu}(w_e \times \sigma(e) + w_\mu \times \sigma(\mu)) \tag{19}$$

$$w_l = \frac{1}{\sigma_l^{unc2}} \tag{20}$$

Source of systematics	$l^+l^-\gamma$	$l^+l^-\gamma$
	$p_T(\gamma) > 15GeV$	
	$N_{jet} >= 0$	$N_{jet} = 0$
Discrepancy between different PDF central sets	0.3%	0.3%
Discrepancy within MSTW 2008 NLO 95% CL PDF set	0.1%	0.1%
renormalisation and factorisation scale uncertainty	1.7%	1.7%
Overall Uncertainty	1.7%	1.7%
	$p_T(\gamma) > 60GeV$	
	$N_{jet} >= 0$	$N_{jet} = 0$
Discrepancy between different PDF central sets	0.4%	0.6%
Discrepancy within MSTW 2008 NLO 95% CL PDF set	0.1%	0.1%
renormalisation and factorisation scale uncertainty	0.5%	0.7%
Overall Uncertainty	0.6%	0.9%

Table 29: Summary of the list systematic uncertainties and overall uncertainties on acceptance ($A_{Z\gamma}$ estimation for $Z\gamma$ analysis)

	$W\gamma \to e\nu\gamma$				$W\gamma \to \mu\nu\gamma$			
	$p_T(\gamma) > 15GeV, N_{jet} = 0$							
	value	stat	syst	lumi	value	stat	syst	lumi
$N^{sig}_{W\gamma}$	1074.1	44.8	71.6	-	1362	58.8	122.7	-
$L_{W\gamma}[pb^{-1}]$	1024	-	-	37.9	1024	-	-	37.9
$C_{W\gamma}$	40.2%	0.4%	4.9%	-	45.3%	0.4%	5.4%	-
$A_{W\gamma}$	76.2%	0.3%	0.5%	-	90.8%	0.3%	0.5%	-
	$p_T(\gamma) > 60GeV, N_{jet} = 0$							
	value	stat	syst	lumi	value	stat	syst	lumi
$N^{sig}_{W\gamma}$	54.6	7.9	5.0	-	74.3	9.2	6.8	-
$L_{W\gamma}[pb^{-1}]$	1024	-	-	37.9	1024	-	-	37.9
$C_{W\gamma}$	57.4%	0.3%	4.5%	-	65.3%	0.3%	5.7%	-
$A_{W\gamma}$	68.5%	0.2%	1.7%	-	76.4%	0.2%	1.9%	-
	$p_T(\gamma) > 100GeV, N_{jet} = 0$							
	value	stat	syst	lumi	value	stat	syst	lumi
$N^{sig}_{W\gamma}$	14.4	4.0	3.0	-	12.8	3.6	1.2	-
$L_{W\gamma}[pb^{-1}]$	1024	-	-	37.9	1024	-	-	37.9
$C_{W\gamma}$	51.7%	0.6%	4.3%	-	67.5%	0.7%	5.9%	-
$A_{W\gamma}$	67.2%	0.5%	1.8%	-	70.8%	0.5%	1.7%	-

Table 30: Summary of input quantities for the calculation of the $W\gamma$ production cross sections. For each channel, the observed numbers of signal events after background subtraction, the correction factors , the acceptance factors $A_{W\gamma}$ and the integrated luminosities are given, with their statistical, systematic, and luminosity uncertainties.

	$W\gamma \rightarrow e\nu\gamma$				$W\gamma \rightarrow \mu\nu\gamma$				
$p_T(\gamma) > 15GeV, N_{jet} >= 0$									
	value	stat	syst	lumi	value	stat	syst	lumi	
$N^{sig}_{W\gamma}$	1464.5	56.8	118.4	-	2197.6	69.0	158.6	-	
$L_{W\gamma}[pb^{-1}]$	1024	-	-	37.9	1024	-	-	37.9	
$C_{W\gamma}$	45.3%	0.3%	5.3%	-	51.1%	0.3%	5.7%	-	
$A_{W\gamma}$	72.5%	0.2%	0.4%	-	87.2%	0.2%	0.5%	-	
$p_T(\gamma) > 60GeV, N_{jet} >= 0$									
	value	stat	syst	lumi	value	stat	syst	lumi	
$N^{sig}_{W\gamma}$	145.9	13.1	8.7	-	213.4	16.2	9.5	-	
$L_{W\gamma}[pb^{-1}]$	1024	-	-	37.9	1024	-	-	37.9	
$C_{W\gamma}$	59.8%	0.2%	3.6%	-	65.0%	0.2%	3.5%	-	
$A_{W\gamma}$	65.7%	0.3%	1.1%	-	77.6%	0.3%	1.9%	-	
$p_T(\gamma) > 100GeV, N_{jet} >= 0$									
	value	stat	syst	lumi	value	stat	syst	lumi	
$N^{sig}_{W\gamma}$	44.9	7.2	2.7	-	64.2	8.3		3.1	-
$L_{W\gamma}[pb^{-1}]$	1024	-	-	37.9	1024	-	-	37.9	
$C_{W\gamma}$	57.6%	0.6%	3.5%	-	62.4%	0.5%	3.5%	-	
$A_{W\gamma}$	66.6%	0.5%	1.7%	-	74.7%	0.4%	2.3%	-	

Table 31: Summary of input quantities for the calculation of the $W\gamma$ production cross sections. For each channel, the observed numbers of signal events after background subtraction, the correction factors , the acceptance factors $A_{W\gamma}$ and the integrated luminosities are given, with their statistical, systematic, and luminosity uncertainties.

	$Z\gamma \rightarrow ee\gamma$				$Z\gamma \rightarrow \mu\mu\gamma$			
	$p_T(\gamma) > 15GeV, N_{jet} = 0$							
	value	stat	syst	lumi	value	stat	syst	lumi
$N_{Z\gamma}^{sig}$	346.7	19.7	8.9	-	455.8	23.0	13.2	-
$L_{Z\gamma}[pb^{-1}]$	1024	-	-	37.9	1024	-	-	37.9
$C_{Z\gamma}$	39.7%	0.2%	4.5%	-	45.9%	0.3%	5.2%	-
$A_{Z\gamma}$	82.9%	0.2%	1.4%	-	91.5%	0.2%	1.6%	-
	$p_T(\gamma) > 15GeV, N_{jet} >= 0$							
	value	stat	syst	lumi	value	stat	syst	lumi
$N_{Z\gamma}^{sig}$	470.3	23.0	14.6	-	577.2	25.9	12.8	-
$L_{Z\gamma}[pb^{-1}]$	1024	-	-	37.9	1024	-	-	37.9
$C_{Z\gamma}$	42.1%	0.3%	4.4%	-	48.5%	0.4%	5.5%	-
$A_{Z\gamma}$	82.6%	0.2%	1.4%	-	91.5%	0.2%	1.6%	-
	$p_T(\gamma) > 60GeV, N_{jet} = 0$							
	value	stat	syst	lumi	value	stat	syst	lumi
$N_{Z\gamma}^{sig}$	22.4	4.9	1.3	-	29.9	5.7	1.6	-
$L_{Z\gamma}[pb^{-1}]$	1024	-	-	37.9	1024	-	-	37.9
$C_{Z\gamma}$	59.2%	0.3%	4.4%	-	64.1%	0.3%	4.4%	-
$A_{Z\gamma}$	83.4%	0.2%	0.8%	-	91.7%	0.2%	0.8%	-
	$p_T(\gamma) > 60GeV, N_{jet} >= 0$							
	value	stat	syst	lumi	value	stat	syst	lumi
$N_{Z\gamma}^{sig}$	35.9	6.3	2.4	-	40.9	6.8	2.2	-
$L_{Z\gamma}[pb^{-1}]$	1024	-	-	37.9	1024	-	-	37.9
$C_{Z\gamma}$	60.9%	0.3%	3.6%	-	64.5%	0.3%	3.5%	-
$A_{Z\gamma}$	83.6%	0.2%	0.5%	-	91.7%	0.2%	0.5%	-

Table 32: Summary of input quantities for the calculation of the $Z\gamma$ production cross sections. For each channel, the observed numbers of signal events after background subtraction, the correction factors ($C_{Z\gamma}$), the acceptance factors and the integrated luminosities are given, with their statistical, systematic, and luminosity uncertainties.

correlated uncertainties
photon recontruction and identification efficiency uncertainties
photon isolation efficiency uncertainties
Photon energy scale and resolution uncertainties
E_T^{miss} scale and resolution uncertainties
Jet energy scale and resolution uncertainties
background uncertainties
Acceptance uncertainties
luminosities measurement uncertainties
uncorrelated uncertainties
lepton recontruction and identification efficiency uncertainties
lepton isolation efficiency uncertainties
lepton energy/Momentum scale and resolution uncertainties
Trigger efficiency uncertainties

Table 33: The lists of correlated and uncorrelated uncertainties considered in combination of extended fiducial cross sections in muon and electron channels

To combine the uncorrelated uncertainties of each channel for combined cross section, the equation 21 is used. To combine the correlated uncertainties of each channel for combined cross section, the equation 22 is used. The way to get the final combined crosssection is shown in Equation 19.

$$\delta\sigma^{unc}(combined) = \frac{1}{\sqrt{w_e + w_\mu}} \tag{21}$$

$$\delta\sigma^{cor}(combined) = 0.5 \times (\delta\sigma^{cor}(e) + \delta\sigma^{cor}(\mu)) \tag{22}$$

$$\delta\sigma(combined) = \sqrt{\delta\sigma^{unc}(combined)^2 + \delta\sigma^{cor}(combined)^2} \tag{23}$$

The value of each components of extended cross sections are presented in Table 30, 31 and 32. The measured extended fiducial cross sections in exclusive 0 jet phase space and inclusive phase space for $W\gamma$ and $Z\gamma$ processes in electron and muon final states are presented in Table 34 and Table 35 respectively. The SM NLO cross sections have been corrected to the particle level. The correction procedure is described in 6.2. A comparison of the measured extended fiducial cross sections to SM model predictions are shown in Figure **??**, Figure **??** and Figure **??**. The SM model predictions shown in Table 34 and Table 35 have been corrected to particle level from parton level SM NLO predictions by MCFM generators, the detailed of corrections and SM predictions are discussed in next section.

	$\sigma^{extfid}[pb]$(measured)	$\sigma^{extfid}[pb]$(predicted)
	$p_T(\gamma) > 15 GeV and N_{jet} = 0$	
$pp \to e\nu\gamma$	$3.42 \pm 0.14(stat) \pm 0.50(syst) \pm 0.13(lumi)$	$2.84 \pm 0.23(syst)$
$pp \to \mu\nu\gamma$	$3.23 \pm 0.14(stat) \pm 0.48(syst) \pm 0.12(lumi)$	$2.84 \pm 0.23(syst)$
$pp \to l\nu\gamma$	$3.32 \pm 0.10(stat) \pm 0.48(syst) \pm 0.12(lumi)$	$2.84 \pm 0.23(syst)$
$pp \to e^+e^-\gamma$	$1.03 \pm 0.06(stat) \pm 0.13(syst) \pm 0.04(lumi)$	$1.08 \pm 0.10(syst)$
$pp \to \mu^+\mu^-\gamma$	$1.06 \pm 0.05(stat) \pm 0.12(syst) \pm 0.04(lumi)$	$1.08 \pm 0.10(syst)$
$pp \to l^+l^-\gamma$	$1.05 \pm 0.04(stat) \pm 0.12(syst) \pm 0.04(lumi)$	$1.08 \pm 0.10(syst)$
	$p_T(\gamma) > 60 GeV and N_{jet} = 0$	
$pp \to e\nu\gamma$	$0.14 \pm 0.02(stat) \pm 0.02(syst) \pm 0.01(lumi)$	$0.13 \pm 0.02(syst)$
$pp \to \mu\nu\gamma$	$0.15 \pm 0.02(stat) \pm 0.02(syst) \pm 0.01(lumi)$	$0.13 \pm 0.02(syst)$
$pp \to l\nu\gamma$	$0.15 \pm 0.01(stat) \pm 0.02(syst) \pm 0.01(lumi)$	$0.13 \pm 0.02(syst)$
$pp \to e^+e^-\gamma$	$0.044 \pm 0.010(stat) \pm 0.004(syst) \pm 0.002(lumi)$	$0.043 \pm 0.004(syst)$
$pp \to \mu^+\mu^-\gamma$	$0.050 \pm 0.010(stat) \pm 0.004(syst) \pm 0.002(lumi)$	$0.043 \pm 0.004(syst)$
$pp \to l^+l^-\gamma$	$0.047 \pm 0.007(stat) \pm 0.004(syst) \pm 0.002(lumi)$	$0.043 \pm 0.004(syst)$
	$p_T(\gamma) > 100 GeV and N_{jet} = 0$	
$pp \to e\nu\gamma$	$0.040 \pm 0.011(stat) \pm 0.009(syst) \pm 0.001(lumi)$	$0.034 \pm 0.004(syst)$
$pp \to \mu\nu\gamma$	$0.026 \pm 0.008(stat) \pm 0.003(syst) \pm 0.001(lumi)$	$0.034 \pm 0.004(syst)$
$pp \to l\nu\gamma$	$0.030 \pm 0.006(stat) \pm 0.006(syst) \pm 0.001(lumi)$	$0.034 \pm 0.004(syst)$

Table 34: Extended fiducia cross sections of the $pp \to l\nu\gamma + X$ and $pp \to ll\gamma + X$ process at $\sqrt{s} = 7$ TeV in exclusive 0 jet phase space. Both, experimental measurement and SM model NLO prediction are given. The SM NLO cross sections have been corrected to the particle level. The correction procedure is described in 6.2. The extended fiducial phase space is defined in Table 22.

6 Theoretical Predictions for $W\gamma$ and $Z\gamma$ production

6.1 Parton level cross section predictions

Our SM cross section predictions are obtained using the event generator MCFM6.1 [referenceMCFM] . The final states $l\nu\gamma + X$ and $ll\gamma + X$ are generated at next-to-leading -order (NLO) with the fragmentation (F) of quark/gluons to photons enabled. The MCFM program has the advantage that it includes sources of photons from direct $W\gamma$ and $Z\gamma$ di-boson production, from final state radiation off the leptons in the W/Z decays and from quark/gluon fragmentation into an isolated photon. The parameters used in the event generation are summarized in Table 36.

To compare the NLO SM predictions to our measurements of $p + p \to l\nu\gamma$ + X and $p + p \to l^+l^-\gamma$ + X we start with the MCFM events generated with the parameters summarized in Table 36, and apply at the truth-level the parton kinematic cuts summarized in Table 37. This parton-level phase space is the same as the particle-level phase space chosen for our "Extended Fiducial Cross Section" measurements (see Table 22). The parton-level SM cross sections, after applying the fiducial cuts in Table 37, are summarized in Table 38 . The cross sections can be quoted as "inclusive", using only the lepton and photon cuts in Table 37, or "zero jets" where this requires a choice of kinematic cuts on the single quark/gluon produced in the generated events. Guided by considerations of jet energy resolution and statistics available in our measured events, we define "zero-jet" events to be those with no quark/gluon with $|\eta| < 4.4$ and $E_T > 30$ GeV. The MCFM NLO cross section prediction should be most precise for events with "zero-jets", since it is LO in α_s with only one radiated quark or gluon. Therefore in order to make the most precise test of SM theory we choose to use the $p + p \to l\nu\gamma$ + zero-jet and $p + p \to l^+l^-\gamma$ + zero-jet MCFM NLO cross section predictions.

	$\sigma^{extfid}[pb]$(measured)	$\sigma^{extfid}[pb]$(predicted)
	$p_T(\gamma) > 15 GeV and N_{jet} >= 0$	
$pp \to e\nu\gamma$	$4.35 \pm 0.16(stat) \pm 0.64(syst) \pm 0.16(lumi)$	$3.70 \pm 0.32(syst)$
$pp \to \mu\nu\gamma$	$4.82 \pm 0.15(stat) \pm 0.64(syst) \pm 0.18(lumi)$	$3.70 \pm 0.32(syst)$
$pp \to l\nu\gamma$	$4.60 \pm 0.11(stat) \pm 0.64(syst) \pm 0.17(lumi)$	$3.70 \pm 0.32(syst)$
$pp \to e^+e^-\gamma$	$1.32 \pm 0.07(stat) \pm 0.16(syst) \pm 0.05(lumi)$	$1.23 \pm 0.12(syst)$
$pp \to \mu^+\mu^-\gamma$	$1.27 \pm 0.06(stat) \pm 0.15(syst) \pm 0.05(lumi)$	$1.23 \pm 0.12(syst)$
$pp \to l^+l^-\gamma$	$1.29 \pm 0.05(stat) \pm 0.15(syst) \pm 0.05(lumi)$	$1.23 \pm 0.12(syst)$
	$p_T(\gamma) > 60 GeV and N_{jet} >= 0$	
$pp \to e\nu\gamma$	$0.36 \pm 0.03(stat) \pm 0.03(syst) \pm 0.01(lumi)$	$0.26 \pm 0.03(syst)$
$pp \to \mu\nu\gamma$	$0.41 \pm 0.03(stat) \pm 0.03(syst) \pm 0.02(lumi)$	$0.26 \pm 0.03(syst)$
$pp \to l\nu\gamma$	$0.38 \pm 0.02(stat) \pm 0.03(syst) \pm 0.02(lumi)$	$0.26 \pm 0.03(syst)$
$pp \to e^+e^-\gamma$	$0.069 \pm 0.012(stat) \pm 0.006(syst) \pm 0.003(lumi)$	$0.058 \pm 0.005(syst)$
$pp \to \mu^+\mu^-\gamma$	$0.068 \pm 0.011(stat) \pm 0.005(syst) \pm 0.003(lumi)$	$0.058 \pm 0.005(syst)$
$pp \to l^+l^-\gamma$	$0.068 \pm 0.008(stat) \pm 0.005(syst) \pm 0.003(lumi)$	$0.058 \pm 0.005(syst)$
	$p_T(\gamma) > 100 GeV and N_{jet} >= 0$	
$pp \to e\nu\gamma$	$0.114 \pm 0.018(stat) \pm 0.010(syst) \pm 0.004(lumi)$	$0.082 \pm 0.006(syst)$
$pp \to \mu\nu\gamma$	$0.135 \pm 0.018(stat) \pm 0.010(syst) \pm 0.005(lumi)$	$0.082 \pm 0.006(syst)$
$pp \to l\nu\gamma$	$0.125 \pm 0.013(stat) \pm 0.010(syst) \pm 0.005(lumi)$	$0.082 \pm 0.006(syst)$

Table 35: Extended fiducia cross sections of the $pp \to l\nu\gamma + X$ and $pp \to ll\gamma + X$ process at $\sqrt{s} = 7$ TeV in inclusive phase space. Both, experimental measurement and SM model NLO prediction are given. The SM NLO cross sections have been corrected to the particle level. The correction procedure is described in 6.2. The extended fiducial phase space is defined in Table 22.

The uncertainties on the parton level cross section predictions include the following:

- renormalisation and factorisation scales uncertainty:

  This uncertainty is quoted by varying of the renormalisation and factorisation scales by factors of two around the nominal scales.

- PDF uncertainty: The uncertainty due to PDF sets is derived using the MSTW2008PDF error eigenvector sets at the 90% C.L. limit. The relative uncertainties on the cross section predictions is found to be 5% for both $W\gamma/Z\gamma$ production.

- Fragmentation photons uncertainty: This uncertainty is quoted for the choice of the isolation cut at parton level affecting the diagrams with a photon from fragmentation off a final state parton (fig. 2). As described above, in this analysis the NLO corrections are calculated setting the parameter ε_h=0.5, corresponding to a parton level isolation $E^{iso}/E^{\gamma} < 0.5$. Considering the potential difference between parton level isolation E_{iso} and photon isolation at reconstruction level, uncertainty on cross section calculation due to the choice of the ε_h generator parameter is estimated looking at the variation of the NLO cross section prediction when its value is shifted by 100% (i.e. from ε_h=0 to ε_h=1.0). We quote the maximum variation in cross section as systematic uncertainty on the ε_h choice.

  It is important to notice that the fraction of events with photons from fragmentation is very hard to predict even with MC simulation. In fact important cancellations (due to virtual gluon emission diagrams) occur in the calculation of the NLO cross sections.

The break down of uncertainties on the parton level cross section predictions for $W\gamma$ and $Z\gamma$ are shown in Table 39.

Parameter	MCFM setting
Select colliding particles	pp collisions at $\sqrt{s}$ = 7 TeV
Parton Distribution functions	MSTW2008nl
QCD and factorization scales	$\mu_{QCD} = \mu_{fact} = M_W$ = 80.4 GeV
Photon isolation	$\varepsilon_h < 0.5$ with cone isolation $\Delta R(\gamma) = 0.4$
quark/gluon fragmentation to photon	BFGsetII with $\mu_{frag} = M_W$ = 80.4 GeV
Event generation at NLO + F	MCFM selection 'tota'
Process selection	290 for $pp \to l^+ \nu\gamma$
	295 for $pp \to l^- \nu\gamma$
	300 for $pp \to l^+ l^- \gamma$
Electroweak parameters	Default settings in MCFM

Table 36: The run parameters settings for MCFM6.1 generation of NLO SM events $pp \to l^\pm \nu\gamma + X$ $pp \to l^+\, l^- \gamma + X$

Partons	kinematic selection cuts
$l^\pm$ and ν	$E_T > 25$ GeV and $\lvert\eta\rvert < 2.47$
photon	$E_T > 15$ or 60 or 100 GeV and $\lvert\eta\rvert < 2.37$
	$\Delta R(l\text{-}\gamma) > 0.7$
count quark/gluon as a "jet " if	$\Delta R(l\text{-q/g}) > 0.6$ and $\Delta R(\gamma\text{-q/g}) > 0.6$
	and $\lvert\eta\rvert < 4.4$ and $E_T > 30$ GeV

Table 37: The kinematic cuts used to select the MCFM NLO SM events for $pp \to l^\pm \nu\gamma + X$ and $pp \to l^+\, l^- \gamma + X$

Channel	$E_T(\gamma)$	Cross section	Cross section
		inclusive	zero-jet
$pp \to l^+ \nu\gamma + X$	> 15 GeV	1.99 pb	1.42 pb
$pp \to l^- \nu\gamma + X$		1.59 pb	1.19 pb
$pp \to l^\pm \nu\gamma + X$		3.58 pb	2.61 pb
$pp \to l^+ \nu\gamma + X$	> 60 GeV	150.5 fb	68.3 fb
$pp \to l^- \nu\gamma + X$		104.6 fb	49.3 fb
$pp \to l^\pm \nu\gamma + X$		255 fb	118 fb
$pp \to l^+ \nu\gamma + X$	> 100 GeV	49.2 fb	18.7 fb
$pp \to l^- \nu\gamma + X$		31.0 fb	12.2 fb
$pp \to l^\pm \nu\gamma + X$		80.2 fb	30.6 fb
$pp \to l^+\, l^- \gamma + X$	> 15 GeV	1.22 pb	1.03 pb
$pp \to l^+\, l^- \gamma + X$	> 60 GeV	58.1 fb	39.9 fb

Table 38: NLO SM parton-level cross sections for $pp \to l^\pm \nu\gamma + X$ and $pp \to l^+\, l^- \gamma + X$ using events generated with MCFM6.1 with the input parameters summarized in Table 36 and the kinematic cuts given in Table 37

Source of systematics	$l\nu\gamma$	$l^+l^-\gamma$
renormalization/fragmentation scale uncertainty	4.5%	1%
PDF uncertainty	4.8%	3.2%
photon isolation	4.7%	8.4%
Overall Uncertainty	8.1%	9.0%

Table 39: Uncertainty of NLO Standard Model cross section predictions for $W\gamma$ and $Z\gamma$ process at $\sqrt{s}$ of 7 TeV for the inclusive and fiducial regions defined in Table 22.

6.2 Corrections from Parton-level Predictions to Particle-level Predictions

To make a comparison of the SM zero-jet cross section predictions to our measured cross sections we must correct for the difference between jets defined at the parton level (single quark or gluon) and jets defined at the particle level using the anti-kt algorithm as is done for our cross section measurement. This affects both the cut on jets with $|\eta| < 4.4$ and $E_T > 30$ GeV, and the jets contributions to the relative photon isolation defined by $\varepsilon_h < 0.5$, where ε_h is defined at parton level as the ratio between sum of the energy carried by partons in the cone $\Delta R < 0.4$ around the photon and the energy carried by the photon.

Ideally we would determine this by taking the MCFM parton-level events and pass them through a shower MC to measure the change in jet definition from the single partons to the "dressed" particle-level jets obtained from the anti-kt clustering algorithm. However since we can not do this for NLO MCFM events, due to double counting in the shower MC, we use the ALPGEN+HERWIG (for $W\gamma$) and SHERPA (for $Z\gamma$) MC samples (see Section 1.2). These MC samples have both truth-level partons and hadrons that can be used to form antikt-clustered jets. This allows us to scale the SM cross section predictions in parton level given in in Table 38 to cross section in particle-level that can be directly compared to our measurements. The procedure is the following:

- Select fiducial events by applying the kinematic cuts in Table 37 to the truth-level leptons and photon.
- Select zero-jet events using cuts on the parton truth-level as defined in Table 37. Using the truth-level partons, require that the relative photon isolation $\varepsilon_h < 0.5$. Count the number of zero-jet events that pass this photon isolation selection = $N_{fiducial}(jet_{parton}\ ,\ \gamma_{iso-parton}\ )$.
- Repeat the above selection of parton level zero-jet events that pass the photon isolation $\varepsilon_h^p < 0.5$, but use ε_h^p (particle level isolation) defined in particle-level rather than parton level ε_h defined in parton level. Count the number of these events = $N_{fiducial}(jet_{parton}\ ,\ \gamma_{iso-particle}\ )$.
- Repeat the above selection of zero-jet events that pass the photon isolation $\varepsilon_h^p < 0.5$, but use particles level jets reconstructed from particles with the antikt clustering algorithm. Count the number of these events = $N_{fiducial}(jet_{particle}\ ,\ \gamma_{iso-particle}\ )$.
- Define a scale factor $C*^{parton->particle}_{W(Z)\gamma}$ that transforms the parton-level SM cross sections to particle-level cross sections that can be directly compared to our measurements:

$$C*^{parton->particle}_{W(Z)\gamma} = N_{fiducial}(jet_{parton}, \gamma_{iso-parton})/N_{fiducial}(jet_{particle}, \gamma_{iso-particle}) \tag{24}$$

According to this definition, the parton level SM cross sections predictions (σ_{NLO}^{parton}) can be corrected to particle level ($\sigma_{NLO}^{particle}$) using Equation 25.

$$\sigma_{NLO}^{particle} = \sigma_{NLO}^{parton} / C*^{parton->particle}_{W(Z)\gamma} \tag{25}$$

- The $C^{*parton->particle}_{W(Z)\gamma}$ can be break down into two factors T_{njet} and $T_{\gamma iso}$ as Equation 26. T_{njet} and $T_{\gamma iso}$ are defined in Equation 27 and Equation 28, they reflect the impact of discrepancy between parton and particles level in jet definitions and photon isolation definitions respectively.

$$C^{*parton->particle}_{W(Z)\gamma} = (T_{njet} * T_{\gamma iso}) \quad (26)$$

$$T_{njet} = N_{fiducial}(jet_{parton}, \gamma_{iso-particle})/N_{fiducial}(jet_{particle}, \gamma_{iso-particle}). \quad (27)$$

$$T_{\gamma iso} = N_{fiducial}(jet_{parton}, \gamma_{iso-parton})/N_{fiducial}(jet_{parton}, \gamma_{iso-particle}). \quad (28)$$

The $C^{*parton->particle}_{W(Z)\gamma}$ scale factors are tabulated in Table 42 and 41. The main part of systematic uncertainties are due to uncertainty in parton showering modelling and the matching between matrix element calculations and parton showering. It is evaluated by comparing different full simulation MC with different parton shower modelling.

According to Table 41, We quote the maxinum discrepancy in $C^{*parton->particle}_{W(Z)\gamma}$ between Standard model Alpgen $W\gamma$ and Sherpa $W\gamma$ sample as uncertainty for $C^{*parton->particle}_{W\gamma}$.

According to Table 42, We quote quoting the maxinum discrepancy between Standard model Sherpa $Z+\gamma$+0/1/2/3 jets and SM Sherpa $Z+\gamma$+0/1 jet samples as uncertainty for $C^{*parton->particle}_{Z\gamma}$.

The NLO SM cross sections predictions for $p+p \rightarrow l\nu\gamma$ + 0 jet and $p+p \rightarrow l^{+}l^{-}\gamma$ + 0 jet are obtained by scaling the parton-level cross sections in Table 38 by the $C^{*parton->particle}_{Z\gamma}$ for each channel using Equation 25. These are summarized in Table 40 , and also in Table 35 and Table 34 along with our measured cross sections.

Table 40: Parton level and particle level NLO Standard Model cross section predictions of the $pp \rightarrow l\nu\gamma+X$ abd $pp \rightarrow ll\gamma+X$ process at $\sqrt{s}$ of 7 TeV for the inclusive and exclusive 0 jet phase space regions defined in Table 22. The correction factors $C^{*parton->particle}_{W(Z)\gamma}$,obtained from Alpgen $W\gamma + 0/1/2/3/4/5 jets$ (from $Z+\gamma+0/1/2/3jets$), is also presented.

Process	σ^{parton}_{NLO} (pb)	$C^{*parton->particle}_{W(Z)\gamma}$	$\sigma^{particle}_{NLO}$ (pb)	σ^{parton}_{NLO}(pb)	$C^{*parton->particle}_{W(Z)\gamma}$	$\sigma^{particle}_{NLO}$ (pb)
	$p_T(\gamma) > 15GeV, N_{jet} = 0$			$p_T(\gamma) > 15GeV, N_{jet} >= 0$		
$l\nu\gamma$	2.61 ± 0.21	0.92 ± 0.02	2.84 ± 0.23	3.58 ± 0.29	0.96 ± 0.03	3.70 ± 0.32
$l^{+}l^{-}\gamma$	1.03 ± 0.10	0.95 ± 0.01	1.08 ± 0.10	1.22 ± 0.11	0.99 ± 0.03	1.23 ± 0.12
	$p_T(\gamma) > 60GeV, N_{jet} = 0$			$p_T(\gamma) > 60GeV, N_{jet} >= 0$		
$l\nu\gamma$	0.118 ± 0.010	0.88 ± 0.07	0.134 ± 0.016	0.255 ± 0.020	0.98 ± 0.09	0.260 ± 0.031
$l^{+}l^{-}\gamma$	0.040 ± 0.0039	0.94 ± 0.03	0.043 ± 0.004	0.058 ± 0.005	0.99 ± 0.02	0.59 ± 0.005
	$p_T(\gamma) > 100GeV, N_{jet} = 0$			$p_T(\gamma) > 100GeV, N_{jet} >= 0$		
$l\nu\gamma$	0.031 ± 0.002	0.92 ± 0.09	0.034 ± 0.004	0.080 ± 0.006	0.98 ± 0.01	0.082 ± 0.006

7 Anomalous Triple Gauge-Boson Couplings in $W\gamma$ Production

7.1 Introduction

The $W\gamma$ process is directly sensitive to the triple gauge boson couplings predicted by the non-Abelian $SU(2)_L \times U(1)_Y$ gauge group of the electroweak sector. Physics beyond the SM (composite structure of W and Z bosons, new vector bosons, etc.) will enhance the $WW\gamma$ coupling, thus enhance the $W\gamma$ cross sections and alter the production kinematics (especially the photon p_T spetrum).

Table 41: Factors for correcting the predicted parton based cross section values to particle based cross section values of $pp \to l\nu\gamma + X$ at $\sqrt{s}$ of 7 TeV for fiducial regions defined in Table 22.

Process	Generator	model	T_{njet}	$T_{\gamma iso}$	$C_{W(Z)\gamma}^{parton->particle}$	$T_{\gamma iso}$	$C_{W(Z)\gamma}^{parton->particle}$
			$p_T(\gamma) > 15GeV, N_{jet} = 0$			$p_T(\gamma) > 15GeV, N_{jet} >= 0$	
$l\nu\gamma + 0-5jet$	Alpgen	SM	0.95	0.97	0.92	0.96	0.96
$l\nu\gamma + 0/1jet$	Sherpa	SM	0.99	0.91	0.91	0.93	0.93
$l\nu\gamma + 0/1jet$	Sherpa	$\lambda_\gamma = 0.2$	0.99	0.94	0.93	0.96	0.96
$l\nu\gamma + 0/1jet$	Sherpa	$\kappa_\gamma = 1.0$	0.99	0.95	0.94	0.96	0.96
			$p_T(\gamma) > 60GeV, N_{jet} = 0$			$p_T(\gamma) > 60GeV, N_{jet} >= 0$	
$l\nu\gamma + 0-5jet$	Alpgen	SM	0.91	0.97	0.88	0.98	0.98
$l\nu\gamma + 0/1jet$	Sherpa	SM	1.03	0.94	0.98	0.96	0.96
$l\nu\gamma + 0/1jet$	Sherpa	$\lambda_\gamma = 0.2$	0.99	0.96	0.95	0.97	0.97
$l\nu\gamma + 0/1jet$	Sherpa	$\kappa_\gamma = 1.0$	0.99	0.97	0.95	0.98	0.98
			$p_T(\gamma) > 100GeV, N_{jet} = 0$			$p_T(\gamma) > 100GeV, N_{jet} >= 0$	
$l\nu\gamma + 0-5jet$	Alpgen	SM	0.94	0.98	0.92	0.98	0.98
$l\nu\gamma + 0/1jet$	Sherpa	SM	1.04	0.97	1.01	0.98	0.98
$l\nu\gamma + 0/1jet$	Sherpa	$\lambda_\gamma = 0.2$	0.97	0.99	0.96	0.99	0.99
$l\nu\gamma + 0/1jet$	Sherpa	$\kappa_\gamma = 1.0$	0.98	0.99	0.97	0.99	0.99

Table 42: Factors for correcting the predicted parton based cross section values to particle based cross section values of $pp \to l^+l^-\gamma + X$ at $\sqrt{s}$ of 7 TeV for fiducial regions defined in Table 22.

Process	Generator	model	T_{njet}	$T_{\gamma iso}$	$C_{W(Z)\gamma}^{parton->particle}$	$T_{\gamma iso}$	$C_{W(Z)\gamma}^{parton->particle}$
			$p_T(\gamma) > 15GeV, N_{jet} = 0$			$p_T(\gamma) > 15GeV, N_{jet} >= 0$	
$ll\gamma + 0-3jet$	Sherpa	SM	0.96	0.99	0.95	0.99	0.99
$ll\gamma + 0/1jet$	Sherpa	SM	0.97	0.99	0.96	0.98	0.98
$ll\gamma + 0/1jet$	Sherpa	$h3_\gamma = 0.03$	0.98	0.98	0.96	0.97	0.97
$ll\gamma + 0/1jet$	Sherpa	$h3_Z = 0.03$	0.97	0.98	0.95	0.97	0.97
$ll\gamma + 0/1jet$	Sherpa	$h4_\gamma = 0.0005$	0.97	0.98	0.95	0.98	0.98
$ll\gamma + 0/1jet$	Sherpa	$h4_Z = 0.0005$	0.98	0.98	0.96	0.96	0.96
			$p_T(\gamma) > 60GeV, N_{jet} = 0$			$p_T(\gamma) > 60GeV, N_{jet} >= 0$	
$ll\gamma + 0-3jet$	Sherpa	SM	0.95	0.99	0.94	0.99	0.99
$ll\gamma + 0/1jet$	Sherpa	SM	0.97	0.98	0.96	0.97	0.97
$ll\gamma + 0/1jet$	Sherpa	$h3_\gamma = 0.03$	0.98	0.99	0.97	0.97	0.97
$ll\gamma + 0/1jet$	Sherpa	$h3_Z = 0.03$	0.97	0.98	0.95	0.97	0.97
$ll\gamma + 0/1jet$	Sherpa	$h4_\gamma = 0.0005$	0.98	0.99	0.97	0.98	0.98
$ll\gamma + 0/1jet$	Sherpa	$h4_Z = 0.0005$	0.99	0.99	0.97	0.97	0.97

The most general Lorentz-invariant Lagrangian that describes the $WW\gamma$ coupling has seven independent dimensionless couplings g_1^γ, κ_γ, λ_γ, g_4^γ, g_5^γ,$\widetilde{\kappa}_\gamma$, and $\widetilde{\lambda}_\gamma$. By requiring CP invariance and $SU(2)\times U(1)$ gauge invariance only two independent parameters remain:κ_γ and λ_γ. In the SM, $\kappa_\gamma = 1$ and $\lambda_\gamma = 0$. We define aTGCs to be deviations from the SM predictions, so instead of using κ_γ we define $\Delta\kappa_\gamma \equiv \kappa_\gamma - 1$. These couplings parameters are related to the electromagnetic properties of the W boson. As shown in Equation 29 and Equation 30, the linear combinations of $\Delta\kappa_\gamma$ and λ_γ are the magnetic dipole and electric quadrupole moments of the W boson.

$$\mu_W = \frac{e}{2M_W}(2+\Delta\kappa_\gamma+\lambda_\gamma) \tag{29}$$

$$Q_W = -\frac{e}{M_W^2}(1+\Delta\kappa_\gamma-\lambda_\gamma) \tag{30}$$

where μ_W and Q_W are the magnetic dipole and electric quadrupole moments of the W boson, respectively.
To assure that the $W\gamma$ cross section does not violate unitarity, a form factor, with a common scale Λ for each non-SM coupling parameter, is introduced to modify the terms as $a0 \rightarrow a0/(1+\hat{s}/\Lambda^2)^2$, where $a0 = \kappa_\gamma, \lambda_\gamma$, and $\hat{s}$ is the square of the partonic center-of-mass energy. In this analysis, the scale is set to:

- 2 TeV, to compare with D0 published results;
- infinite, to compare with CMS published results.

7.2 The method for measurement in $W\gamma$ channel

Contributions from anomalous couplings will increase the $W\gamma$ production cross section and yield photons of higher energy than in the SM process. Measurement in high photon p_T extended fiducial phase space is more sensitive to ATGC coupling. In this study, only $W\gamma$ candidates events within high p_T exclusive 0 jet extended fiducial phase space (${p_T}_\gamma > 100$GeV and $N_{jet} = 0$) as defined in table 23, are used to extract the ATGC limits for κ_γ and λ_γ. The limit is set based on counting of events in high p_T extended fiducial phase space, not based on the photon p_T shape. The objects and event level selection for ATGC study are exactly kept the same with cross-setion measurement(jet veto is applied) which are described in Section 5.
MCFM generator is also used as $W\gamma$ ATGC generator. Similar with $Z\gamma$ ATGC study part, since we know the cross-section can be descirbed as a second order polynomial function as ATGC parameters, so we just generate 100 ATGC samples for both $\Delta\kappa_\gamma$ and λ_γ parameter, and calculate the expected signal events number in our selected extended fiducial phase space:

$$N_{sig}^{expect} = \sigma_{fiducial}^{W\gamma} \times C_{W\gamma} \times A_{W\gamma} \times L/C_{W\gamma}^{*parton\rightarrow particle} \tag{31}$$

and then perform a fit with second order poynomial function. From the second order poynomial function, we can directly get the N_{sig}^{expect} at any $\Delta\kappa_\gamma$ and λ_γ point.
In Fig **??**(Λ =2TeV) and Fig **??**(Λ =10000TeV), we show the fitting for each ATGC parameters(just use μ channel as an example), and the fitting functions are summarized in Table 43 .

To set limits on $\Delta\kappa_\gamma$ and λ_γ, we also use Bayesian approach, first obtain the probability distribution of $P(a0|I_{w\gamma}^e, I_{w\gamma}^\mu)$ (where $a0 = \Delta\kappa_\gamma$ or λ_γ, $I_{W\gamma}^e$ and $I_{W\gamma}^\mu$ denote all the inputs for high p_T exclusive 0 jet extended fiducial cross section for electron and muon channel respectly in Table 24 and their systematic in Table 44), by integrating all nuisance parameters (including uncertainty in background estimations and signal acceptance and correction factors).

Table 43: Fitting parameters of expected number of $W\gamma$ signal events as a function of ATGC parameters

muon channel			
Λ=2TeV	p0	p1	p2
$\Delta\kappa_\gamma$	51.7 ± 5.52	-1.71 ± 3.27	16.2 ± 2.12
λ_γ	$1.79e3 \pm 1.48e3$	16 ± 41.9	16.2 ± 1.87
Λ=10000TeV	p0	p1	p2
$\Delta\kappa_\gamma$	63.7 ± 5.86	-1.68 ± 3.49	16.2 ± 2.16
λ_γ	$2.7e3 \pm 1.53e3$	21.3 ± 43.6	16.3 ± 1.89
electron channel			
Λ=2TeV	p0	p1	p2
$\Delta\kappa_\gamma$	37.6 ± 4.71	-1.24 ± 2.79	11.8 ± 1.8
λ_γ	$1.3e3 \pm 1.26e3$	11.6 ± 35.7	11.8 ± 1.6
Λ=10000TeV	p0	p1	p2
$\Delta\kappa_\gamma$	46.3 ± 5	-1.22 ± 2.97	11.8 ± 1.84
λ_γ	$1.96e3 \pm 1.31e3$	15.5 ± 37.2	11.9 ± 1.61

7.3 Addtional systematics for $W\gamma$ ATGC limits : QCD scale dependence

The renormalisation and factorisation scales uncertainty has been mentioned in Section 6 in SM predictions. However this uncertainty may not cover the whole ATGC grid points. In this subsection, we vary the renormalisation and factorisation scales by factors of two around the nominal scales for the whole ATGC grid, and quote the maximum variations in cross section predictions of ATGC models. As shown in Figure **??** and Figure **??**, the expected $W\gamma$ signal events in μ channel as a functions of aTGCs are calculated using MCFM with different QCD scale. The maximum variations are summarized in Table 44.

7.4 The Result

The PDF function for $P(a0|I^e_{w\gamma}, I^\mu_{w\gamma})$ for $W\gamma$ analysis is similar to the one defined in Equation 36 of Section 8 for $Z\gamma$ analysis. Figure **??** shows the $-Log[P(\Delta\kappa_\gamma)|I^\mu_{W\gamma}, I^e_{W\gamma}]$ distribution of $\Delta\kappa_\gamma$ for combined channel as an example. We use the similar method as in $Z\gamma$ channel to extract the ATGC limits. By doing an integral with the probability density function in equation 39 and 40, we then obtain the ATGC limits at 95% CL. In Table 46, we summarize our extracted ATGC limits with systematics considered.

In the ATGC limit extraction based on Bayesian approach, the values of $C_{W\gamma} \times A_{W\gamma}$ (see equation 31) are obtained based on inputs from Table 30 and 31.

We assume the values of $C_{W\gamma} \times A_{W\gamma}$ do not vary significantly, in the extended fiducial phase space for the ATGC limit extraction, between the SM $W\gamma$ production and the non-SM $W\gamma$ production in the ATGC parameter space we are exploring. Table 45 shows the $C_{W\gamma} \times A_{W\gamma}$ values obtained from the SM MC samples and from ATGC MC samples that are generated at a few ATGC points. The $C_{W\gamma} \times A_{W\gamma}$ values vary by about $\sim 11\%$. This difference has not been added as an additional systematics in the ATGC limit extraction.

We also compare our results to those published by other experiments such as D0s results with $4.2fb^{-1}$ at $\Lambda = 2$TeV and CMS results with $35pb^{-1}$ at $\Lambda = infinite$, and summarized in table 47 and Figure **??**. In order to make sure our Bayesian limit is robust, we perform addtional cross checks using frequentist coverage test, and the results show that it is consistent with Bayesian limit. The details of this

Table 44: The systematics used in $W\gamma$ ATGC limits setting. The uncertainties due to QCD scale dependence is mentioned in Section 7.3.

systematics	fractional uncertainty(e channel)	fractional uncertainty(μ channel)
Trigger efficiency	0.5%	1.0%
electron reco efficiency	0.7%	
electron ID efficiency	1.5%	
electron iso efficiency	1.0%	
muon ID efficiency		0.7%
Momentum scale and resolution		1.0%
photon ID efficiency	4.3%	4.3%
photon isolation efficiency	2.5%	2.5%
EM scale and resolution	2.5%	1.5%
Jet scale	4.8%	6.8%
Jet resolution	1.0%	1.0%
luminosity	3.7%	3.7%
background	45.0%	17.0 %
MET scale/resolution uncertainty	3.2%	3.0%
$A_{W\gamma} * C_{W\gamma}$ within ATGC sample	11.0%	11.0%
theoretical		
QCD scale dependence in ATGC grid for λ	6.0%	6.0%
QCD scale dependence in ATGC grid for $\Delta\kappa$	4.0%	4.0%
PDF	4.6%	4.6%

coverage test are show in Section **??**.

8 Set limits on $Z\gamma$ anomalous couplings

8.1 Introduction

The triple gauge boson couplings (through $ZZ\gamma$ vertex and $Z\gamma\gamma$ vertex) in $Z\gamma$ process vanish in the SM at tree level. Physics beyond the SM could enhance the $Z\gamma\gamma$ and $ZZ\gamma$ coupling, which are forbidden in SM physics.

The most general Lorentz and gauge invariant $ZV\gamma$ coupling, where V stands for either Z or γ , is described by eight coupling parameters: $h_i^V (i = 1,2,3,4)$. Combinations of the CP-conserving (CP-violating) parameters h_3^V and h_4^V (h_1^V and h_2^V) correspond to the electric (magnetic) dipole and magnetic (electric) quadrupole transition moments of the $ZV\gamma$ vertex. Non-zero (anomalous) values of the h_i^V couplings result in an increase of the Z cross-section, especially for large photon transverse energies. Partial wave unitarity of the general $ff \rightarrow Z\gamma$ process restricts $ZV\gamma$ couplings to vanish at high energies. Therefore, the couplings are parameterized with form-factors:

$$h_i^V = \frac{h_{i0}^V}{(1+\hat{s}/\Lambda^2)^n} \quad (32)$$

Acceptance and Correction factors for $W\gamma$ in different models					
$p_T(\gamma) > 100GeV$ and $N_{jet} == 0$					
		Muon channel			
	Model	$C_{W\gamma}$	$A_{W\gamma}$	$C_{W\gamma} * A_{W\gamma}$	rel
Sherpa	SM	0.567	0.668	0.379	-
Sherpa	$\Lambda_\gamma = 0.2$	0.604	0.695	0.419	+10.7%
Sherpa	$\Lambda_\gamma = 0.2$ $\Delta\kappa_\gamma = 1.0$	0.623	0.663	0.413	+9.1%
Sherpa	$\Lambda_\gamma = 0.2$ $\Delta\kappa_\gamma = -1.0$	0.605	0.668	0.404	+6.7%
Sherpa	$\Delta\kappa_\gamma = 1.0$	0.618	0.658	0.407	+7.5%
Sherpa	$\Delta\kappa_\gamma = -1.0$	0.562	0.681	0.383	+1.1%
Alpgen	SM	0.565	0.717	0.405	+6.9%

Table 45: The variations of acceptance and Correction factors for $W\gamma$ in different models

Table 46: The observed ATGC limits considering systematics in $W\gamma$ electron channel and muon channel, as well as the observed and expected combined limits from both channels.

channel	ATGC pars	Λ=2TeV	Λ=10000TeV
muon channel	$\Delta\kappa_\gamma$	(-0.37,0.42)	(-0.32,0.38)
	λ_γ	(-0.080,0.087)	(-0.068,0.071)
elec channel	$\Delta\kappa_\gamma$	(-0.56,0.60)	(-0.51,0.55)
	λ_γ	(-0.093,0.079)	(-0.089,0.085)
combined	$\Delta\kappa_\gamma$	(-0.36,0.41)	(-0.33,0.37)
	λ_γ	(-0.079,0.074)	(-0.060,0.060)
expect(combined)	$\Delta\kappa_\gamma$	(-0.36,0.40)	(-0.33,0.36)
	λ_γ	(-0.075,0.066)	(-0.063,0.055)

where $\hat{s}$ is the square of the $Z\gamma$ invariant mass, Λ is a form-factor scale, and h_{i0}^V are values of couplings at low energy. We take n = 3 for $h_{1,3}^V$, and n = 4 for $h_{2,4}^V$.

In the following study, we set limits on the CP-conserving anomalous coupling h_3^V and h_4^V with form-factor scale set to:

- Λ = 1.5TeV to compare with D0 results;
- Λ = 10000TeV to compare with CMS results.

We set limits by fitting the number of observed events, with $E_T(\gamma) > 60$GeV and jet veto cut, predicted from the NLO MCFM generator (correlated to the particle level), plus backgrounds, to the observed number of $Z\gamma$ candidates with the same cuts. The effect of anomalous coupling on the photon E_T spectrum can seen in Fig **??** for the SM sample and and MC sample generated with two sets of non-zero anomalous couplings normalized with their cross-setion.

Table 47: ATGC limits compared among different experiments at 95% C.L. in $W\gamma$ channel

experiment	ATGC pars	Λ=2TeV	Λ=10000TeV
ATLAS resuls	$\Delta\kappa_\gamma$	(-0.36,0.41)	(-0.33,0.37)
	λ_γ	(-0.079,0.074)	(-0.060,0.060)
D0 results	$\Delta\kappa_\gamma$	(-0.40,0.40)	NA
	λ_γ	(-0.080,0.070)	NA
CMS results	$\Delta\kappa_\gamma$	NA	(-1.11,1.04)
	λ_γ	NA	(-0.18,0.17)

8.2 The method for ATGC measurement in $Z\gamma$ channel

Contributions from anomalous couplings will increase the $Z\gamma$ production cross section and yield photons of higher energy than in the SM process. Measurement in high photon p_T extended fiducial phase space is more sensitive to ATGC coupling. In this study, only $Z\gamma$ candidates events in medium p_T extended fiducial phase space (photon $pT > 60$GeV, $N_{jet} = 0$) as mentioned in Table 23, are used to extract the ATGC limits. The limit is set based on counting of events in medium p_T extended fiducial phase space, not based on the photon p_T shape. The objects and event level selection for ATGC study are the same as used for medium p_T exclusive 0 jet extended fiducial cross-setion measurement, which are described in Section 5.

For MCFM is a NLO generator, we can get the production cross-section directly by generating different MCFM samples with different ATGC parameters. A fixed QCD and factorization scales (μ_{QCD} = μ_{fact} = M_Z) are used for $Z\gamma$ cross section predictions in ATGC model with form factor (Λ=1.5 TeV), and dynamic QCD scales (μ_{QCD} = μ_{fact} = $\sqrt{M_Z^2 + P_t^{\gamma 2}}$) are used in $Z\gamma$ cross section predictions in ATGC model without form factor ($\Lambda = \infty$). The motivation of this choice is presented Appendix **??**. Since we know the cross-section can be described as a second order polynomial function as ATGC parameters, we generate 10 ATGC samples for each $h_{i0}^V(i0 = 3,4; V = Z,\gamma)$ parameter, calculate the expected signal events number in our selected extended fiducial phase space:

$$N_{sig}^{expect} = \sigma_{fiducial}^{Z\gamma} \times C_{Z\gamma} \times A_{Z\gamma} \times L / C*_{Z\gamma}^{parton \to particle} \tag{33}$$

and then fit to a second order poynomial function.

From the second order poynomial function, we can directly get the N_{sig}^{expect} at any ATGC point, and this can help us to reduce the period of huge ATGC samples production which would cost a lot of cpu time. In Fig **??**(Λ =1.5TeV) and Fig **??**(Λ =10000TeV), we show the fitting for each ATGC parameters(just use μ channel as an example), and the fitting functions are summarized in Table 48 .

To set limits on ATGC parameters, we use Bayesian approach, first obtaining the probability density function (PDF) of $P(H_{i0}^V|I_{Z\gamma}^e, I_{Z\gamma}^\mu)$ given the measurement (where $I_{Z\gamma}^e$ and $I_{Z\gamma}^\mu$ denote all the inputs for medium p_T exclusive 0 jet extended fiducial cross section for electron and muon channel respectively in Table 25 and their systematic in Table 51). By integrating all nuisance parameters (including uncertainty in background estimations and signal acceptance and corrections factors), we then extract 95% CL limits based on PDF function $P(H_{i0}^V|I_{Z\gamma}^e, I_{Z\gamma}^\mu)$.

We define the negative log-likelihood function as:

Table 48: Fitting parameters of expected $Z\gamma$ signal events as a function of ATGC parameters $N_{sig}^{expect} = p0 \cdot (h_{i0}^{V})^2 + p1 \cdot h_{i0}^{V} + p2$

channel	Λ=1.5TeV	p0	p1	p2
muon channel	h_{30}^{Z}	$2.97e3 \pm 549$	-37 ± 31.8	25.4 ± 2.46
	h_{30}^{γ}	$2.01e3 \pm 516$	6.9 ± 29.6	25.3 ± 2.41
	h_{40}^{Z}	$2.04e6 \pm 2.46e5$	140 ± 719	25.3 ± 2.55
	h_{40}^{γ}	$1.38e6 \pm 2.26e5$	56.7 ± 657	25.4 ± 2.49
	Λ=10000TeV	p0	p1	p2
	h_{30}^{Z}	$2.49e4 \pm 931$	-45.1 ± 55.3	24.9 ± 2.44
	h_{30}^{γ}	$1.85e4 \pm 891$	9.93 ± 53.7	25.0 ± 2.87
	h_{40}^{Z}	$8.25e8 \pm 3.71e7$	$1.51e3 \pm 1.12e4$	24.9 ± 2.92
	h_{40}^{γ}	$7.30e8 \pm 3.55e7$	$-976 \pm 1.07e4$	25.2 ± 2.88
elec channel	Λ=1.5TeV	p0	p1	p2
	h_{30}^{Z}	$2.48e3 \pm 502$	-31.0 ± 29.1	21.2 ± 2.25
	h_{30}^{γ}	$1.68e3 \pm 472$	5.78 ± 27.1	21.2 ± 2.21
	h_{40}^{Z}	$1.71e6 \pm 2.25e5$	118 ± 658	21.2 ± 2.33
	h_{40}^{γ}	$1.16e6 \pm 2.07e5$	47.4 ± 602	21.3 ± 2.27
	Λ=10000TeV	p0	p1	p2
	h_{30}^{Z}	$2.08e4 \pm 906$	-37.8 ± 54.9	20.9 ± 2.73
	h_{30}^{γ}	$1.55e4 \pm 815$	8.31 ± 49.1	20.9 ± 2.63
	h_{40}^{Z}	$6.91e8 \pm 3.39e7$	$1.26e3 \pm 1.02e4$	20.8 ± 2.67
	h_{40}^{γ}	$6.11e8 \pm 3.25e7$	$-817 \pm 9.80e3$	21.1 ± 2.63

$$-logL(H_{i0}^{V}, \vec{x_k^{\mu}} | I_{Z\gamma}^{\mu}) = -log\left(\frac{e^{-(N_s(H_{i0}^{V}, \vec{x_k^{\mu}}|I_{Z\gamma}^{\mu}) + N_b(\vec{x_k^{\mu}}|I_{Z\gamma}^{\mu}))} \times (N_s^{\mu}(H_{i0}^{V}, x_k^{\mu}|I_{Z\gamma}^{\mu}) + N_b^{\mu}(\vec{x_k^{\mu}}|I_{Z\gamma}^{\mu}))^{N_{obs}^{\mu}}}{N_{obs}^{\mu}!}\right) + \sum_{k=1}^{n}\frac{x_k^{\mu 2}}{2} \tag{34}$$

- where N_{obs} is the number of events observed in data sample.
- x_k is assumed to be normally distributed unit Gaussian, n is the number of nuisance parameters x_k.
- $$N_b(x_k|I_{Z\gamma}^{\mu}) = N_b \prod_{k=1}^{n}(1 + x_k B_k)$$

  where $N_b$is the number of predicted background events and B_k is the fractional size of one standard deviation representing the kth systematic uncertainty for the background. The predicted signal events number

- $$N_s(H_{i0}^{V}, x_k^{\mu}|I_{Z\gamma}^{\mu}) = \sigma_{Z\gamma \to \mu\mu\gamma}^{ATGC} \times L \times A_{Z\gamma}^{\mu} \times C_{Z\gamma}^{\mu} / C*_{Z\gamma}^{parton \to particle} \times \prod_{k=1}^{n}(1 + x_k^{\mu} S_k^{\mu})$$

where S_k is the fractional sizes of the kth systematic uncertainty for signal.

In equation 34, the expression inside the log function is essentially the Poisson probability that the expected number of signal and background events produce the observed number of events. The final term in the likelihood equation is the product of the Gaussian constraints on the nuisance parameters x_k. These nuisance parameters account for the systematic uncertainty on the number of expected signal and background events. Each systematic k is ascribed to an independent source.

$$
\begin{aligned}
P(H_{i0}^V|I_{Z\gamma}^{\mu}, I_{Z\gamma}^{e}) &= c0 \times \int L(H_{i0}^V, \vec{x_{k'}}, \vec{x_{k''}}|I_{Z\gamma}^{\mu}) \times L(H_{i0}^V, \vec{x_{k'}}, \vec{x_{k'''}}|I_{Z\gamma}^{e}) \\
&\quad \times P(\vec{x_{k'}}) \times P(\vec{x_{k''}^{\mu}}) \times P(\vec{x_{k'''}}^{e}) d\vec{x_{k'}} d\vec{x_{k''}} d\vec{x_{k'''}^{e}} \qquad (35) \\
&\qquad (36)
\end{aligned}
$$

- where c0 is just normalization factor for PDF function $P(H_{i0}^V|I_{Z\gamma}^{\mu}, I_{Z\gamma}^{e})$.
- $x_{k'}$ denotes the correlated uncertainties in both electron and muon channel, including uncertainties on photon efficiency, uncertainties on luminosity, uncertainties on theoretical predictions, uncertainties on acceptance, uncertainties on EM scale for photon and uncertainties on jet energy scale and resolution.
- $x_{k''}^{\mu}$ denotes the uncertainties in muon channel, which is not correlated with any uncertainties in electron channel, including uncertainties on muon reconstruction and identification efficiency and uncertainties on muon momentum scale and resolution, background uncertainties in muon channels.
- $x_{k'''}^{e}$ denotes the uncertainties in electron channel, which is not correlated with any uncertainties in muon channel, including uncertainties on electron efficiency, uncertainties on EM scale and resolution for electron and background uncertainties in electron channels.

By integrating over all nuisance parameters ($x_{k'}$, $x_{k''}^{\mu}$ and $x_{k'''}^{e}$) following Equation 36, the PDF function for given ATGC coupling parameters $P(H_{i0}^V|I_{Z\gamma}^{\mu}, I_{Z\gamma}^{e})$ can be obtained. In figure **??**, we show the negative $-Log[P(H_{i0}^V)||I_{Z\gamma}^{\mu}, I_{Z\gamma}^{e}]$ distribution of h_{30}^{γ} for an example.

$$P(H_{i0}^{V\,upper}|I_{Z\gamma}^{\mu}, I_{Z\gamma}^{e}) = P(H_{i0}^{V\,lower}|I_{Z\gamma}^{\mu}, I_{Z\gamma}^{e}) \tag{37}$$

$$\int_{H_{i0}^{V\,lower}}^{H_{i0}^{V\,upper}} P(H_{i0}^V|I_{Z\gamma}^{\mu}, I_{Z\gamma}^{e}) dH_{i0}^V = 0.95 \times \int_{-\infty}^{\infty} P(H_{i0}^V|I_{Z\gamma}^{\mu}, I_{Z\gamma}^{e}) dH_{i0}^V \tag{38}$$

In order to extract the ATGC limits, we define $H_{i0}^{V\,upper}$ and $H_{i0}^{V\,lower}$ in Equation 37 , 38, 39 and 40. When the integral value reaches 95% of the complete integral value,we consider the corresponding ATGC values to be our limits at 95% C.L.. In Table 50, we summarize our extracted ATGC limits at different Λ scale after considering systematics.

$$\int_{H_{i0}^{V\,lower}}^{\infty} P(H_{i0}^V|I_{Z\gamma}^{\mu}, I_{Z\gamma}^{e}) dH_{i0}^V = 0.975 \times \int_{-\infty}^{\infty} P(H_{i0}^V|I_{Z\gamma}^{\mu}, I_{Z\gamma}^{e}) dH_{i0}^V \tag{39}$$

Acceptance and Correction factors for $Z\gamma$ in models with ATGC coupling					
$p_T(\gamma) > 60GeV$ and $N_{jet} == 0$					
		Muon channel			
	Model	$A_{Z\gamma}$	$C_{Z\gamma}$	$C_{Z\gamma} * A_{Z\gamma}$	rel
Sherpa (3 jets)	SM	0.917	0.641	0.588	-
Sherpa (1 jet)	SM	0.921	0.591	0.544	-7.5%
Sherpa	$h3_\gamma = 0.03$	0.909	0.617	0.561	-6.0%
Sherpa	$h3_Z = 0.03$	0.915	0.604	0.553	-13.9%
Sherpa	$h4_\gamma = 0.005$	0.915	0.548	0.502	-4.6%
Sherpa	$h4_Z = 0.005$	0.906	0.558	0.506	-14.6%

Table 49: The variations of acceptance and Correction factors for $Z\gamma$ in models with ATGC coupling.

$$\int_{-\infty}^{H_{i0}^{V\,upper}} P(H_{i0}^V | I_{Z\gamma}^{\mu}, I_{Z\gamma}^{e}) dH_{i0}^V = 0.975 \times \int_{-\infty}^{\infty} P(H_{i0}^V | I_{Z\gamma}^{\mu}, I_{Z\gamma}^{e}) dH_{i0}^V \quad (40)$$

All the systematics applied in equation 34 are summarized in Table 51.

8.3 systematics uncertainties

In the ATGC limit extraction the values of $C_{Z\gamma} \times A_{Z\gamma}$ (see equation 33) are obtained from Table 32. We assume the values of $C_{Z\gamma} \times A_{Z\gamma}$ do not vary significantly, in the extended fiducial phase space for the ATGC limit extraction, between the SM $Z\gamma$ production and the non-SM $Z\gamma$ production in the ATGC parameter space we are exploring.

8.3.1 Addtional systematics for $Z\gamma$ ATGC limits with form factor ($\Lambda = 1.5$ TeV)

In order to prove this assumption, we simulated the $Z\gamma$ events using non-SM ATGC parameters with form-factor, as shown in Equation 32. We studied the kinematic dependence for efficiency factors $C_{Z\gamma}$ using non-SM ATGC full simulations MC samples. As shown in Figure **??**, the efficiency factors $C_{Z\gamma}$ does not show any significant dependence on M(Z;γ) and $\Delta R(l^+;l^-)$. Table 49 shows the $C_{Z\gamma} \times A_{Z\gamma}$ values obtain from the SM MC samples and from ATGC MC samples generated with form factors that are generated at a few ATGC points. The $C_{Z\gamma} \times A_{Z\gamma}$ values vary by about $10-15\%$. This difference has been included as an additional systematics in the ATGC limit extraction.

8.3.2 Addtional systematics for $Z\gamma$ ATGC limits without form factor ($\Lambda = \infty$)

The event kinematic of $Z\gamma$ events in ATGC model without form factor are different from the ATGC model with form factor and the SM model, as shown in Figure **??**. The Z boson is highly boosted in the ATGC model without form factor. Even though we have checked in Figure **??** that efficiency factors $C_{Z\gamma}$ doesn't show any dependence on event kinematic over a large phase space($\Delta R(l^+;l^-) > 0.3$ or $M(Z;gamma) < 2.5$ TeV) . However, there are still some potential acceptance loss in special phase space, where the Z boson is heavily boosted and the open angle between two leptons from Z boson ($\Delta R(l^+;l^-)$) is less than 0.3. The worst senorio is $C_{Z\gamma} = 0$ in the special phase space where $\Delta R(l^+;l^-) < 0.3$. The blue curve in Figure **??** shows the expected signal yield in the worst senorio, and the red curve in Figure **??** shows the normal senorio in which $C_{Z\gamma}$ in ATGC model is very close the SM case. By comparing the expected signal yield in the worst senorio and in normal SM senorio, we can get a conservative estimation of the addtional uncertainties (so called σ_{DRll}) due to this potential acceptance loss. The detailed defintion of σ_{DRll} is shown in Equation 41. The $\sigma_{DRll}(h_{i0}^{V})$ is not a constant, it depends on ATGC parameters. The anomalous couplings influence the kinematic properties of $Z\gamma$ events and thus the corrections for event reconstruction ($C_{Z\gamma}$). The maximum variations of $C_{W\gamma}$ and $C_{Z\gamma}$ within the measured aTGC limits (eg: $\sigma_{DRll}(h4^{V} = 0.00022)$, $\sigma_{DRll}(h3^{V} = 0.027)$) are quoted as addtional systematic uncertainties.

$$\sigma_{DRll} = \frac{N_{expect}^{sig}(h_{i0}^{V})(without dR > 0.0) - N_{expect}^{sig}(h_{i0}^{V})(with dR > 0.3)}{N_{expect}^{sig}(h_{i0}^{V})(without dR > 0.0)} \tag{41}$$

8.3.3 Addtional systematics for $Z\gamma$ ATGC limits : QCD scale dependence

The renormalisation and factorisation scales uncertainty has been mentioned in Section 6 in SM predictions. However this uncertainty may not cover the whole ATGC grid points. In this subsection, we vary the renormalisation and factorisation scales by factors of two around the nominal scales for the whole aTGC grid, and quote the maximum variations in cross section predictions of ATGC models. As shown in Figure **??** and Figure **??**, the expected $Z\gamma$ signal events in μ channel as a functions of aTGCs are calculated using MCFM with different QCD scale. The maximum variations are summarized in Table 51.

Table 50: The observed ATGC limits considering systematics in $Z\gamma$ electron channel and muon channel, as well as the observed and expected combined limits from both channels.

channel	ATGC pars	Λ=1.5TeV	Λ=10000TeV
muon channel	h_{30}^{γ}	(-0.083,0.083)	(-0.033,0.033)
	h_{30}^{Z}	(-0.064,0.083)	(-0.026,0.030)
	h_{40}^{γ}	(-0.0033,0.0035)	(-0.00023,0.00023)
	h_{40}^{Z}	(-0.0027,0.0028)	(-0.00024,0.00024)
elec channel	h_{30}^{γ}	(-0.078,0.085)	(-0.029,0.029)
	h_{30}^{Z}	(-0.060,0.078)	(-0.023,0.028)
	h_{40}^{γ}	(-0.0031,0.0032)	(-0.00021,0.00021)
	h_{40}^{Z}	(-0.0026,0.0027)	(-0.00022,0.00021)
combined	h_{30}^{γ}	(-0.074,0.071)	(-0.028,0.027)
	h_{30}^{Z}	(-0.051,0.068)	(-0.022,0.026)
	h_{40}^{γ}	(-0.0028,0.0027)	(-0.00021,0.00021)
	h_{40}^{Z}	(-0.0024,0.0023)	(-0.00022,0.00021)
expect(combined)	h_{30}^{γ}	(-0.073,0.070)	(-0.027,0.027)
	h_{30}^{Z}	(-0.053,0.066)	(-0.022,0.025)
	h_{40}^{γ}	(-0.0027,0.0027)	(-0.00021,0.00021)
	h_{40}^{Z}	(-0.0022,0.0022)	(-0.00022,0.00021)

Table 51: The list of systematics uncertainties used in ATGC limits setting in $Z\gamma$ analysis. The uncertainties due to QCD scale dependence is mentioned in Section 8.3.3. The addtional systematics due to the potential loss in low $dR(l^+,l^-)$ has been discussed in Section 8.3.2.

systematics	fractional uncertainty(e channel)	fractional uncertainty(μ channel)
Trigger efficiency	0.02%	1.0%
electron reco efficiency	1.0%	
electron ID efficiency	2.2%	
electron iso efficiency	1.0%	
muon ID efficiency		1.4%
Momentum scale and resolution		0.3%
photon ID efficiency	4.3%	4.3%
photon isolation efficiency	2.0%	2.0%
EM scale and resolution	2.2%	1.5%
Jet scale	4.5%	3.8%
Jet resolution	1.0%	1.0%
luminosity	3.7%	3.7%
background	81.0%	76.0 %
$A_{W\gamma} * C_{W\gamma}$ within ATGC sample	15.0%	15.0%
uncertainty for $h_{30}^{\gamma/Z}$ due to accptance loss in $dR(l^+,l^-) < 0.3$ phase space	16.0%	16.0%
uncertainty for $h_{40}^{\gamma/Z}$ due to accptance loss in $dR(l^+,l^-) < 0.3$ phase space	40.0%	40.0%
theoretical		
QCD scale dependence in ATGC grid for $h_{40}^{\gamma/Z}$	8.0%	8.0%
QCD scale dependence in ATGC grid for $h_{30}^{\gamma/Z}$	4.0%	4.0%
PDF	3.4%	3.4%

8.4 Nominal Result

Taking account for all the systematics mention above, we extracted the observed ATGC limits considering systematics in $Z\gamma$ electron channel and muon channel, as well as the observed and expected combined limits from both channels (see Table 50). These results are compared with previously published results: D0 results with $6.2fb^{-1}$ at $\Lambda = 1.5$TeV, and CMS results with $35pb^{-1}$ at $\Lambda = \infty$. The comparison is summarized in Table 52 and Figure **??**.

8.5 More cross check results for $Z\gamma$ ATGC limits without form factor

To desmonstrate the effect of the addtional uncertainties due to the potential acceptance loss in the small $\Delta R(l^+,l^-)$ region, we compare the observed and expect limits in three different configurations and shown in Table 53:

- Configuration one (cross check result): We assume that the efficiency factor $C_{Z\gamma}$ in extreme ATGC model (The ATGC model without form factor) is consistent with $C_{Z\gamma}$ in SM model with 15% as

Table 52: ATGC limits compared among different experiments at 95% C.L. in $Z\gamma$ channel

channel	ATGC pars	Λ=1.5TeV	Λ=10000TeV
ATLAS results	h_{30}^{γ}	(-0.074,0.071)	(-0.027,0.027)
	h_{30}^{Z}	(-0.051,0.068)	(-0.022,0.025)
	h_{40}^{γ}	(-0.0028,0.0027)	(-0.00021,0.00021)
	h_{40}^{Z}	(-0.0024,0.0023)	(-0.00022,0.00021)
D0 results	h_{30}^{γ}	(-0.044,0.044)	NA
	h_{30}^{Z}	(-0.041,0.041)	NA
	h_{40}^{γ}	(-0.0023,0.0023)	NA
	h_{40}^{Z}	(-0.0023,0.0023)	NA
CDF results	h_{30}^{γ}	(-0.022,0.020)	NA
	h_{30}^{Z}	(-0.020,0.021)	NA
	h_{40}^{γ}	(-0.0008,0.0008)	NA
	h_{40}^{Z}	(-0.0009,0.0009)	NA
CMS results	h_{30}^{γ}	NA	(-0.070,0.070)
	h_{30}^{Z}	NA	(-0.050,0.060)
	h_{40}^{γ}	NA	(-0.00050,0.00060)
	h_{40}^{Z}	NA	(-0.00050,0.00050)

shown in Table 49.

- Configuration two (nominal value): On top of 15% systematics mentioned above, we assign an addtional systematics ($\sigma(DRll)$) is quoted to cover the potential acceptance loss in small $\Delta R(l^+,l^-)$ region as shown in Figure **??**.

- Configuration three(cross check result): We introduce a new cut in fiducial selection $\Delta R(l^+,l^-) > 0.3$ to remove the small $\Delta R(l^+,l^-)$ region, and re-extract the ATGC limits in the new fiducial region.

It is found in Table 53 that the limits using the first configuration are the best, and limits in the second and the third configuration is more or less similar. We may underestimate the systematics uncertainties of $C_{Z\gamma}$ in low $\Delta R(l^+,l^-)$ region using configuration one, and there are too much changes in fiducial phase space with respect to the SM measurement in configuration three. As the result, the configuration two is used to extract the final $Z\gamma$ ATGC limits without form factor.

9 Summary

The measurement of $W\gamma$ and $Z\gamma$ production with 1 fb^{-1} of ATLAS data at $\sqrt{s} = 7$ TeV is presented. Fiducial cross sections are measured for photon transverse momentum $p_T^{\gamma} > 15, 60$ and 100 GeV. The fiducial cross sections are also measured for the "inclusive" case, where no jet requirement is applied, and for the "exclusive" case, where there should be no reconstructed jet ($p_T(jet) > 30$ GeV, $|\eta(jet)| < 4.4$) in the final state. The measured "inclusive" fiducial cross sections are significantly higher than the inclusive NLO predictions, especially in phase space with $p_T^{\gamma} > 60$ and 100 GeV. However the measured "exclusive" fiducial cross sections agree well with the exclusive NLO predictions.

Table 53: The observed and expected $Z\gamma$ ATGC limits without form factor ($\Lambda = \infty$) in three different configurations.

channel	ATGC pars	without $\sigma(DRll)$	with $\sigma(DRll)$	apply $dR(l^+,l^-) > 0.3$ cut
Configuration		one	two	three
muon channel	h_{30}^{γ}	(-0.029,0.029)	(-0.033,0.032)	(-0.034,0.034)
	h_{30}^{Z}	(-0.023,0.027)	(-0.026,0.030)	(-0.026,0.031)
	h_{40}^{γ}	(-0.00014,0.00015)	(-0.00023,0.00023)	(-0.00027,0.00029)
	h_{40}^{Z}	(-0.00014,0.00014)	(-0.00024,0.00024)	(-0.00026,0.00028)
elec channel	h_{30}^{γ}	(-0.026,0.026)	(-0.029,0.029)	(-0.031,0.031)
	h_{30}^{Z}	(-0.020,0.025)	(-0.023,0.028)	(-0.023,0.029)
	h_{40}^{γ}	(-0.00013,0.00014)	(-0.00021,0.00021)	(-0.00024,0.00028)
	h_{40}^{Z}	(-0.00012,0.00012)	(-0.00022,0.00021)	(-0.00022,0.00024)
combined	h_{30}^{γ}	(-0.024,0.023)	(-0.028,0.027)	(-0.028,0.028)
	h_{30}^{Z}	(-0.019,0.023)	(-0.022,0.026)	(-0.021,0.026)
	h_{40}^{γ}	(-0.00012,0.00012)	(-0.00021,0.00021)	(-0.00022,0.00023)
	h_{40}^{Z}	(-0.00011,0.00011)	(-0.00022,0.00021)	(-0.00021,0.00022)
expect(combined)	h_{30}^{γ}	(-0.023,0.023)	(-0.027,0.027)	(-0.027,0.027)
	h_{30}^{Z}	(-0.019,0.021)	(-0.022,0.025)	(-0.022,0.024)
	h_{40}^{γ}	(-0.00011,0.00012)	(-0.00021,0.00021)	(-0.00022,0.00022)
	h_{40}^{Z}	(-0.00011,0.00011)	(-0.00022,0.00021)	(-0.00021,0.00021)

The exclusive fiducial measurements at the highest photon transverse momentum threshold ($p_T^{\gamma} >$ 100 GeV for $W\gamma$ and $p_T^{\gamma} > 60$ GeV for $Z\gamma$) are used to determine the limits of the anomalous Triple Gauge-Boson Coupling parameters at the 95% confidence level. The extracted limits have extended the limits set by D0 experiment at the Tevatron, and by the CMS experiment using 35 pb^{-1} of data collected in 2010.

References

[1] Measurement of the production cross section of Wgamma and Zgamma at sqrt(s) = 7 TeV with the ATLAS Detector, ATL-COM-PHYS-2011-119

[2] Measurement of the production cross section of W gamma and Zgamma at sqrt(s) = 7 TeV with the ATLAS Detector and Limits on the Anomalous Triple-Gauge-Boson Couplings, ATL-COM-PHYS-2011-1629

[3] S. Weinberg, *Phys. Rev.* **D13** (1976) 974.

[4] L. Susskind, *Phys. Rev.* **D20** (1979) 2619.

[5] K. D. Lane and E. Eichten, *Phys. Lett. B* **222** (1989) 274.

[6] ATLAS Collaboration, “Luminosity Determination in pp Collisions at $\sqrt{s} = 7$ TeV Using the ATLAS Detector at the LHC”, arXiv:1101.2185

[7] https://twiki.cern.ch/twiki/bin/viewauth/AtlasProtected/ExtendedPileupReweighting

[8] svn+ssh://svn.cern.ch/reps/atlewunfold/EWUnfolding

[9] The RooUnfold package and documentation, http://hepunx.rl.ac.uk/ãdye/software/unfold/RooUnfold.html

[10] Measurement of the $W->l\nu$ and $Z/\gamma*->ll$ production cross sections in proton-proton collisions at sqrt(s) = 7 TeV with the ATLAS detector, CERN-PH-EP-2010-037, arXiv:1010.213v1

[11] https://twiki.cern.ch/twiki/bin/view/AtlasProtected/EnergyRescaler

[12] https://twiki.cern.ch/twiki/bin/view/AtlasProtected/MCPAnalysisGuidelinesRel16

[13] First measurement of the inclusive isolated prompt photon cross section in pp collisions at $\sqrt{s}$ =7TeV with the ATLAS detector, ATL-COM-PHYS-2010-802

[14] https://twiki.cern.ch/twiki/bin/view/AtlasProtected/HowToCleanJets2011

[15] Electron efficiency scale factor and its uncertainty(Egamma recommendations for EPS 2011 analysis), https://twiki.cern.ch/twiki/bin/view/AtlasProtected/EfficiencyMeasurements

[16] https://twiki.cern.ch/twiki/pub/Atlas/MuonTriggerPhysicsTriggerRecommendations2011/trigger.pdf.

[17] Muon reconstruction efficiency in reprocessed 2010 LHC proton-proton collision data recorded with the ATLAS detector, ATLAS-CONF-2011-063

[18] https://twiki.cern.ch/twiki/bin/view/AtlasProtected/MCPAnalysisGuidelinesEPS2011

[19] A Measurement of $W^{\pm}Z$ Production in Proton-Proton Collisions at $\sqrt{s} = 7$ TeV with the ATLAS Detector, ATL-COM-PHYS-2011-1108

[20] Measurement of the ZZ production cross section and limits on anomalous neutral triple gauge couplings in proton-proton collisions at $\sqrt{s} = 7$ TeV with the ATLAS detector, ATL-COM-PHYS-2011-1053

[21] Reconstruction and Identification Efficiency of Inclusive Isolated Photons, ATL-COM-PHYS-2010-803

[22] Photon fudge factor corrections for EPS analysis (Egamma recommendations for EPS 2011 analysis), https://svnweb.cern.ch/cern/wsvn/atlasgrp/Physics/StandardModel/PromptPhotons/FudgeMCTool/trunk/

[23] Measurement of the WW Production Cross Section in Proton-Proton Collisions at $\sqrt{s} = 7$ TeV with the ATLAS Detector and Limits on the Anomalous Triple-Gauge-Boson Couplings, ATL-COM-PHYS-2011-1522

[24] Performance of Missing Transverse Energy Reconstruction in Proton-Proton Collisions at 7 TeV with ATLAS,ech. Rep. ATL-COM-PHYS-2011-567

[25] EGamma energy scale uncertainty and MC smearing recommendations from Egamma group for EPS analysis, https://twiki.cern.ch/twiki/bin/view/AtlasProtected/EnergyRescaler

[26] Jet energy scale and its uncertainty from JET/MET group recommendations for 2011 EPS analysis, https://twiki.cern.ch/twiki/bin/view/AtlasProtected/MultijetJESUncertaintyProvider

[27] Jet energy resolution and its uncertainty from JET/MET group recommendations for 2011 EPS analysis, https://twiki.cern.ch/twiki/bin/view/Main/JetEnergyResolutionProvider

[28] Total inclusive W and Z boson cross-section measurements and cross-section ratios in the electron and muon decay channels at $\sqrt{s} = 7 TeV$, ATL-COM-PHYS-2010-701

[29] https://twiki.cern.ch/twiki/bin/view/AtlasProtected/MCTruthClassifier